

NASATCR-94- 206082

NAGW-3685

7N-43-CR

040601

ANALYSIS OF AIRBORNE RADAR ALTIMETRY MEASUREMENTS OF THE
GREENLAND ICE SHEET

A Dissertation Presented

by

ELLEN J. FERRARO

Submitted to the Graduate School of the
University of Massachusetts Amherst in partial fulfillment
of the requirements for the degree of

DOCTOR OF PHILOSOPHY

May 1994

Department of Electrical and Computer Engineering

© Copyright Ellen J. Ferraro 1994

All Rights Reserved

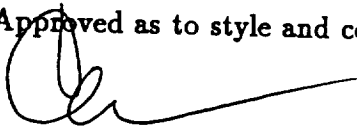
ANALYSIS OF AIRBORNE RADAR ALTIMETRY MEASUREMENTS OF THE
GREENLAND ICE SHEET

A Dissertation Presented

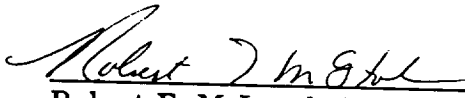
by

ELLEN J. FERRARO

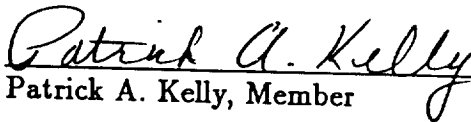
Approved as to style and content by:



Calvin T. Swift, Chair



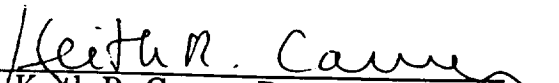
Robert E. McIntosh, Member.



Patrick A. Kelly, Member



Julie Brigham-Grette, Member


Keith R. Carver, Department Head
Electrical & Computer Engineering

To Mom and Dad

ACKNOWLEDGMENTS

During my graduate school years, I have had the invaluable opportunity to not only study microwave remote sensing of the earth, but also to design and manage a project from its development through to its final stages of experiment and data analysis. As my advisor, Dr. Calvin T. Swift allowed me to make my own decisions as well as make my own mistakes, while providing the guidance and encouragement necessary as I progressed from a shy and naive first year graduate student to a doctoral recipient. I would like to thank him for this guidance and for the opportunity to travel to unique places such as Greenland, Iceland and Newfoundland. Both Dr. Calvin T. Swift and Dr. Robert E. McIntosh deserve thanks for providing the excellent facilities and equipment available in the Microwave Remote Sensing Laboratory, without which none of this work would have been possible. I would also like to thank Dr. Patrick Kelly for serving on my committee and Dr. Julie Brigham-Grette for her help in preparing for my trip to Greenland and for serving on my committee.

When the design for the refurbished AAFE altimeter was first being developed, Dr. Chris Rapley, Dr. Seymour Laxon and many other scientists at the Mullard Space Science Laboratory provided invaluable suggestions on current tracking techniques and problems with previous tracking methods, as well as a tremendous amount of literature on radar altimetry. Once the AAFE system was completely developed I spent numerous hours at the NASA Wallops Flight Facility installing and testing the instrument. I would like to thank the aircraft crew and pilots at Wallops for their assistance and friendship. In addition I would like to thank the Observational Sciences Branch, especially Bill Krabill and Earl Frederick for their

patience and help in providing GPS, AOL and INS data and for their friendship. Everyone at Wallops knew how to make a Yankee feel welcome and comfortable on the eastern shore of Virginia.

During my last summer in MIRSL, I spent four weeks on the Greenland ice cap. Despite inhibitions about camping on an ice sheet without heat or hot water, it turned out to be a fun and adventure-some experience, primarily due to the help and friendship of Ingrid Zabel, Paul Baggeroer, Henry Brecher, Mark Anderson and Clint Rowe. I would especially like to thank Clint Rowe and Mark Anderson for their help in the probing experiment.

I would also like to thank Dr. Robert Thomas for providing the funding for this project under NASA grant NGT-50606, Matthew Grund for operating the AAFE altimeter during the 1993 experiment, Wayne Boncyk for his help in developing the data acquisition system of the radar and the numerous other past and present MIRSL graduate students whose suggestions, help and friendship aided in the development of this project. In addition, I would like to thank Claire Hopley for reading and editing this dissertation.

There are many people who helped me through the difficult times in both undergraduate and graduate school, but the person that deserves the most thanks is Dean Nancy Hellman for her encouragement, guidance and friendship. Finally, I would like to thank my friends and family, especially my parents Neal and Bernice Martin, for their love and support throughout the past twenty-six years. I love all of you and none of this would have been worth while if it were not for the opportunities to go home and share these experiences with you. Above all, I thank my husband and friend for life, Paul Ferraro, for his love, his support and for the lifetime that we will share together.

ABSTRACT

ANALYSIS OF AIRBORNE RADAR ALTIMETRY MEASUREMENTS OF THE GREENLAND ICE SHEET

MAY 1994

ELLEN J. FERRARO

B.S.E.E., UNIVERSITY OF MASSACHUSETTS AMHERST

PH.D., UNIVERSITY OF MASSACHUSETTS AMHERST

Directed by: Professor Calvin T. Swift

This dissertation presents an analysis of airborne altimetry measurements taken over the Greenland ice sheet with the 13.9 GHz Advanced Application Flight Experiment (AAFE) pulse compression radar altimeter. This Ku-band instrument was refurbished in 1990 by the Microwave Remote Sensing Laboratory at the University of Massachusetts to obtain high-resolution altitude measurements and to improve the tracking, speed, storage and display capabilities of the radar. In 1991 and 1993, the AAFE altimeter took part in the NASA Multisensor Airborne Altimetry Experiments over Greenland, along with two NASA laser altimeters. Altitude results from both experiments are presented along with comparisons to the laser altimeter and calibration passes over the Sondreström runway in Greenland. Although it is too early to make a conclusion about the growth or decay of the ice sheet, these results show that the instrument is capable of measuring small-scale surface changes to within 14 centimeters.

In addition, results from these experiments reveal that the radar is sensitive to the different diagenetic regions of the ice sheet. Return waveforms from the wet-snow, percolation and dry-snow zones show varying effects of both surface scattering and sub-surface or volume scattering. Models of each of the diagenetic regions of Greenland are presented along with parameters such as rms surface roughness, rms

surface slope and attenuation coefficient of the snow pack obtained by fitting the models to actual return waveforms.

TABLE OF CONTENTS

	<u>Page</u>
ACKNOWLEDGMENTS	v
ABSTRACT	vii
LIST OF TABLES	xi
LIST OF FIGURES	xii
CHAPTERS	
1. INTRODUCTION	1
1.1 History of Radar Altimetry	1
1.2 Scientific Motivation	2
1.3 Summary of Chapters	4
2. PRINCIPLES OF RADAR ALTIMETRY	6
2.1 Altitude Measurements	6
2.2 Pulse compression	8
2.3 Mode of Operation	16
3. AAFE RADAR ALTIMETER SYSTEM	24
3.1 Radar System Hardware	25
3.1.1 Transmitter Subsystem	28
3.1.2 Antenna	31
3.1.3 Receiver Subsystem	31
3.1.4 Data Acquisition Subsystem	36
3.1.5 Tracking Subsystem	40
3.1.6 Control Subsystem	47
3.2 System Calibration	49
3.2.1 Internal Calibration	49
3.2.2 External Calibration	55
3.3 Noise Analysis	55
3.3.1 System Signal-To-Noise Ratio	55
3.3.2 Range Resolution	66
3.3.3 Quantization Noise	69
3.3.4 FFT Errors	69

4. ALTIMETRY MEASUREMENTS OF THE GREENLAND ICE SHEET	71
4.1 1991 Greenland Experiment	71
4.1.1 Experiment Description and Flight Lines	71
4.1.2 Runway Ground Truth Comparison	72
4.1.3 Comparison with the AOL Laser Altimeter	78
4.1.4 Comparison of Flight Line Cross-over Points	88
4.1.5 Altitude Results	90
4.2 1993 Greenland Experiment	93
4.2.1 Experiment Description and Flight Lines	93
4.2.2 Runway Ground Truth Comparison	98
4.2.3 Altitude Results	98
4.3 Comparison of 1991 and 1993 Elevation Measurements	101
5. ANALYSIS OF WAVEFORMS FROM THE GREENLAND ICE SHEET	106
5.1 Scattering Models of the Diagenetic Zones of Greenland	110
5.1.1 Wet-snow Zone Model	110
5.1.2 Percolation Zone Model	120
5.1.3 Dry-snow Zone Model	132
5.2 Mapping Diagenetic Zones	144
5.3 Comparison of Retracking Algorithms	148
6. CONCLUSIONS AND RECOMMENDATIONS FOR FUTURE RESEARCH	159
REFERENCES	161

LIST OF TABLES

Table		Page
3.1	Table of AAFE parameters used to calculate the system signal-to-noise ratio.	64
5.1	Table of the five parameters used in the least-mean-squared error fit to the surface scattering model.	115
5.2	Table of the seven parameters used in the LMSE fit to the combined surface and Rayleigh volume scattering model.	140
5.3	Table of the five parameters used in the least-mean-squared error fit to the Martin et al. model.	151

LIST OF FIGURES

Figure	Page
2.1 Principle of a radar altimeter altitude measurement.	7
2.2 Example of a chirp waveform with a linear frequency modulation [Skolnik, 1980].	9
2.3 The time-frequency plot of the chirp waveform shown in figure 2.2 [Skolnik, 1980].	10
2.4 Illustration of a Reflective Array Compression device and its input and output waveforms.	12
2.5 One method of de-chirping a waveform in a pulse compression radar [Ulaby et al., 1982].	13
2.6 Example of a de-chirped pulse with duration $\frac{1}{B}$ and power BT [Skol- nik, 1980].	14
2.7 Illustration of full deramping and how it converts time delays into shifts in frequency [Rapley, 1990].	15
2.8 Geometry of the beam-limited mode of operation in radar altimetry [Rapley, 1990].	17
2.9 Geometry of the pulse-limited mode of operation in radar altimetry. .	19
2.10 Stages of the illuminated footprint area in the pulse-limited mode of operation [Rapley, 1990].	20
2.11 Effects of the footprint area on the radar altimeter return waveform. .	22
2.12 Geometry for deriving the area of the pulse-limited footprint, [Rapley, 1990].	23
3.1 Comparison of the original AAFE system waveform (top waveform) and the refurbished AAFE system waveform (bottom waveform). . .	26
3.2 A simplified block diagram of the entire AAFE radar altimeter system.	27
3.3 Block diagram of the AAFE transmitter subsystem [NASA, 1976]. . .	29

3.4	Output of AAFE RAC device measured with a spectrum analyzer. . .	30
3.5	(a) The E-plane gain pattern of the main AAFE horn antenna and (b) the H-plane gain pattern of the main AAFE horn antenna.	32
3.6	Diagram of the main AAFE horn antenna.	33
3.7	Block diagram of the original AAFE receiver subsystem [NASA, 1976].	34
3.8	Block diagram of the refurbished AAFE receiver subsystem.	35
3.9	Example of how the AAFE altimeter converts delays in range to shifts in frequency [NASA, 1976].	37
3.10	Simplified block diagram of the AAFE altimeter data acquisition subsystem.	38
3.11	Examples of how the tracking subsystem keeps a waveform in the range window of the altimeter.	42
3.12	Illustration of (a) the maximum value tracker and (b) the OCOG tracker used in the AAFE altimeter tracking subsystem.	44
3.13	A series of waveforms illustrating the acquisition procedure of the AAFE altimeter radar system.	46
3.14	Simplified block diagram of the AAFE altimeter control subsystem. .	48
3.15	Internal delays in the AAFE radar altimeter system.	50
3.16	Simplified block diagram of the AAFE transmitter and receiver, show- ing the path taken by the chirp and de-chirp pulse when the system is in the calibration mode.	51
3.17	Actual internal calibration impulse of the AAFE radar altimeter. . .	52
3.18	Example of measurement of (a) $t_{hardware}$ and (b) $t_{waveguide}$ for internal calibration.	54
3.19	Example of external calibration to surface below aircraft, when the aircraft is on the ground.	56
3.20	Example of how added noise affects the shape of the AAFE altimeter return waveform.	57

3.21	Method used to model a noisy radar receiver. (a) Signal entering noisy receiver; (b) equivalent system with noiseless receiver and noise added to input signal; (c) equivalent system using linearity to model the system as two separate noiseless receivers.	58
3.22	Simplified block diagram of the receiver showing the location of each signal in equations 3.9, 3.10 and 3.11.	60
3.23	Final output of receiver when the input is a return from a single point scatterer.	61
3.24	Signal-to-noise ratio of the AAFE altimeter versus aircraft altitude using a σ^o of 3 dB. (a) Theoretical $\frac{S}{N}$ for the altimeter and (b) actual $\frac{S}{N}$ due to the limited dynamic range of the receiver.	65
3.25	Calculation of time error, Δt , using the leading edge of the ideal and noisy pulse.	67
3.26	Range resolution of the AAFE radar altimeter versus altitude (a) using an approximate leading edge rise time of 13.88 nsecs and (b) using the maximum and minimum realizable values of surface roughness to calculate the leading edge rise time.	68
4.1	Illustration of the measurement of the ice sheet altitude above the ellipsoid.	73
4.2	Four of the flight lines in the 1991 Greenland experiment.	74
4.3	The final three flight lines in the 1991 Greenland experiment, which were all under the ERS-1 trajectory.	75
4.4	A comparison between the aircraft position on September 18, 1991 and September 19, 1991.	76
4.5	Location of differential GPS receivers and all of the 1991 flight lines.	77
4.6	A typical AAFE return waveform from the Sondrestrom runway with the actual data points (asterisks), the model fit to the waveform (dashed line) and the resulting retracked altitude point (solid line).	79
4.7	A comparison between the AAFE altimeter altitude measurements on September 18, 1991 and the ground-based GPS altitude measurements on September 10, 1991. (a) The actual AAFE and ground GPS altitude measurements and (b) the difference between the two data sets calculated by subtracting the ground GPS altitude measurements from the AAFE altitude measurements.	80

4.8	A comparison between the AOL altitude measurements on September 18, 1991 and the ground-based GPS altitude measurements on September 10, 1991. (a) The actual AOL and ground GPS altitude measurements and (b) the difference between the two data sets calculated by subtracting the ground GPS altitude measurements from the AOL altitude measurements.	82
4.9	Interaction of the AAFE radar altimeter footprint and the AOL laser footprint.	83
4.10	A comparison between AAFE and AOL altitude measurements on September 18, 1991 over the Sondrestrom runway. (a) The actual AAFE and AOL altitude measurements and (b) the difference between the two data sets calculated by subtracting the AOL altitude measurements from the AAFE altitude measurements.	85
4.11	A comparison between AAFE and AOL altitude measurements on September 18, 1991 over a 10 kilometer section of the ice sheet. (a) The actual AAFE and AOL altitude measurements and (b) the difference between the two data sets calculated by subtracting the AOL altitude measurements from the AAFE altitude measurements.	86
4.12	A comparison between AAFE and AOL altitude measurements on September 18, 1991 over an entire south-west to north-east pass over the ice sheet. (a) The actual AAFE and AOL altitude measurements and (b) the difference between the two data sets calculated by subtracting the AOL altitude measurements from the AAFE altitude measurements.	87
4.13	A histogram of the difference in altitude at the cross-over points of the AAFE altimeter taken on different days in the 1991 Greenland experiment.	89
4.14	A histogram of the difference in altitude at the cross-over points of the AAFE altimeter taken on the same day in the 1991 Greenland experiment.	91
4.15	A map of the elevations measured by the AAFE altimeter in the 1991 experiment. The location of the highest measured elevation at 72.8° N latitude, 322.0° longitude and the lower dome near 65.2° N latitude, 314.0° longitude can be noted.	92
4.16	The first four flight lines in the 1993 Greenland experiment.	94
4.17	The fifth through eighth flight lines in the 1993 Greenland experiment.	95

4.18	The final three flight lines in the 1993 Greenland experiment.	96
4.19	All of the flight lines in the 1993 Greenland experiment and the location of the differential GPS receivers.	97
4.20	A comparison between the AAFE altimeter altitude measurements on July 1, 1993 and the ground-based GPS altitude measurements on September 10, 1991. (a) The actual AAFE and ground GPS altitude measurements and (b) the difference between the two data sets calculated by subtracting the ground GPS altitude measurements from the AAFE altitude measurements.	99
4.21	A map of the elevations measured by the AAFE altimeter in the 1993 experiment.	100
4.22	A map of the major areas that were covered in both the 1991 and 1993 Greenland experiments.	102
4.23	A comparison between AAFE altitude measurements of the ERS-1 line on September 18, 1991 and July 9, 1993. (a) The actual altitude measurements, (b) the difference between the two data sets calculated by subtracting the 1991 data from the 1993 data and (c) the horizontal distance between the location of the 1991 altitude measurement and the 1993 altitude measurement.	103
4.24	A comparison between AAFE altitude measurements of the EGIG line on September 4, 1991 and July 9, 1993. (a) The actual altitude measurements, (b) the difference between the two data sets calculated by subtracting the 1991 data from the 1993 data and (c) the horizontal distance between the location of the 1991 altitude measurement and the 1993 altitude measurement.	104
5.1	Six altimeter return waveforms from the Greenland ice sheet.	107
5.2	Distribution of the diagenetic zones in Greenland according to Benson and the location of the six altimeter waveforms of figure 5.1.	108
5.3	Model of surface scattering in the wet-snow zone of the Greenland ice sheet.	112
5.4	Surface scattering model for radar altimetry (each range bin = 2.77 nsec). (a) The effects of varying rms surface height, σ_h , on the surface scattering model and (b) the effects of varying rms surface slope, s , on the surface scattering model.	113

5.5	(a) Surface scattering model fit to waveform 2 of figure 5.1., (b) surface scattering model fit to waveform 4 of figure 5.1., and (c) surface scattering model fit to waveform 6 of figure 5.1.	116
5.6	Measurements of the rms surface height over a south-west to north-east flight line. (a) The actual altitudes measured and (b) the rms surface height determined by fitting 960 averaged waveforms to the surface scattering model in equation 5.9.	117
5.7	Measurements of the rms surface slope over a flight section in the wet-snow zone. (a) The actual altitudes measured and (b) the rms surface slope determined by fitting 960 averaged waveforms to the surface scattering model in equation 5.9.	119
5.8	Model of sub-surface scattering in the percolation zone of the Greenland ice sheet.	121
5.9	Six sample altimeter return waveforms from the central part of the percolation zone of Greenland.	122
5.10	A sample distribution of the ice features in a 5 x 3 meter area of the Greenland ice sheet at Dye 2. Each measurement represents the depth that the steel rod hit ice.	125
5.11	The ice features in vertical wall # 1 of the 5 x 3 meter pit. The features shown were located from 0 to 2.5 meters along the 5 meter length of the wall.	126
5.12	A sample distribution of the location of ice features below the surface or $n(h)$ in the Greenland snow pack at Dye 2.	128
5.13	Picture of an ice pipe taken during the 1993 Greenland ground truth experiment at Dye 2.	129
5.14	Picture of an ice lens taken during the 1993 Greenland ground truth experiment at Dye 2.	130
5.15	Altimeter model returns from the percolation zone. (a) The volume scattering component of the return and (b) the sum of the surface and volume scattering returns.	133
5.16	Actual AAFE Altimeter return waveforms from the percolation zone obtained while the aircraft flew over the Dye 2 camp site.	134
5.17	Model of Rayleigh volume scattering in the dry-snow zone of the Greenland ice sheet.	136

5.18	Effects of varying attenuation, α , on the Rayleigh volume scattering model of the dry-snow zone of Greenland.	138
5.19	Combined surface and Rayleigh volume scattering model for varying values of snow density, ρ_s , and liquid water content, m_v	139
5.20	Combined surface and Rayleigh volume scattering model fit to waveform 6 of figure 5.1.	142
5.21	Results of the combined surface and Rayleigh volume scattering model fit to AAFE return waveforms from the dry-snow zone of the Greenland ice sheet. (a) Values of attenuation coefficient, α , (b) values of rms surface height, σ_h , and (c) values of rms surface slope, s	143
5.22	A block diagram of the algorithm used to determine the transitions between diagenetic zones of the Greenland ice sheet.	145
5.23	Raw data from passing the AAFE return waveforms from 1991 and 1992 through the diagenetic zone algorithm.	146
5.24	Smoothed results from the AAFE transition algorithm from 1991 and 1992 and the results from Benson in 1962.	147
5.25	A comparison between AAFE altitudes obtained from retracking by fitting to the surface scattering model and AOL altitude measurements on September 18, 1991 over an entire south-west to north-east pass over the ice sheet. (a) The actual AAFE and AOL altitude measurements and (b) the difference between the two data sets calculated by subtracting the AOL altitude measurements from the AAFE altitude measurements.	150
5.26	Sample radar altimeter waveform using the Martin et al [Martin et al, 1983] model.	152
5.27	A comparison between AAFE altitudes obtained from retracking by fitting to the Martin et al. [Martin et al., 1983] model and AOL altitude measurements on September 18, 1991 over an entire south-west to north-east pass over the ice sheet. (a) The actual AAFE and AOL altitude measurements and (b) the difference between the two data sets calculated by subtracting the AOL altitude measurements from the AAFE altitude measurements.	153

- 5.28 A comparison between AAFE altitudes obtained from retracking using the Offset Center of Gravity (OCOG) algorithm and AOL altitude measurements on September 18, 1991 over an entire south-west to north-east pass over the ice sheet. (a) The actual AAFE and AOL altitude measurements and (b) the difference between the two data sets calculated by subtracting the AOL altitude measurements from the AAFE altitude measurements. 155
- 5.29 An actual AAFE return waveform (asterisks) consisting of 100 points spaced 41.67 cm apart and the cubic spline (solid line) consisting of 5000 points spaced .83 cm apart. 156
- 5.30 A comparison between AAFE altitudes obtained from retracking using the cubic spline algorithm and AOL altitude measurements on September 18, 1991 over an entire south-west to north-east pass over the ice sheet. (a) The actual AAFE and AOL altitude measurements and (b) the difference between the two data sets calculated by subtracting the AOL altitude measurements from the AAFE altitude measurements. 158

CHAPTER 1

INTRODUCTION

1.1 History of Radar Altimetry

Since variations in climate are directly related to the growth and decay of the ice sheets, a better understanding of the current global climate can be achieved by studying their volume or mass balance. Obtaining accurate mass balance measurements is, however, difficult because of the ice sheets enormous size, inaccessibility and harsh surface conditions. In 1966, Robin proposed using satellite radar altimetry to help alleviate this problem [Robin, 1966]. Seven years later the first experimental spaceborne radar altimeter, S-193, was launched on NASA's Skylab [McGoogan et al., 1974]. Due to its success in providing geodetic and oceanographic information, several spaceborne altimeter projects followed. These projects included the GEOS-3 (1975), SEASAT (1978), and GEOSAT (1985) satellite radar altimeters, and the more recent ERS-1 (1991) and TOPEX/POSEIDON (1992) satellite radar altimeters [Davis, 1992]. Although their intended purpose was oceanographic, altitude measurements from SEASAT and GEOSAT have also been used to create surface elevation maps of most of the Greenland and Antarctic ice sheets [Zwally et al., 1983], [Gundestrup et al., 1986], [Zwally et al., 1987], [Bindenschadler et al., 1989]. Glaciologists use these maps to study the current status and annual rate of change in the surface altitude of the ice sheets. This measurement of elevation change is then used to determine variations in the mass balance or volume of the ice sheets and ultimately to understand their response to changes in global climate.

1.2 Scientific Motivation

Recent interest in determining the mass balance of the ice sheets is primarily due to their direct relationship to global sea level. Since a significant change in the current sea level would affect many of the major cities of the world, there is an increasing drive to determine the causes of sea level variation and how it will change over the next century. Satellite radar altimetry measurements taken between 1978 and 1985 show that the Greenland ice sheet south of 72° N is thickening at a rate of .23 meters/year [Zwally et al., 1989]. This should correspond to a subsequent sea level reduction, but instead the level of the sea has increased by $2.4 \pm .9$ mm/year during the past 50 years [Meier, 1990]. Some scientists claim that a decrease in global temperature leads to an increase in ice volume [Schneider, 1992], while many others believe that an increase in global temperature causes an increase in precipitation in the polar regions and therefore an increase in the volume of the ice sheets [Zwally, 1989]. These conflicting hypotheses show that changes in ice sheet volume and the resulting effect on sea level demand further investigation. Previous satellite radar altimetry measurements do not include areas north of 72° N, sensitive drainage basins or ice sheet margins, and therefore it may be premature to conclude that the ice sheets are growing [Schneider, 1992]. In addition, the effects of penetration and sub-surface scattering on the radar altimeter altitude measurement are not yet well understood and need to be studied in greater detail.

In 1985, Swift *et al.* showed that the scattering and emission processes at X and C-band are affected by sub-surface inhomogeneities in the Greenland ice sheet [Swift et al., 1985]. These sub-surface features have been recorded by glaciologists and are one of several diagenetic facies, or physical and chemical characteristics, used to divide ice sheets into zones. The most common zones or stratigraphic regions are the ablation, soaked, percolation and dry-snow zones. In the ablation zone, which is usually near the edge of the ice sheet, the entire snowfall from the previous year

is ablated or lost during the summer months. Similarly, in the soaked zone all the snow deposited over the previous year is raised to the melting point during the summer months, but it is not necessarily ablated. The ablation and soaked zones are sometimes combined into a region called the wet-snow zone. The percolation zone lies in the higher altitudes of the ice sheets, where there is less summer melting. Here the melt water percolates down through the upper layers of the ice sheet and refreezes into ice layers, ice pipes and ice lenses. Finally, in the dry-snow zone melting never occurs. In 1962, Benson determined that the Greenland ice sheet has all four diagenetic zones [Benson, 1962].

Changes in Ku-band satellite radar altimeter waveforms over the different diagenetic regions of Greenland have been noted and analyzed [Ridley and Partington, 1988], [Partington et al., 1989], [Davis, 1993]. These satellite waveforms show that returns from some areas of the ice sheet have both a surface and volume scattering component. The volume or sub-surface component is due to penetration of the Ku-band pulse into the ice sheet. Determining the amount of the radar return caused by surface reflection as opposed to sub-surface scattering is, however, very difficult. Another issue that has not been addressed in the literature is the response of the radar to ice features in the percolation zone. A more thorough understanding of the effects of the diagenetic zones on the radar altimeter waveform not only helps determine if there are biases in altitude measurements due to penetration, but also allows mapping of the boundaries of the diagenetic regions. Uncertainties such as these have been investigated with controlled experiments using the refurbished AAFE radar altimeter in conjunction with laser altimeters, which are not affected by sub-surface scattering. These airborne experiments were conducted over Greenland by NASA in 1991 and 1993, and will continue to occur every other year for the next several years.

1.3 Summary of Chapters

This dissertation contains a comprehensive analysis of the airborne radar altimetry measurements taken over the Greenland ice sheet in 1991 and 1993. The first chapter presents the history of radar altimetry, the scientific motivation behind studying changes in the earth's ice sheets and a summary of the chapters. Chapter 2 reviews radar altimetry principles such as pulse compression and the beam-limited and pulse-limited mode of operation. In Chapter 3, a complete description of the AAFE radar altimeter system hardware as well as a description of the internal and external calibration procedures is provided. This chapter also analyzes the noise level of the system and its sources, and establishes the resulting precision of the altitude measurements of the instrument.

The radar altimeter return waveforms have been retracked or processed to determine the exact location in the waveform corresponding to the mean altitude in the pulse-limited footprint. The result is the altitude of the aircraft above the surface. The GPS receivers, on the other hand, calculate the aircraft altitude above the ellipsoid, which is a reference sphere around the surface of the earth. The difference between these two measurements is the actual ice sheet altitude above the ellipsoid. A complete analysis of the surface elevation measurements obtained in the 1991 and 1993 Greenland experiments is presented in Chapter 4 of this dissertation. This includes an experiment description and a map of all flight lines over the ice sheet. To determine system biases, the data are compared with ground-based GPS measurements taken on the Sondrestrom runway. In addition, a comparison with the AOL laser altimeter over all flight lines is used to examine the system noise level as well as locations on the ice sheet where the retracking algorithm fails. This chapter also compares crossover points to determine system repeatability and evaluates the results from both experiments. From these surface elevation results, the rate of change in the surface of the ice sheet between 1991 and 1993 is investigated.

The experimental flights over Greenland covered all of the diagenetic or stratigraphic zones of the ice sheet. Chapter 5 analyzes the effects on the altimeter waveform shape due to the different scattering properties in each zone. Scattering models for each diagenetic region are presented and fit to AAFE return waveforms. Using these models, the boundaries of the zones have been mapped with AAFE data and analyzed. In addition, the 1993 ground truth data obtained at Dye 2 are compared to results from the scattering models.

The final chapter of this dissertation discusses the results and conclusions of this analysis, and suggests system improvements and future experiments.

CHAPTER 2

PRINCIPLES OF RADAR ALTIMETRY

2.1 Altitude Measurements

The radar altimeter is a nadir viewing instrument that measures the mean distance between the radar and the surface directly below it by sending a short pulse of microwave energy and measuring the time it takes the pulse to reflect off the ground and return to the radar. The altitude of the instrument above the surface, h , is calculated by using the speed of the transmitted pulse, which is the speed of light or $c = 3.0 \times 10^8$ meters per second and the relationship

$$h = \frac{ct}{2} \quad (2.1)$$

where t is the round-trip time recorded by the altimeter. This main principle of radar altimetry is illustrated in figure 2.1.

High range resolution is achieved in radar altimetry by transmitting a narrow pulse and analyzing the return waveform. The minimum resolution of a single altitude measurement, Δh , is

$$\Delta h = \frac{cT}{2} \quad (2.2)$$

where T is the transmitted pulse width. Since this accuracy is often degraded by noise, several returns are usually averaged together to reduce the noise level. If a radar altimeter transmits a 10 nanosecond pulse, for example, the minimum obtainable range resolution is 1.5 meters. By understanding the response of the instrument to certain geophysical surfaces, even better range resolution is achieved. For example, Brown [1977] showed that the radar return from a rough, horizontal

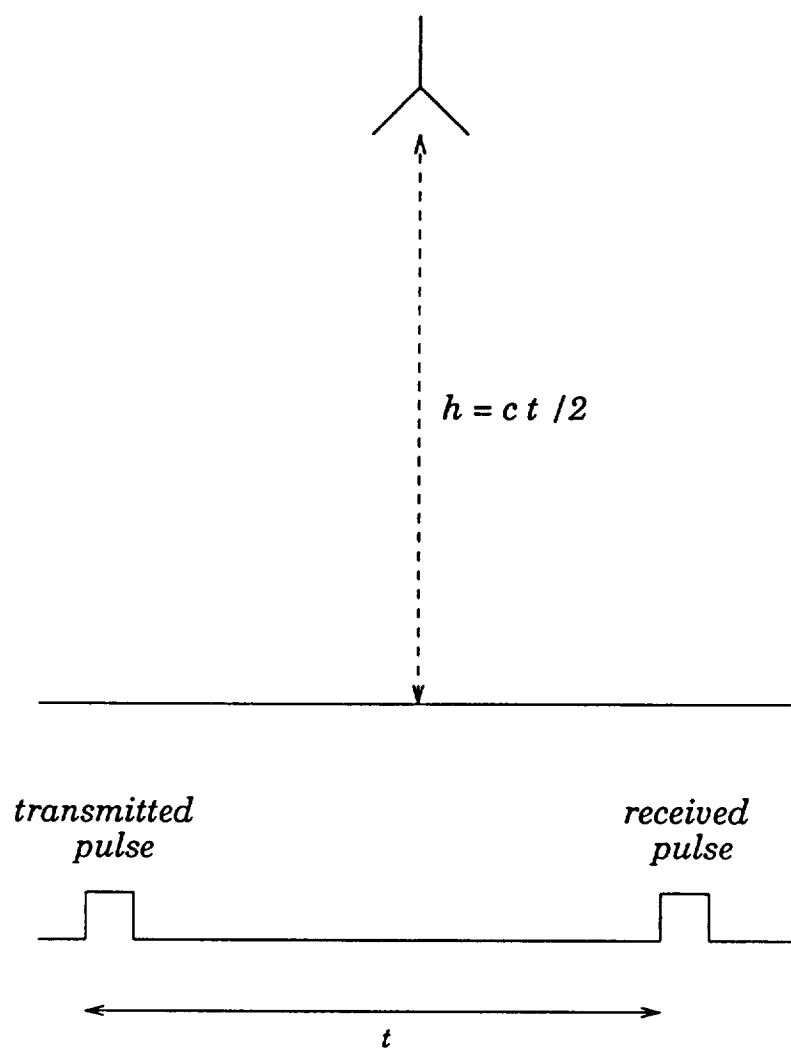


Figure 2.1. Principle of a radar altimeter altitude measurement.

surface is a convolution of the radar system point target response, $P_{pt}(t)$; the flat surface impulse response, $P_{fs}(t)$, which depends mostly on the antenna gain; and the height distribution of the surface scatterers, $q(t)$, or

$$P_r(t) = P_{pt}(t) * P_{fs}(t) * q(t). \quad (2.3)$$

Brown also quantified $P_{pt}(t)$ and $P_{fs}(t)$ for a nadir-viewing radar altimeter. Since the ocean is a rough, horizontal surface and the height distribution of its surface scatterers is known, radar altimeter return waveforms from the ocean are well understood. When these waveforms are fit to the Brown model, they produce range measurements accurate to within 10 cm. This method of increasing range resolution using the return waveform is commonly used in radar altimetry.

2.2 Pulse compression

As equation 2.2 shows, an extremely narrow pulse should be transmitted to achieve as high range resolution as possible. It is difficult, however, to create a small pulse with enough power to obtain a desirable signal-to-noise ratio. This problem can be overcome by pulse compression, a technique that uses increased bandwidth. A pulse compression radar transmits a chirp or FM modulated pulse of duration T , power P_t and bandwidth B . Figure 2.2 gives an example of a typical chirp and figure 2.3 shows its time-frequency plot. A chirp is usually created by exciting a dispersive delay line with an impulse. The frequency response of the delay line causes each frequency component of the input impulse to have a different time delay. For example, a Reflective Array Compression (RAC) device creates a chirp by first converting the input impulse into an acoustic signal in the input transducer and then passing it onto a series of reflective gratings that are etched on the surface of a piezoelectric crystal. The incoming signal is reflected 90° by the first set of grooves and then another 90° by the second set of grooves before it goes to the

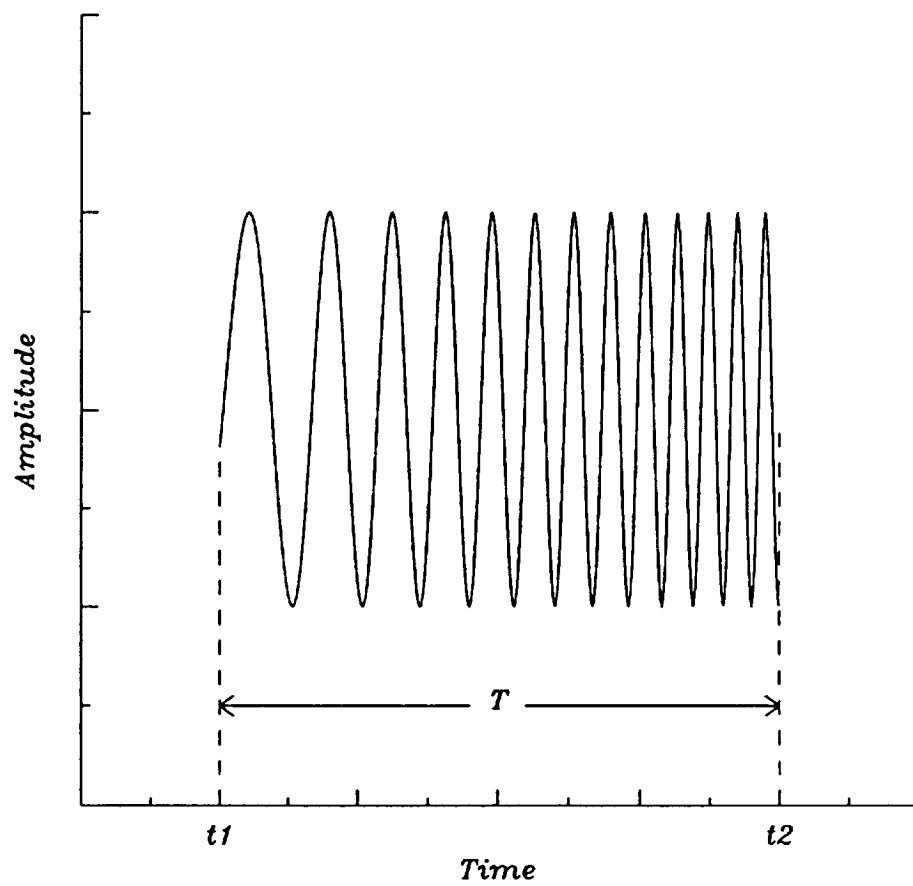


Figure 2.2. Example of a chirp waveform with a linear frequency modulation [Skolnik, 1980].

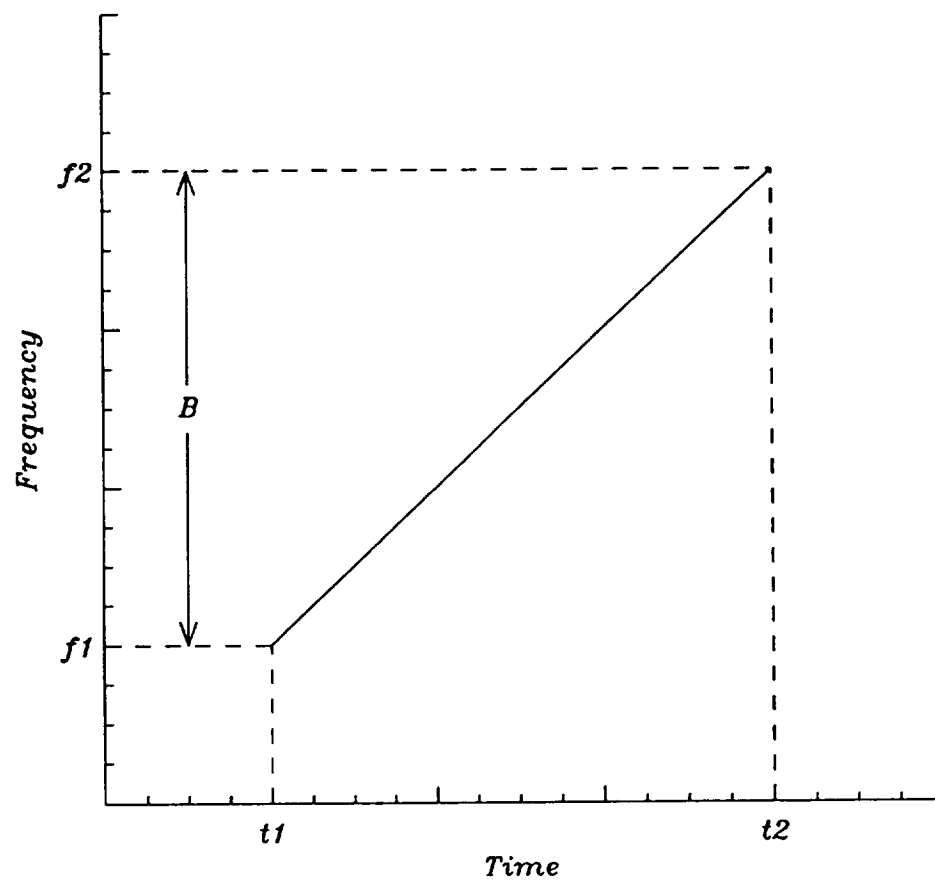


Figure 2.3. The time-frequency plot of the chirp waveform shown in figure 2.2 [Skolnik, 1980].

output transducer and is converted back to a microwave signal. Each set of grooves is spaced so that the propagation delay of the U-shaped path depends on frequency. As a result, the high frequency components of the input impulse travel a longer distance than the low frequency components and therefore exit the device later. Figure 2.4 illustrates a RAC device and some typical time and frequency domain waveforms at its input and output [NASA, 1976],[Skolnik, 1980].

Once the chirp pulse has been transmitted and received by the radar, it must be de-chirped. This is often done by inverting the frequency sweep of the received chirp and passing it back through the dispersive delay line, as illustrated in the block diagram in figure 2.5 [Ulaby et al., 1982]. In the example of the RAC, the high frequency components, which enter the device first, travel a longer path than the low frequency components and, as a result, all components are compressed together in time. The output, as shown in figure 2.6, is a pulse of duration $\tau = \frac{1}{B}$ and power $P'_t = P_t * BT$. Thus a low-power long duration pulse can be used to obtain the same range resolution as a high-power short duration pulse [Skolnik, 1980].

Another way of de-chirping a received pulse is to mix it with a replica chirp. This method, known as full deramping, causes delays in time to be converted to shifts in frequency. Figure 2.7 illustrates how the returns from three different ranges are transformed into separate frequency components. The resulting de-chirped waveform must be analyzed in the frequency domain, and its frequency resolution is

$$\Delta f = \frac{B}{T} \tau = \frac{1}{T} \quad (2.4)$$

where B and T are the actual transmitted bandwidth and pulse width respectively, and τ is the effective pulse duration [Rapley, 1990].

The compression ratio, CR , is a parameter often used to measure the effectiveness of a pulse compression radar. It is defined as the actual transmitted pulse length, T , divided by the effective pulse length, τ , or

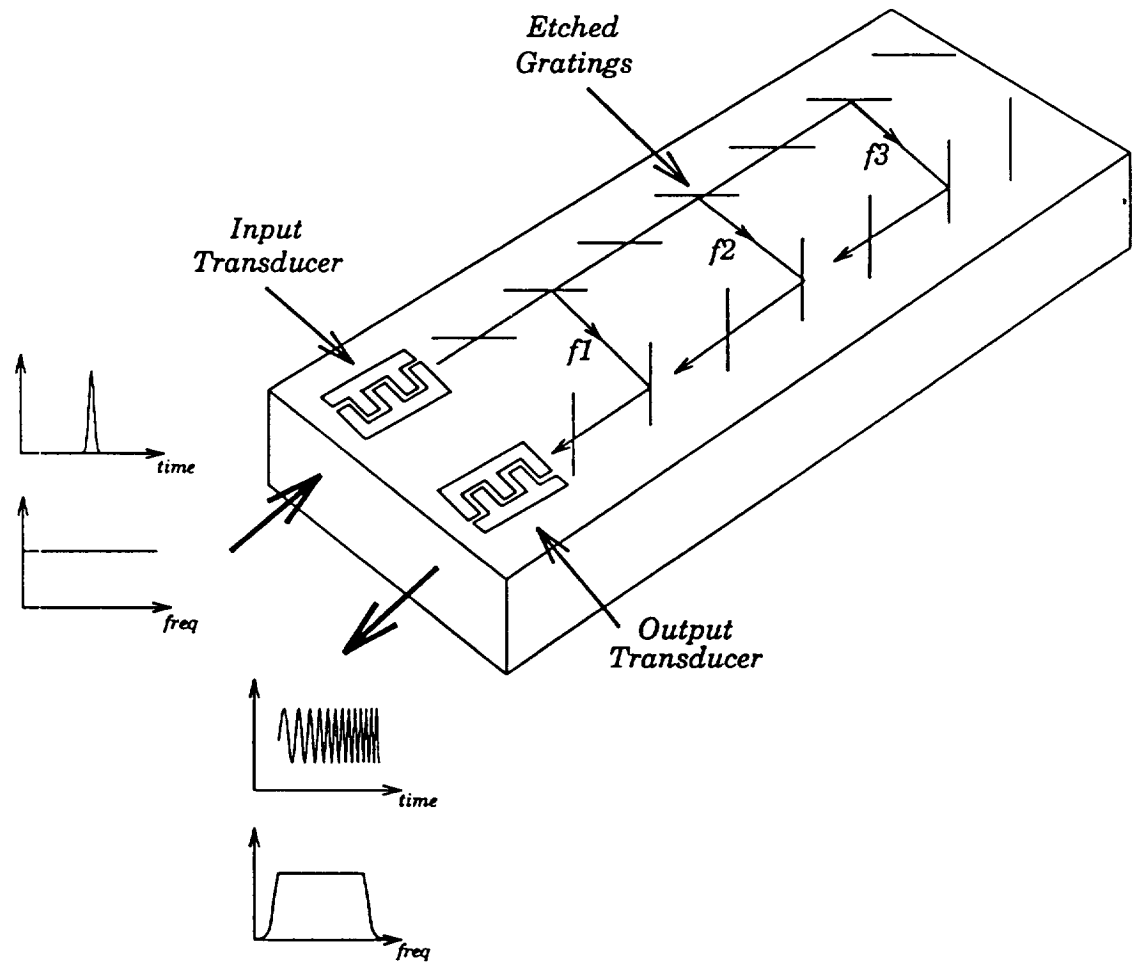


Figure 2.4. Illustration of a Reflective Array Compression device and its input and output waveforms.

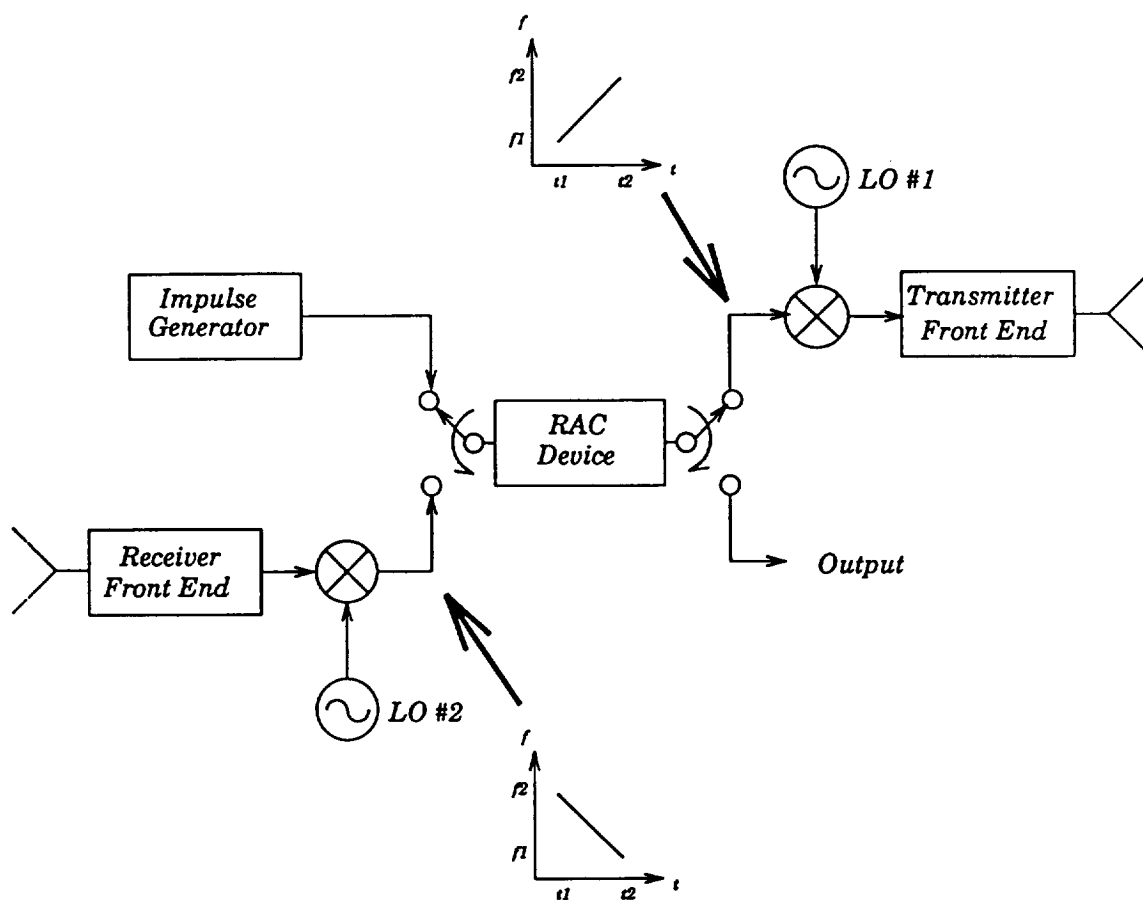


Figure 2.5. One method of de-chirping a waveform in a pulse compression radar [Ulabay et al., 1982].

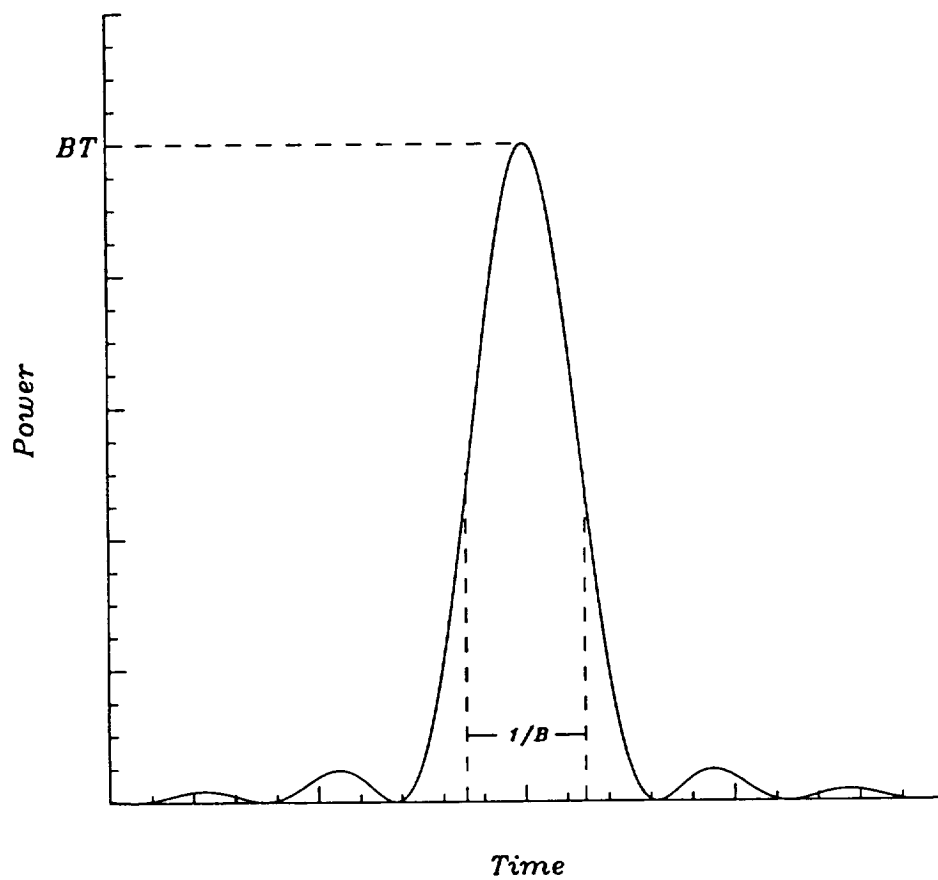


Figure 2.6. Example of a de-chirped pulse with duration $\frac{1}{B}$ and power BT [Skolnik, 1980].

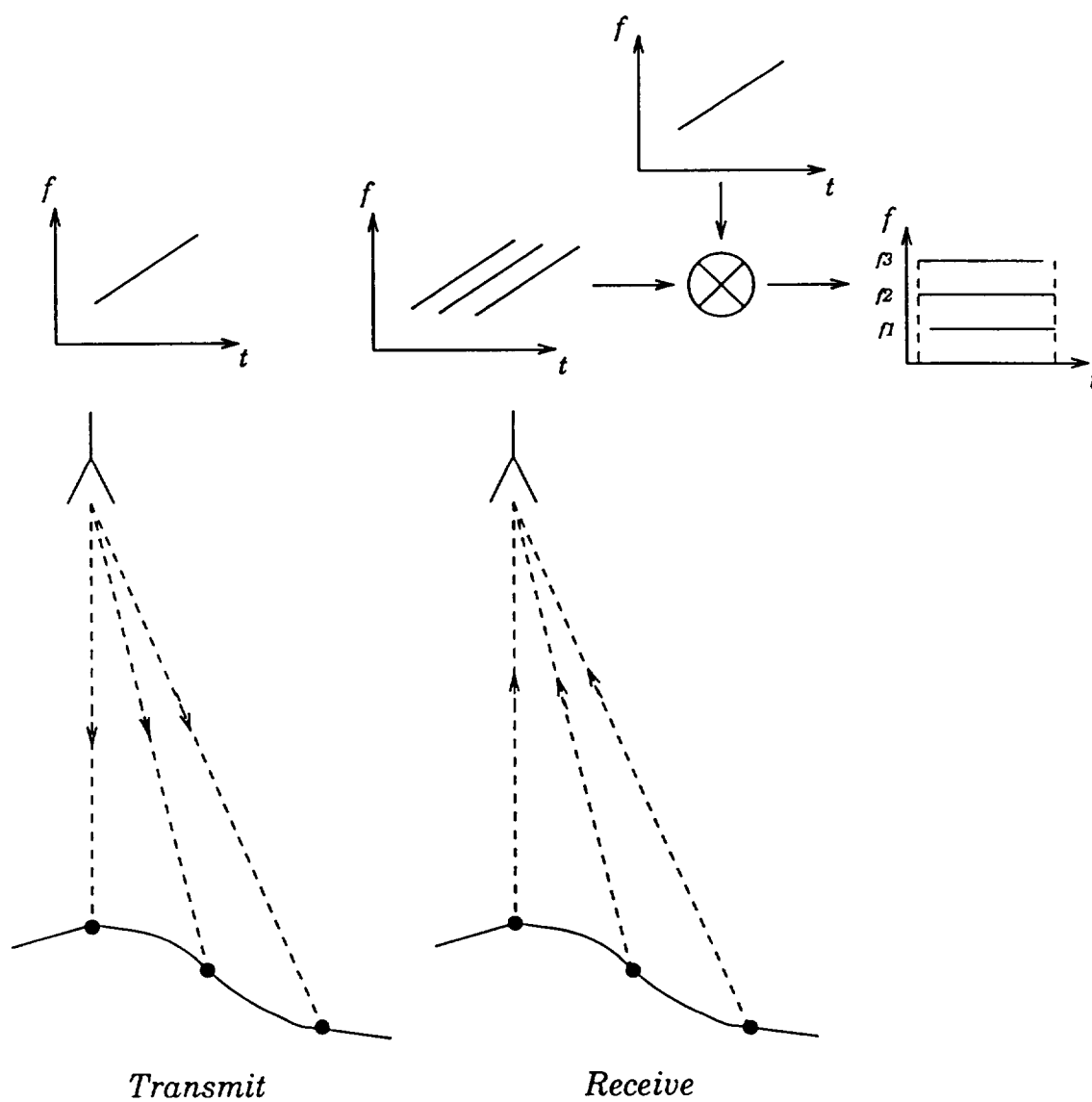


Figure 2.7. Illustration of full deramping and how it converts time delays into shifts in frequency [Rapley, 1990].

$$CR = \frac{T}{\tau} = TB. \quad (2.5)$$

The ERS-1 radar altimeter, for example, transmits a 20 μ sec chirp pulse with 300 MHz of bandwidth and 50 watts of power. Therefore, the effective pulse width of the radar is 3.3 nanoseconds and its CR is 6000, resulting in an effective transmitted power of 300 kilowatts [Rapley, 1990].

2.3 Mode of Operation

The two principle modes of operation in radar altimetry are the beam-limited mode and the pulse-limited mode. In the beam-limited mode, a narrow beam antenna is used to illuminate the entire radar footprint simultaneously. To meet this requirement, the excess slant range, ΔR , must not exceed the minimum rms surface height, $\sigma_{h \min}$, or

$$\Delta R < \sigma_{h \min}. \quad (2.6)$$

Figure 2.8 illustrates the geometry and requirements of the beam-limited mode of operation for a radar altimeter. Since the excess slant range is

$$\Delta R = R - h = \left(\frac{h}{\cos \theta} - h \right) \quad (2.7)$$

and θ is small, ΔR can be simplified to

$$\Delta R = 2h \left(\frac{\sin^2 \frac{\theta}{2}}{\cos \theta} \right) \approx \frac{h\theta^2}{2}. \quad (2.8)$$

Therefore, to meet the requirements of the beam-limited mode, the beamwidth of the antenna must be limited to

$$\theta < \sqrt{\frac{2\sigma_{h \min}}{h}}. \quad (2.9)$$

For the ERS-1 radar altimeter, which has $h = 777$ km, the maximum allowable beamwidth, assuming a minimum rms surface height of .5 meters, is 1.13 mrad or

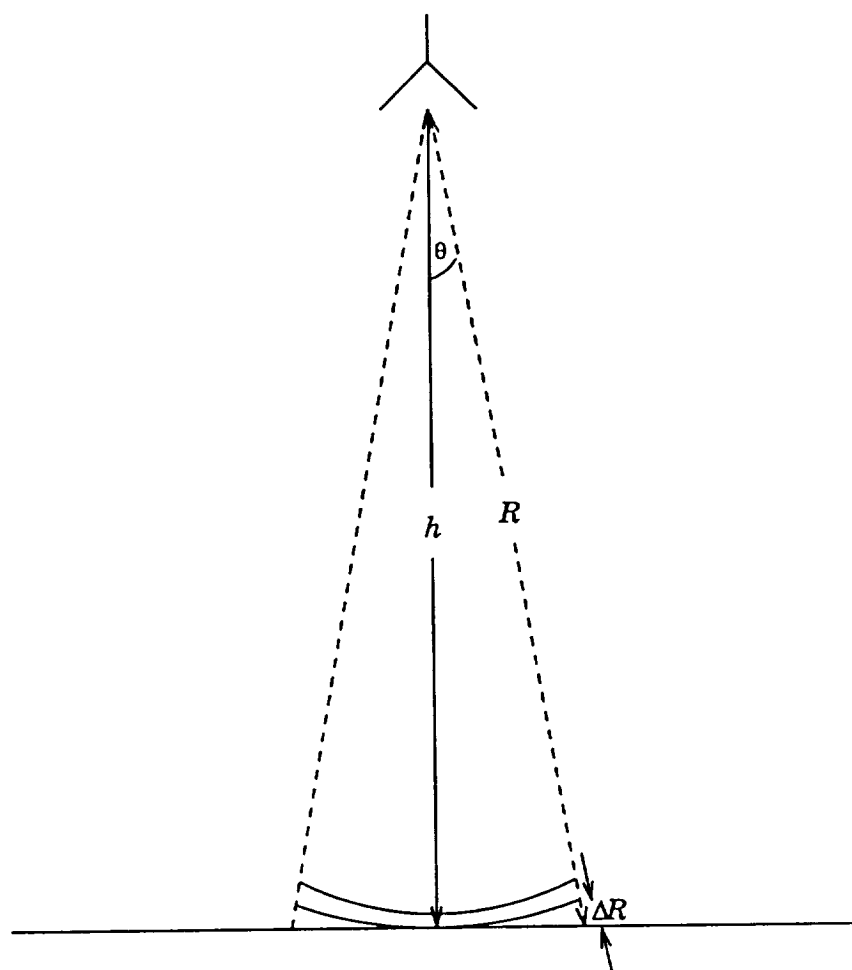


Figure 2.8. Geometry of the beam-limited mode of operation in radar altimetry [Rapley, 1990].

.06 degrees. Using the approximation $D \approx \frac{\lambda}{2\theta}$, where λ is 2.16 cm, the diameter of the beam-limited antenna has to be at least 9.5 meters. Because an antenna of this size is difficult and costly to put in space, the beam-limited mode of operation is impractical for spaceborne radar altimetry. It can, however, be used effectively in airborne applications. For example, a radar altimeter on an aircraft flying 450 meters above the surface only needs a .23 meter wide antenna.

Due to the shortcomings of the beam-limited mode, spaceborne applications usually use the pulse-limited mode for satellite radar altimetry. In this mode the antenna has a small aperture. As figure 2.9 shows, the resulting wide-beam makes the transmitted pulse expand out into a spherical shell as it propagates away from the radar. When the pulse intersects with the surface, it creates a circular footprint that grows larger in diameter with increasing time. Eventually, the trailing edge of the pulse reaches the surface at nadir and begins to reflect back. Once this occurs, the footprint becomes an annulus, which grows outward until it reaches the full extent of the antenna beam. Figure 2.10 illustrates the stages of the pulse-limited mode and the resulting area of the footprint versus time. The maximum circular area of the illuminated surface, which is noted as t_2 in figure 2.10, is called the pulse-limited footprint.

To achieve the pulse-limited mode, the excess slant range at the edge of the beam must be at least three times greater than the largest rms surface height, or

$$\Delta R > 3\sigma_{h\max}. \quad (2.10)$$

Using a similar analysis as in the beam-limited case, the resulting beamwidth must be

$$\theta > \sqrt{6\sigma_{h\max}}. \quad (2.11)$$

For a value of $\sigma_{h\max} = 5$ meters, the ERS-1 radar altimeter must have an antenna diameter less than .9 meters. Thus, the requirements for the pulse-limited mode are much easier to satisfy than those of the beam-limited mode [Rapley, 1990].

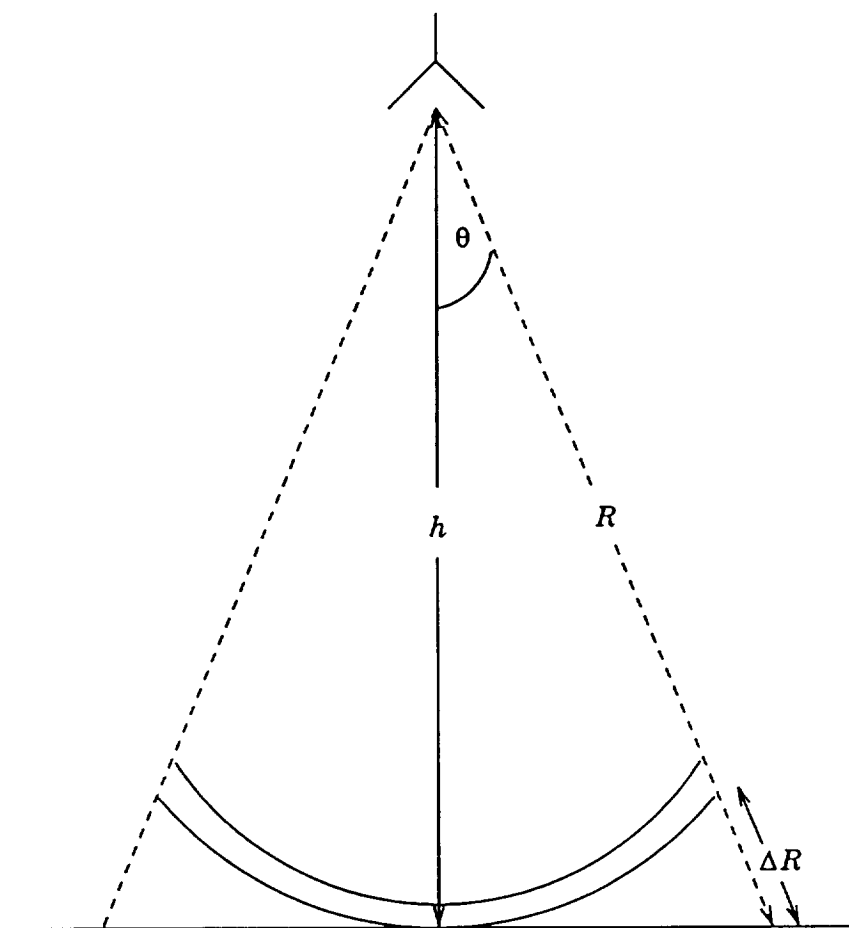


Figure 2.9. Geometry of the pulse-limited mode of operation in radar altimetry.

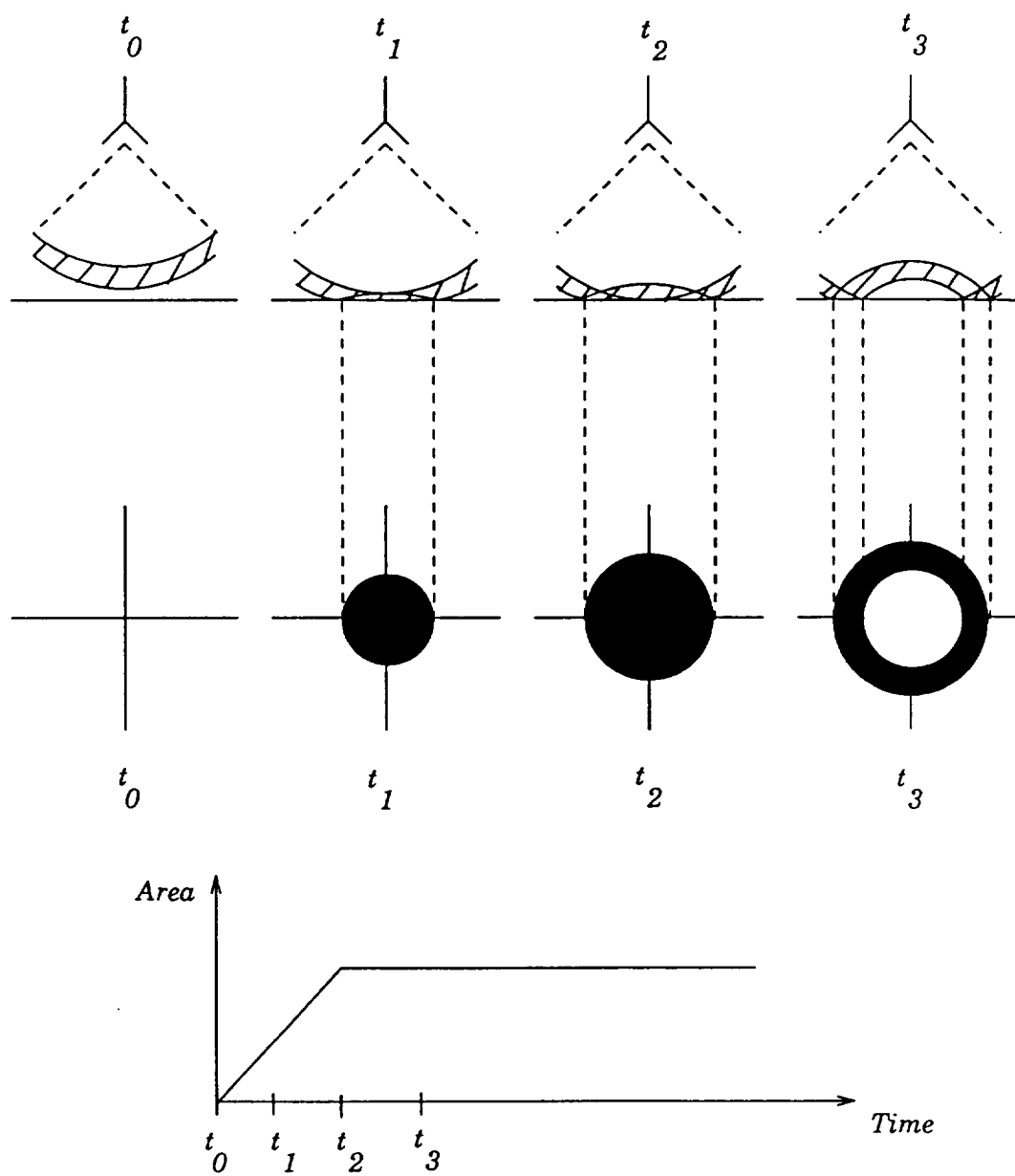


Figure 2.10. Stages of the illuminated footprint area in the pulse-limited mode of operation [Rapley, 1990].

When a radar altimeter is operating in the pulse-limited mode, the return waveform has a leading edge that rises in power as the area of the circular footprint increases until the full extent of the pulse-limited footprint has been reached. At this point, the illuminated area stays the same, but the return power begins to roll off due to the antenna gain pattern and increased range to the surface. Figure 2.11 shows a typical radar altimeter return waveform from the ocean and the footprint stages that contribute to its shape [McGoogan et al., 1974]. Since the return waveform depends on the size of the pulse-limited footprint (PLF), it is important to know the relationship between the effective transmitted pulse width, τ , and the area of the footprint. Figure 2.12 illustrates the geometry used for deriving the PLF area. The pulse-limited footprint is created from the time point N first receives the radar pulse at $t_1 = \frac{2h}{c}$, until it receives the back end of the pulse at $t_2 = \frac{2h}{c} + \tau$. At time t_2 , the pulse has reached as far out as point P, and the corresponding range it has traveled is

$$R = \frac{ct_2}{2} = \frac{c}{2} \left(\frac{2h}{c} + \tau \right) = h + \frac{c\tau}{2}. \quad (2.12)$$

The radius from point N to point P is

$$l = \sqrt{R^2 - h^2} \quad (2.13)$$

and the resulting pulse-limited footprint area is

$$\begin{aligned} A_f &= \pi l^2 = \pi(R^2 - h^2) = \pi \left(h c \tau + \frac{c^2 \tau^2}{4} \right) \\ &\approx \pi h c \tau \end{aligned} \quad (2.14)$$

[Rapley, 1990]. Therefore, a radar altimeter operating at an altitude of 450 m and transmitting a 2.7 nsec effective pulse would have a PLF area of 1145 m² and a radius of 19 m.

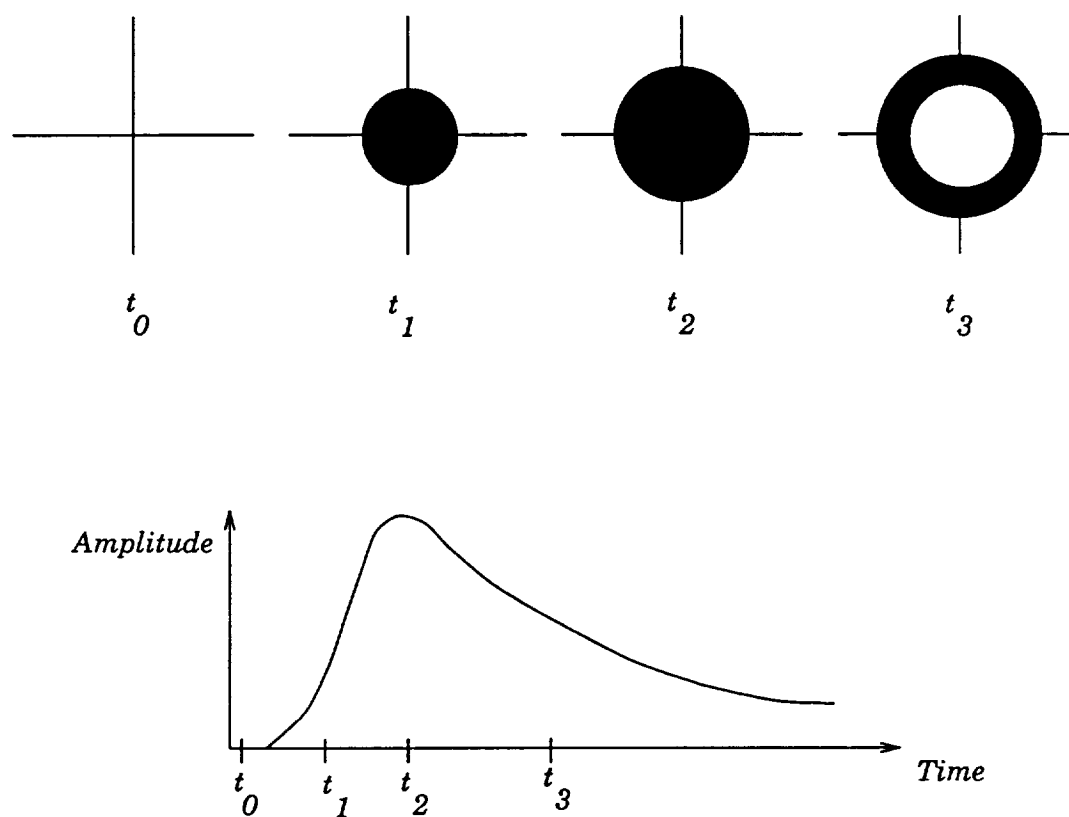


Figure 2.11. Effects of the footprint area on the radar altimeter return waveform.

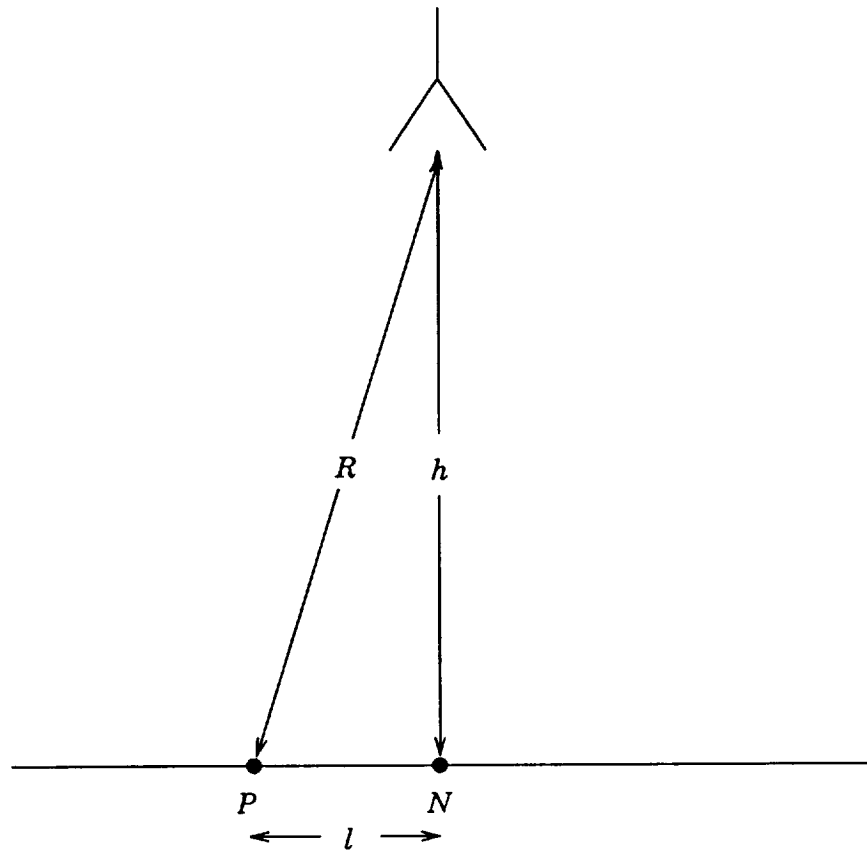


Figure 2.12. Geometry for deriving the area of the pulse-limited footprint, [Rapley, 1990].

CHAPTER 3

AAFE RADAR ALTIMETER SYSTEM

The Advanced Application Flight Experiment (AAFE) radar altimeter was built by Hughes Aircraft company for NASA Wallops Flight Facility in 1974. At this time the Skylab S-193 radar altimeter had demonstrated its ability to make spaceborne altimetry measurements with a 10 nsec transmitted pulse, and there was an increasing drive to achieve better range resolution. As a breadboard pulse compression radar, the AAFE radar altimeter accomplished this with a 1010:1 pulse compression ratio and an effective pulse width of 2.7 nsecs. The radar had many successful missions and demonstrated an altitude resolution of 2.1 cm over the ocean and a 10% sea wave height estimation accuracy [NASA, 1976]. One of the limitations of the AAFE radar altimeter, however, was that it had only 24 range bins, resulting in a 10 meter range window. This limited the tracking ability of the radar, causing it to lose lock over any rapidly changing surface. As a result, the radar was primarily used for oceanographic purposes.

In 1990, the AAFE altimeter was donated to the Microwave Remote Sensing Laboratory at the University of Massachusetts at Amherst. By this time, the analog/digital subsystem of the radar and its computer subsystem, which contained a teletype, a magnetic tape drive and a tape punch reader, had become obsolete, so the University of Massachusetts refurbished the entire radar system. One of the major improvements was an increase in its range window size to 88 meters. This allowed the radar to track over rapidly changing topographical surfaces such as glaciers, sea ice and land. Recent advances in digital technology allowed the new system to digitize each return waveform and store the entire result for post

processing. Figure 3.1 shows the amount of waveform processed and stored by the original AAFE system and by the refurbished radar. This refurbishment converted the AAFE altimeter to a high resolution radar system with robust tracking ability and advanced computing, storage and data display capabilities.

3.1 Radar System Hardware

A simplified block diagram of the entire AAFE system is illustrated in figure 3.2. The transmitter subsystem contains the IF and RF components that create the 13.9 GHz chirp, which is then transmitted from a horn antenna. After the signal has returned from its target, it passes back through the antenna and into the receiver subsystem. Here the RF and IF stages convert the signal down to baseband and send it onto the data acquisition subsystem, which consists of a digitizer and a vector signal processor (VSP). Once the digitizer has converted the signal into a digital waveform, the VSP board takes a Fast Fourier Transform (FFT) of the result and then averages several waveforms to reduce noise. The final processed waveform is then passed to the computer subsystem, consisting of a Hewlett Packard computer, a hard drive and an optical drive. The computer stores the waveform along with the system parameters and also sends it to the tracking subsystem. This software routine decides what changes need to be made to the system to maintain lock. The control subsystem takes the results of the tracking subsystem and makes the necessary adjustments to the transmitter and receiver. Changes can also be made by the user from the computer. The desired modifications are passed onto the control subsystem or the data acquisition system to update parameters such as sampling rate, PRF and radar calibration.

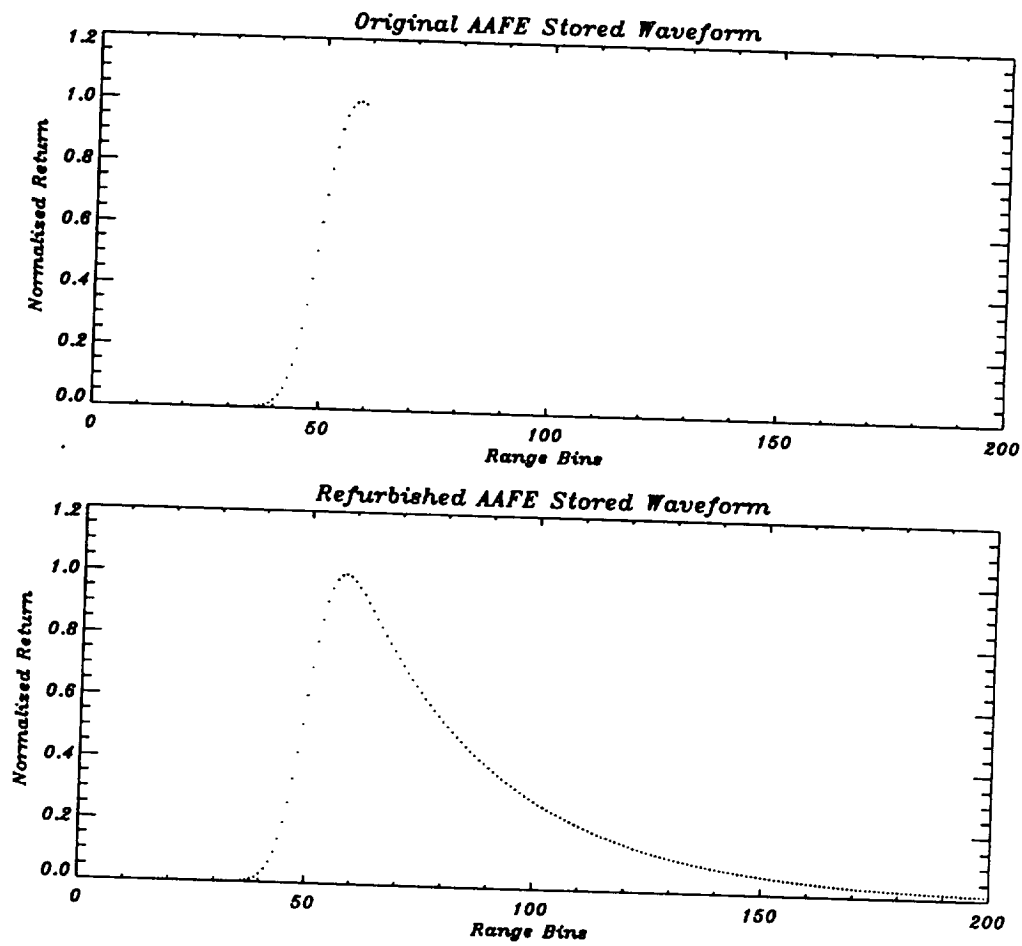


Figure 3.1. Comparison of the original AAFE system waveform (top waveform) and the refurbished AAFE system waveform (bottom waveform).

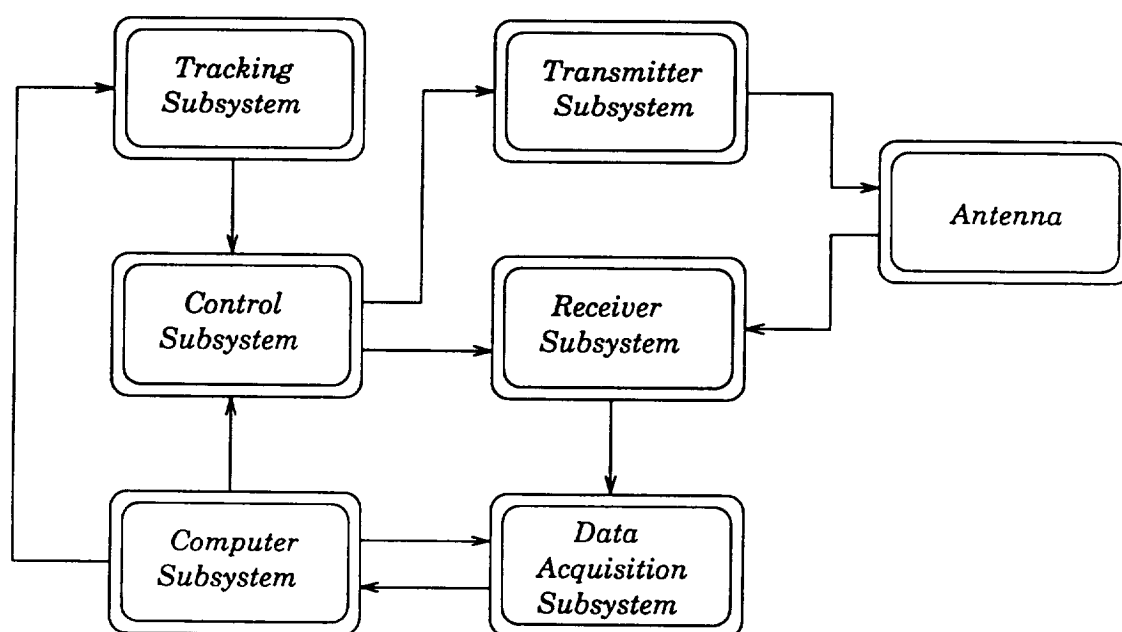


Figure 3.2. A simplified block diagram of the entire AAFE radar altimeter system.

3.1.1 Transmitter Subsystem

The transmitter of the refurbished AAFE radar altimeter, shown in figure 3.3, is very similar to that of the original system. In this subsystem, a 108 MHz oscillator source is multiplied by 5 to generate a 540 MHz signal and divided by 4 to create a 27 MHz signal. The 540 MHz CW signal is passed into a spectrum generator that creates a 5 nsec pulse when triggered by the control subsystem. This narrow pulse provides the necessary bandwidth for the reflective array compression (RAC) device to produce a 3 μ sec chirp with 180 MHz of bandwidth and a center frequency at 540 MHz. Figure 3.4 shows the frequency domain output of the RAC taken on a spectrum analyzer. A frequency doubler following the RAC increases the bandwidth to 360 MHz and the center frequency to 1080 MHz. Since a 3 μ sec pulse is 450 meters long, the aircraft must fly at least 450 meters above the surface to enable the entire pulse to leave the system before it is received. To allow instrument operation at lower altitudes, a RF switch placed after the frequency doubler can cut the pulse width down to any duration as small as .25 μ secs. This enables the AAFE altimeter to operate as low as 278 meters. Cutting the pulse width, however, reduces the bandwidth of the chirp and therefore increases the effective pulse width and range resolution.

The power splitter that follows the pulse width switch allows the pulse to take either the chirp or the de-chirp path. The chirp path consists of amplification followed by mixing with a 12.82 GHz local oscillator. The resulting 13.9 GHz signal receives 57 dB of amplification from a travelling wave tube (TWT), and is sent through a circulator and on to the antenna. The de-chirp signal, on the other hand, is mixed with the 540 MHz CW signal to create a 1620 MHz de-chirp pulse. This signal along with the 12.82 GHz LO and a 567 MHz signal, created by mixing the 27 MHz and 540 MHz signals, are passed on to the receiver.

A calibration switch located before the circulator also allows the radar to operate

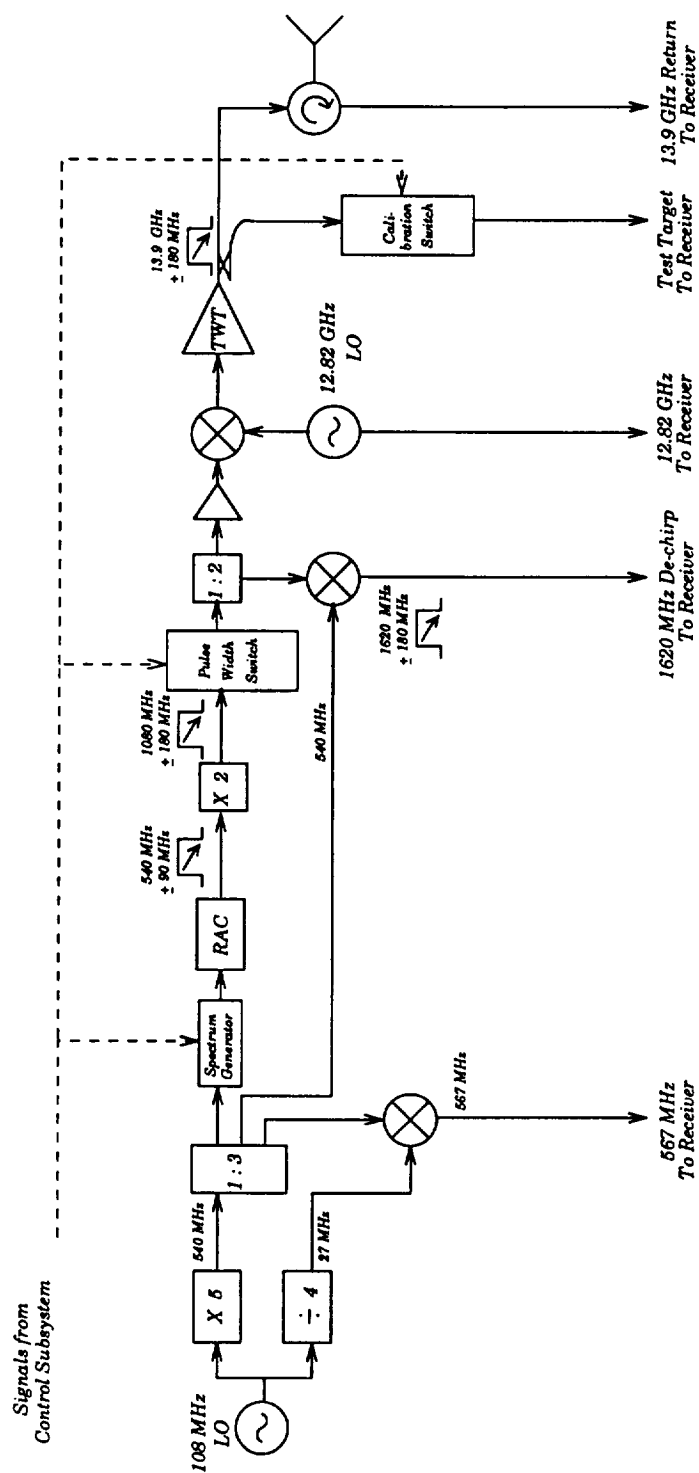


Figure 3.3. Block diagram of the AAFE transmitter subsystem [NASA, 1976].

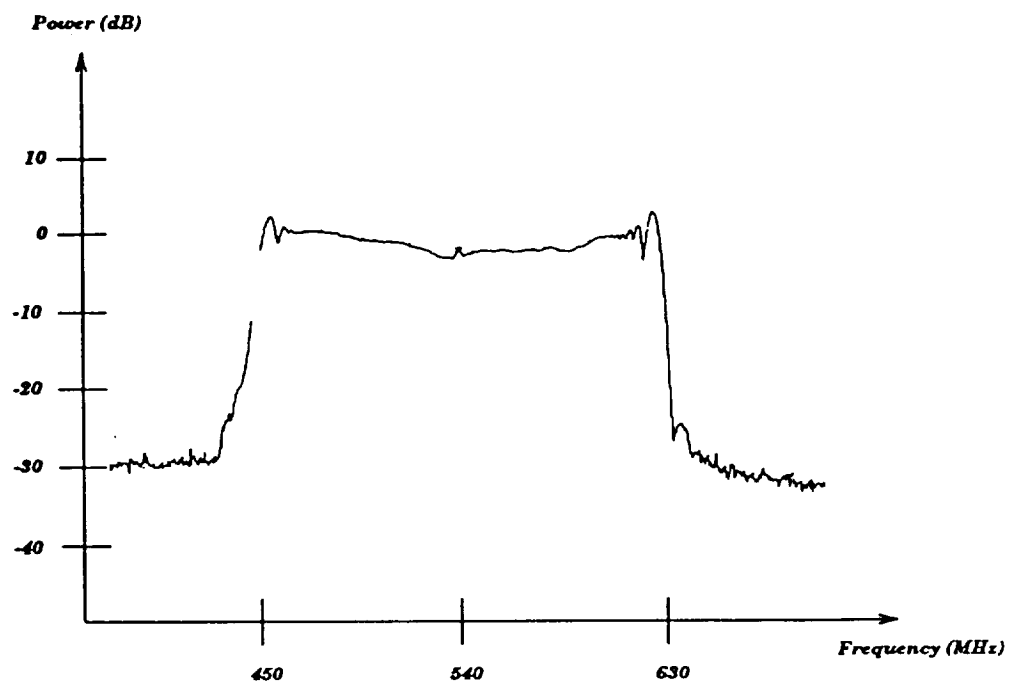


Figure 3.4. Output of AAFE RAC device measured with a spectrum analyzer.

in a calibration mode, in which the chirp by-passes transmission to the antenna and instead is attenuated by 80 dB before being sent to the receiver subsystem.

3.1.2 Antenna

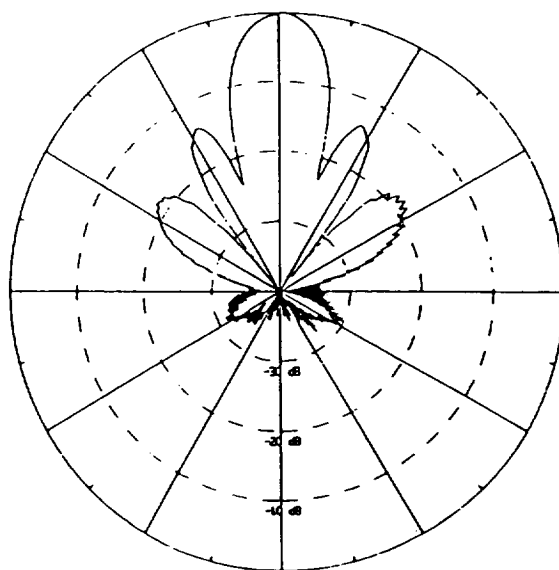
The main antenna used in the AAFE radar system is an optimum gain pyramidal horn with a one way 3 dB beamwidth of 15.6 degrees and a gain of 21.6 dB. Figures 3.5a and 3.5b show the gain patterns of this antenna in the E and H-planes, respectively. The wide beam of the horn allows the antenna to operate in the pulse-limited mode at aircraft elevations as low as 270 meters if the maximum surface roughness is 3 meters and, as figure 3.6 shows, its small size enables easy installation.

In order to investigate volume scattering from glacial ice, a wider beam antenna with a 31.2 degree beamwidth was developed for the AAFE altimeter. This antenna, which has half the aperture of the main antenna and therefore twice the beamwidth, allows additional volume scattering returns to be received from angles far from nadir. A narrow beam antenna was also designed and built to enable the AAFE altimeter to maintain lock over mountainous areas and from high altitudes. This patch phased array has a beamwidth of 4 degrees and a gain of 34 dB.

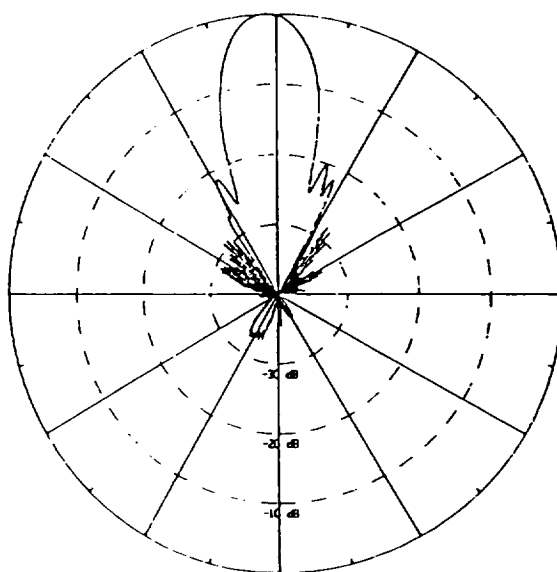
3.1.3 Receiver Subsystem

Figure 3.7 is a block diagram of the original AAFE receiver. The 24 ramp filters, 13 tracking filters and 27 detectors made the receiver bulky and inefficient. The hardware filters also limited the size of the range window of the instrument. When the AAFE radar altimeter was refurbished, significant changes were made to the receiver subsystem. As figure 3.8 shows, the refurbished system performs the filtering and tracking in software.

Figure 3.8 also illustrates the processing of the received signal. When the return chirp comes from the antenna, it passes through the circulator and is mixed down



(a)



(b)

Figure 3.5. (a) The E-plane gain pattern of the main AAFE horn antenna and (b) the H-plane gain pattern of the main AAFE horn antenna.

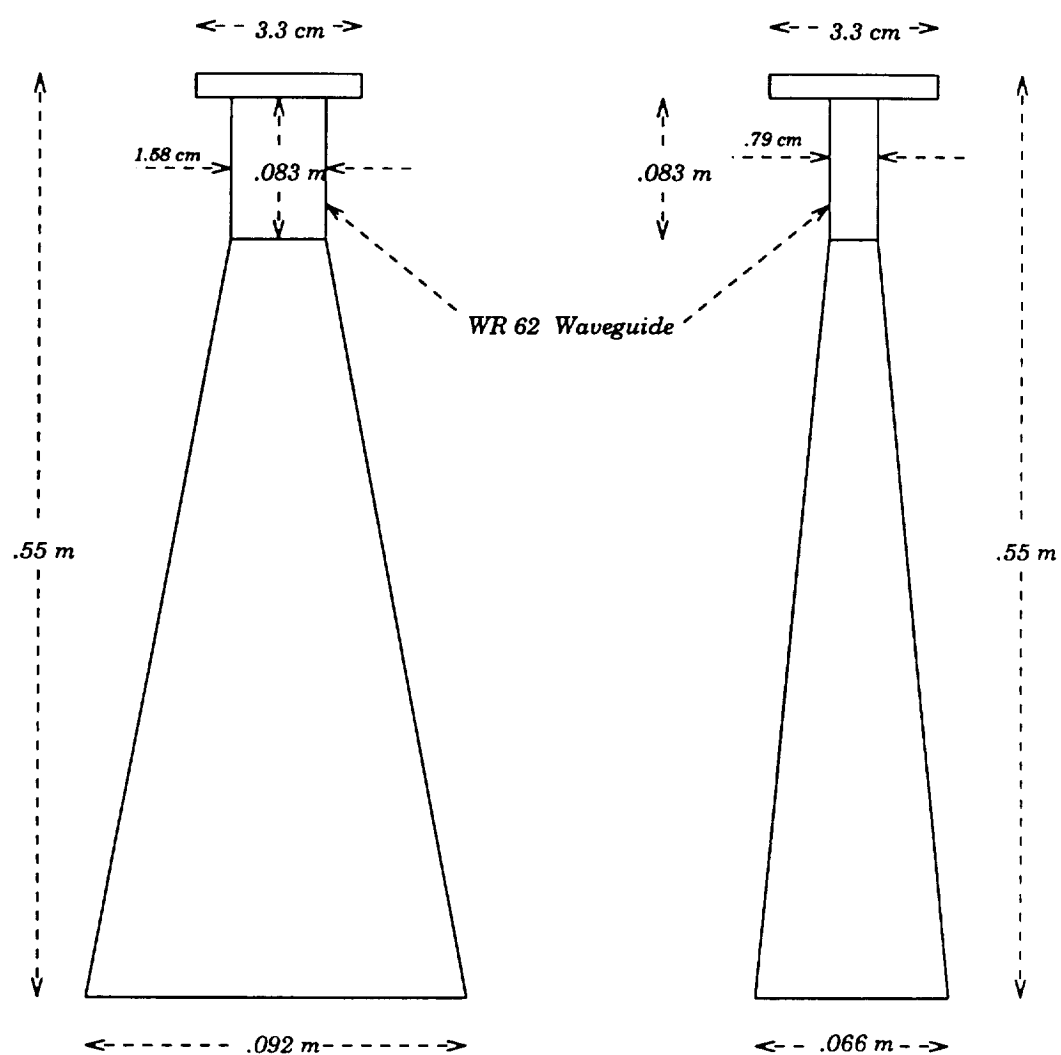


Figure 3.5. Diagram of the main AAFE horn antenna.

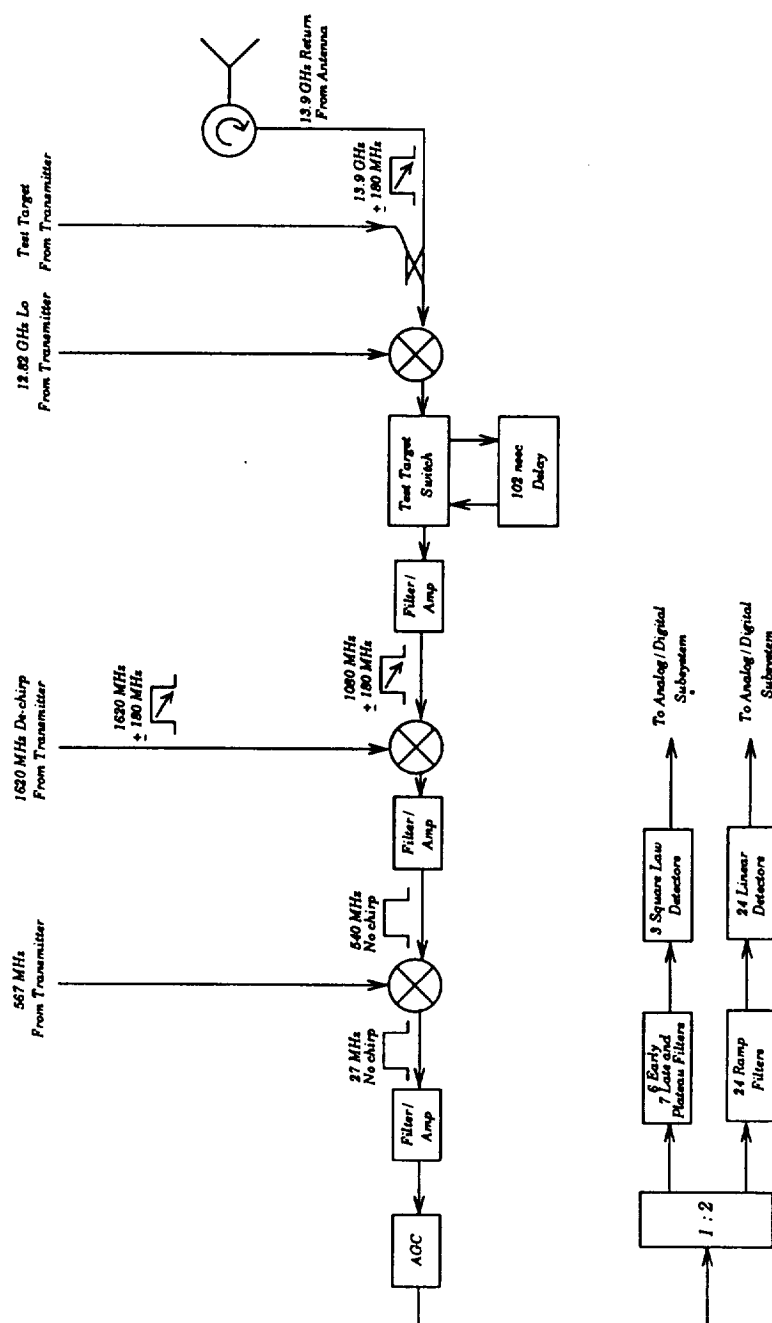


Figure 3.7. Block diagram of the original AAFE receiver subsystem [NASA, 1976].

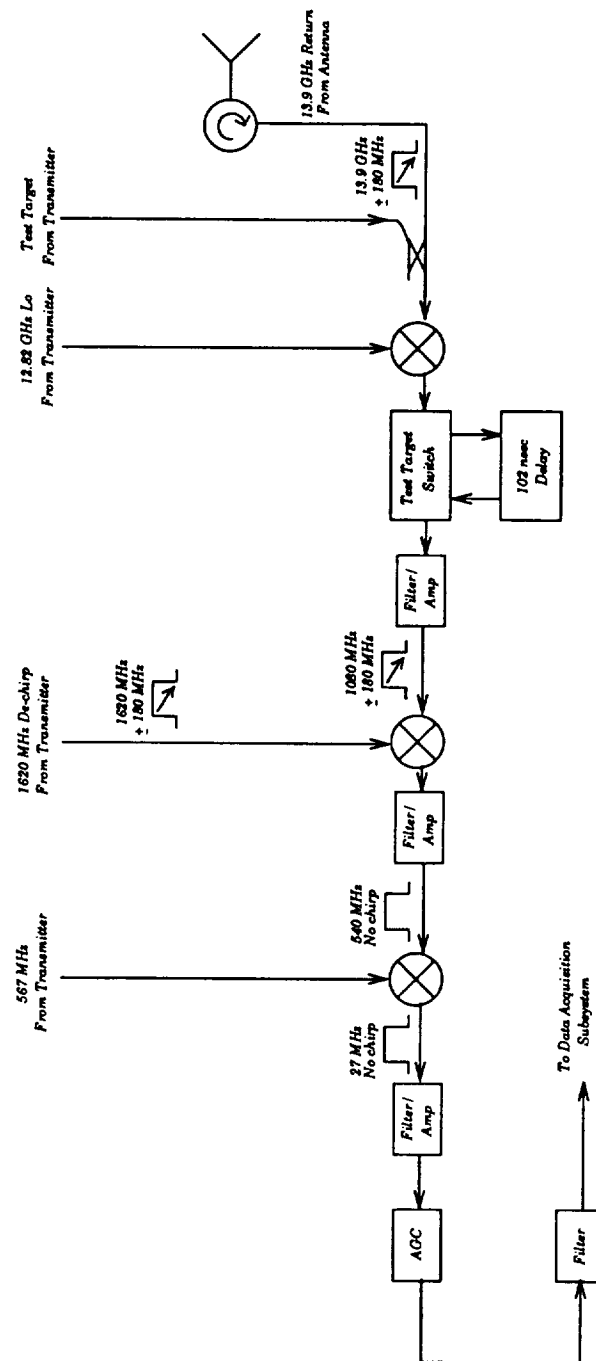


Figure 3.8. Block diagram of the refurbished AAFE receiver subsystem.

to 1080 MHz. A pair of manual attenuators after the mixer allow the user to adjust the signal strength entering the receiver according to the reflectivity of the surface below. This prevents saturation of the receiver front end amplifiers. When operating in the calibration mode, the test target switch in the receiver can be used to send the signal through a 102 nsec delay line. In normal operation, however, the chirp is just filtered and amplified before being mixed with the 1620 MHz de-chirp pulse. The result is a 540 MHz pulse with no chirp. It is at this point that delays in range are converted to shifts in frequency or, as explained in section 2.2, the signal is deramped. An example of this process is shown in figure 3.9, where the returns from 3 discrete scatterers separated by 45 cm in range are received 3 nsecs apart. If the second return is perfectly aligned in time with the 1620 MHz de-chirp, the first return will be at $540 \text{ MHz} + 360 \text{ kHz}$, the second will be at 540 MHz and the third will be at $540 - 360 \text{ kHz}$ [NASA, 1976]. Thus, as figure 3.9 shows, it is essential that the de-chirp pulse is timed to reach the mixer when the chirp is arriving, otherwise this deramping method will not work. The tracking subsystem of the altimeter is responsible for aligning the two signals and therefore keeping the system in lock.

Once the chirp has been removed, the signal is filtered, amplified and mixed down to baseband. A single IF filter was added to the receiver so that the signal has a bandwidth ranging from 5 MHz to 75 MHz. Since range delays have been converted to frequency offsets, the desired AAFE return waveform is now in the frequency domain. Before going to the data acquisition subsystem, this signal is attenuated by the automatic gain control (AGC) to prevent saturation of the digitizer.

3.1.4 Data Acquisition Subsystem

The data acquisition subsystem consists of an Analytek Series 2000B Waveform Acquisition System and an Impact Technologies Viper 8704/30-30 vector signal processor. As figure 3.10 shows, this subsystem is packaged in two 5-slot VME

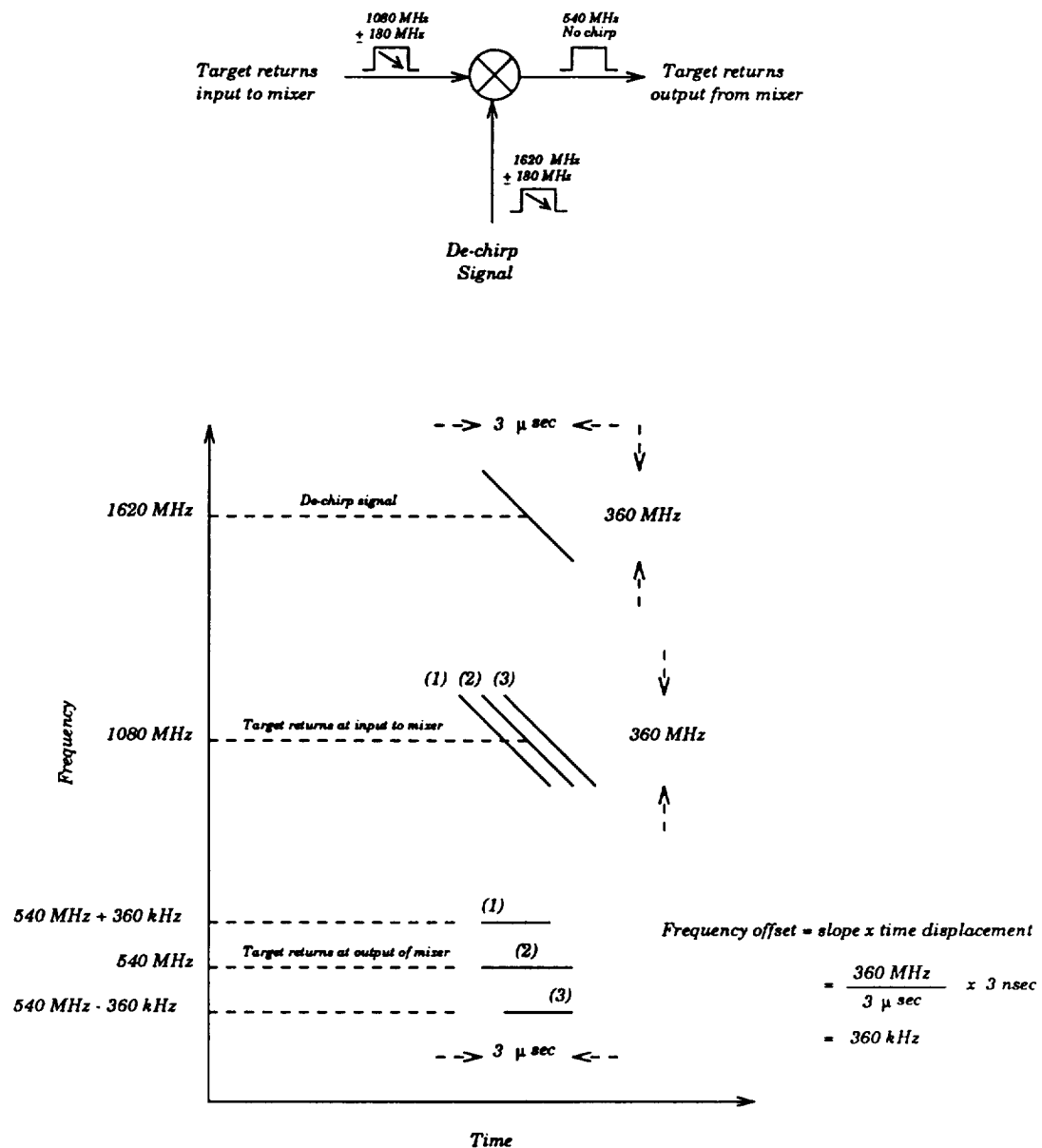


Figure 3.6. Example of how the AAFE altimeter converts delays in range to shifts in frequency [NASA, 1976].

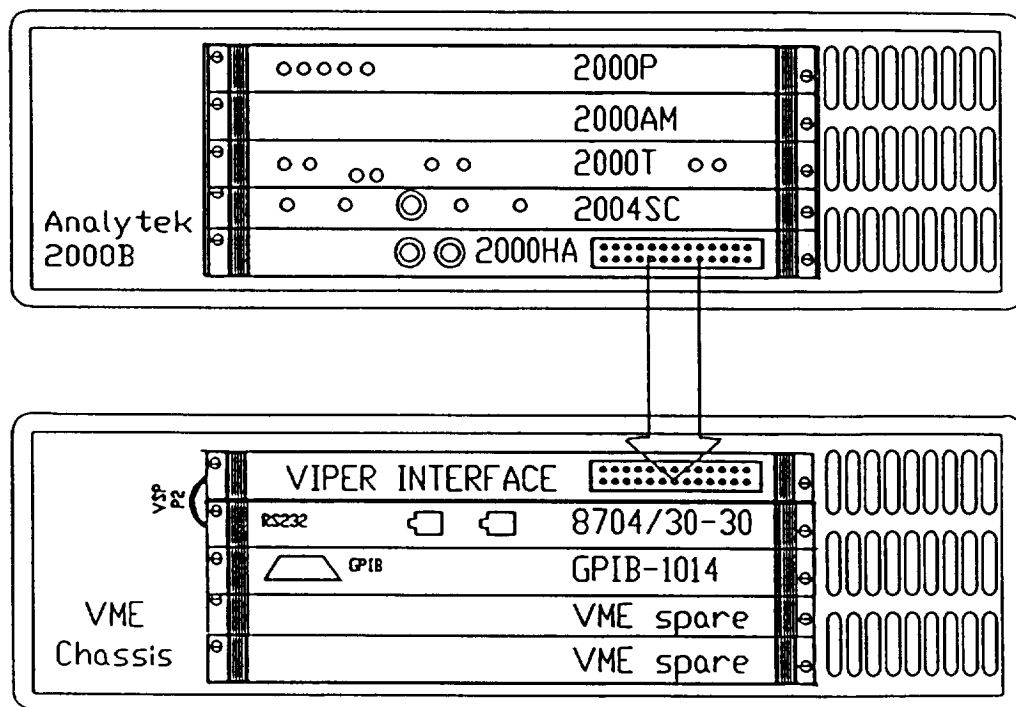


Figure 3.10. Simplified block diagram of the AAFE altimeter data acquisition subsystem.

chassis. The top chassis contains the Analytek 12-bit digitizing system, which has five separate modules, the 2000P, 2000AM, 2000T, 2004SC and 2000HA. When the signal coming from the receiver subsystem enters the 2000HS1 sampling card (consisting of the 2004SC and the 2000HA), its highest frequency is 75 MHz, so it must be sampled at a minimum rate of 150 MHz [Haykin, 1989]. Since the internal 1 GHz clock provided by the 2000T timing module can only be divided by integer multiples, a value of $\frac{1\text{GHz}}{6}$ or 166.67 MHz was chosen as the sampling rate. As each signal enters the system, it is captured by the 2004SC sampling unit and then sent to the 2000HA high throughput accelerator module, which performs the digital conversion, data correction and fast data transfer. All processing is managed and controlled by the 2000P processor module, and the remaining 2000AM air module is just a cover for the empty chassis slot [Analytek, 1991].

Each pulse entering the Analytek digitizer has a duration of 3 μsecs and therefore a minimum of 3 $\mu\text{sec/pulse} \times 166 \text{ Msamples/sec}$ or 500 samples/pulse must be taken. Since the Analytek uses powers of two for the sample count setting, a value of 512 samples/pulse was chosen. The repetition rate of the radar altimeter may be set to any value, but it is typically run between 750 Hz and 1250 Hz, so there are approximately 800 to 1333 μsecs between each incoming pulse. During this time the 2000HA off loads the digitized pulse via a high speed parallel port that handles up to 3.8 Mwords/sec. All parameters of the Analytek digitizer are set from the HP computer over a GPIB IEEE 488 bus. Additional information about the Analytek system can be obtained in the Analytek Limited Series 2000 Waveform Sampler Systems Operations Manual [Analytek, 1991].

A data interface card in the bottom 5-slot VME chassis receives the data from the Analytek 2000HA and sends it on to the Viper 8704/30-30. This board contains four vector signal processors running at 30 MHz and an on-board 68030 operating at 25 MHz [Impact, 1987]. The vector signal processors perform a Papoulis window

[Papoulis, 1973] and then a 512 point FFT on each one of the incoming digitized waveforms. Since the 512 point FFT returns 256 points in the positive frequency domain and 256 points in the negative frequency domain, only the positive ones are used. As a result, the frequency domain resolution is $\frac{1}{3 \mu\text{sec}} = 333 \text{ kHz}$ and the bandwidth is $256 \times 333 \text{ kHz} = 85.25 \text{ MHz}$. Each FFT point represents a range bin equivalent to $333 \text{ kHz} \times \frac{3 \mu\text{sec}}{360 \text{ MHz}} = 2.77 \text{ nsecs}$, or 41.67 cm. Since the original bandwidth is from 5 MHz to 75 MHz, the waveform lies between bins #15 and #225 creating a range window that is 210 range bins or 87.5 meters wide. After performing the FFT, the VSP board averages several waveforms together to reduce noise and then sends the data to the HP computer using a National Instruments VME GPIB-1014 DMA interface card and a GPIB IEEE 488 bus. All of the assembler language software for the Viper board is loaded from the HP computer over a RS-232 port. This allows the user to enter the amount of averaging as either 1, 16, 32, 64, 128, 256 or 512. Typically, averaging 64 waveforms produces a clean enough waveform to run the tracker and maintain lock, except at altitudes above 3500 meters when the number of averages may have to be increased. Additional information about the VSP board can be found in the Impact Technologies Viper 8704/30 User's Manual [Impact, 1987] and the Impact Technologies 161ASM User's Manual [Impact, 1988].

3.1.5 Tracking Subsystem

To keep the de-chirp pulse of the altimeter aligned with the return chirp pulse when the range to the surface fluctuates, a tracking routine must be run on each stored AAFE waveform. This routine, which is run in the HP computer software, attempts to keep a point on the leading edge of the return waveform located at the center bin of the range window. If the return from a single point scatterer aligns with the de-chirp pulse perfectly, the result is an impulse at 27 MHz, therefore, the center bin is at 27 MHz or bin #81. When a return waveform is displayed, however,

this center bin is often called bin #0. The AAFE range window was designed to have more range bins to the right of the center bin because return waveforms usually have long trailing edges.

Tracking routines find a specific point on the return waveform, such as the half power point, and then determine the distance from this point to the center bin. As shown in figure 3.11, the resulting ΔR , or the track bin minus the center bin, is the amount of adjustment that should be made to the de-chirp pulse. If ΔR is positive or the waveform is too far to the right, the de-chirp pulse must be sent later because the range to the surface is increasing. Similarly, if ΔR is negative the de-chirp must be sent earlier due to a decrease in altitude. Since the AAFE altimeter has such a large range window, the radar stays in lock as long as the waveform is kept within approximately 15 meters or 36 range bins of the center bin.

During the past 20 years several tracking routines have been developed to keep the leading edge at the center bin and therefore the entire waveform in the range window. The AAFE radar altimeter allows the user to choose from several tracking routines, such as a maximum value tracker, an offset center of gravity (OCOG) tracker and a weighted split-gate (WSG) tracker. The maximum value tracker takes the waveform points, which are stored in an array, and finds the maximum point in that array. This point corresponds to the peak of the return waveform and, as figure 3.12a shows, the tracker uses its location as the track bin. Since the maximum value tracker is simple and takes little computation time, it is very efficient. It should only be used, however, over smooth, slowly varying, highly reflective surfaces where the return waveform is clean and has a high signal-to-noise ratio.

The offset center of gravity (OCOG) tracker, which was developed by the Mullard Space Science Laboratory, uses an estimate of the pulse width to track the return waveform. The width of the pulse, W , is approximated using

$$W = \frac{(\sum_{n=0}^{k-1} p_n)^2}{\sum_{n=0}^{k-1} p_n^2} \quad (3.1)$$

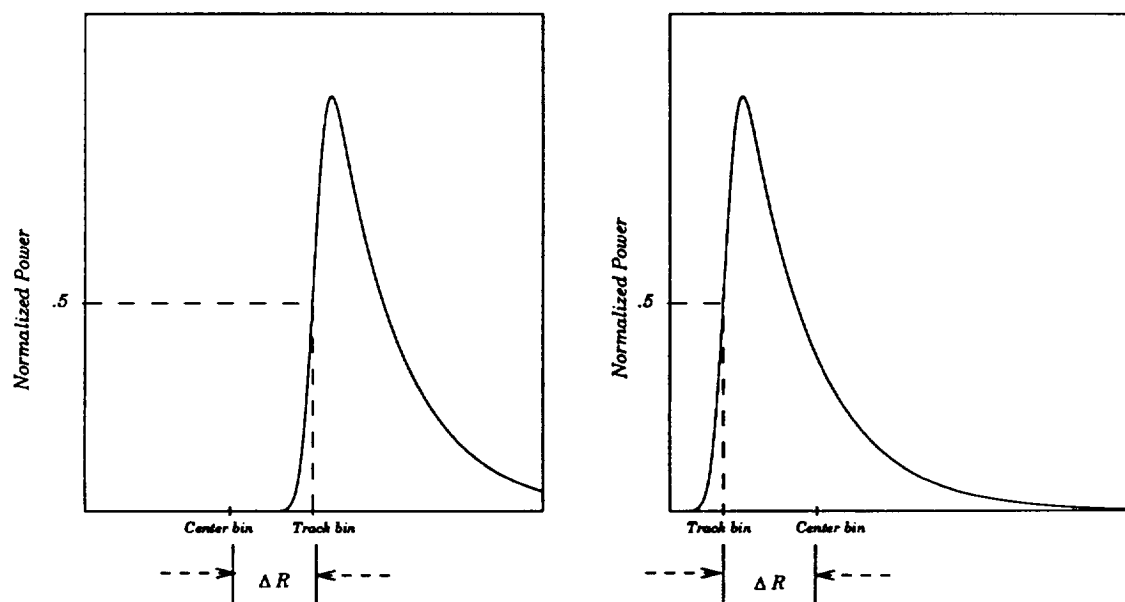


Figure 3.8. Examples of how the tracking subsystem keeps a waveform in the range window of the altimeter.

where k is the total number of range bins and p_n is the power in range bin n . Since the waveform is stored as an array, p_n is the value of the n th element of the array. For example, a pulse defined as

$$p_n = \begin{cases} A & m \leq n < m + j \\ 0 & \text{otherwise} \end{cases} \quad (3.2)$$

results in $W = j$. The OCOG tracker then calculates the center of area of the pulse as

$$\frac{\sum_{n=0}^{k-1} n p_n}{\sum_{n=0}^{k-1} p_n} - \frac{W}{2} \quad (3.3)$$

[Wingham et al., 1986] and uses the result as the track bin. Figure 3.12b shows a model altimeter return waveform and the resulting OCOG track bin location. The OCOG tracker works well with all types of waveform shapes, such as sea ice, glacial ice and ocean returns, and also with waveforms that have low signal-to-noise ratios.

The AAFE system also has the weighted split-gate (WSG) tracker, which attempts to keep a fixed ratio of power in the two halves of the range window, or

$$\text{track bin - center bin} = \frac{a \sum_{n=0}^{c-1} p_n - b \sum_{n=c}^{k-1} p_n}{2 \max(p_n)} \quad (3.4)$$

where c is the center bin and the weighting ratio is $a:b$. Typical values for a and b are .5 and 1.5 respectively, resulting in a weighting ratio of 1:3. The problem with the WSG tracker is that it works well only if a portion of the pulse is on each side of the center bin [Wingham et al., 1986].

All of the trackers in the AAFE tracking subsystem check the ratio of maximum to minimum power in the range window for each waveform. When this ratio is less than 2 dB, the tracker assumes that the waveform is either extremely noisy or non-existent. If this occurs for ten consecutive waveforms, the tracker determines that the radar altimeter is no longer in lock and it enters the acquisition mode.

Each of the above trackers determines the range error, ΔR , for a single return waveform. When rapidly varying terrain requires frequent updates to the de-chirp

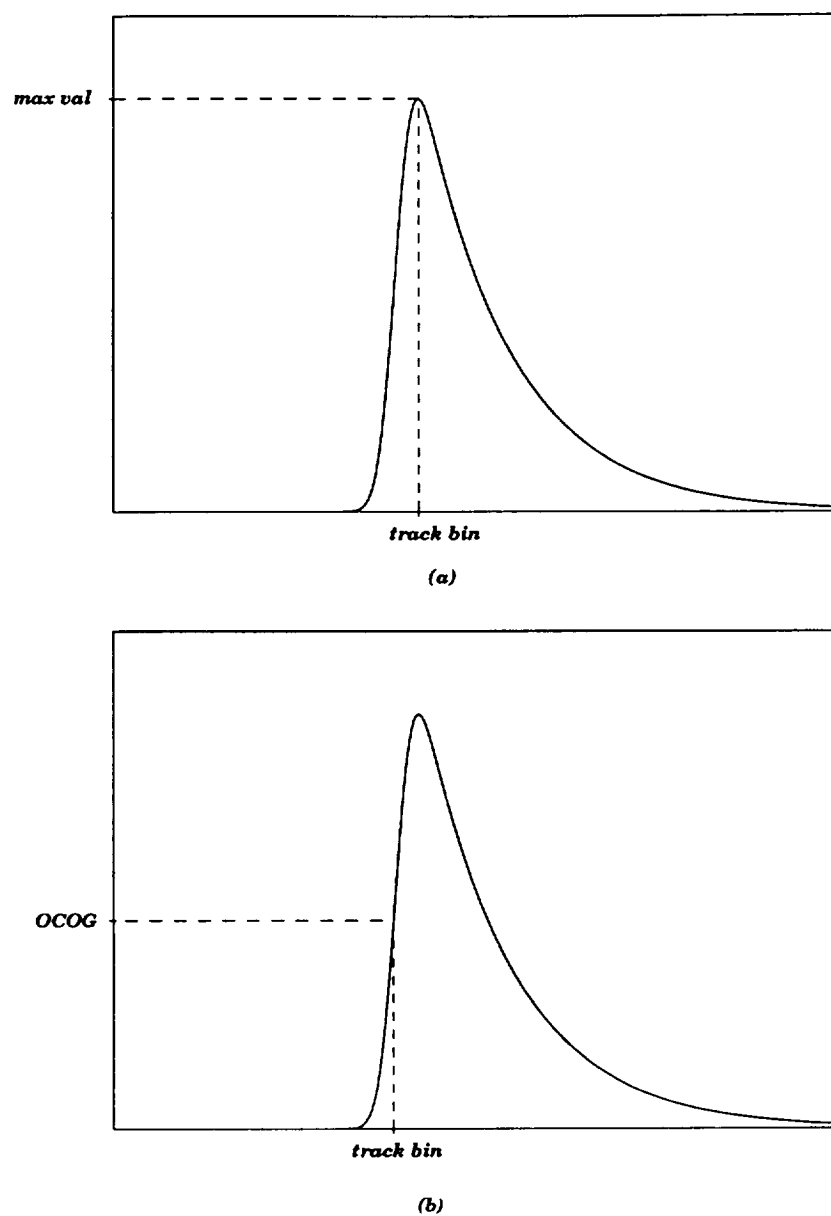


Figure 3.9. Illustration of (a) the maximum value tracker and (b) the OCOG tracker used in the AAFE altimeter tracking subsystem.

pulse, a tracking filter such as a two-pole or alpha-beta filter can be implemented. By using previous waveform range errors along with the current waveform error to determine the update to the de-chirp pulse, the filter smoothes the transitions from pulse to pulse and prevents the system from going into oscillations [Rapley et al., 1983].

Additional trackers, such as terrain and sea ice trackers, can be easily added to the AAFE tracking subsystem, as well as new smoothing techniques like Kalman filtering. When tracking return waveforms, however, it is only necessary to keep the waveform in the range window and not exactly at the center bin because all return waveforms are retracked or post-processed at a later time to obtain a more accurate altitude measurement. Retracking methods are discussed in greater detail in Chapter 5.

The acquisition time of the tracking subsystem is the time it takes the radar to initially obtain lock on the surface. Currently, the AAFE altimeter uses an incremental step method of acquiring lock. When the instrument enters the transmit mode, the user is asked for a maximum and minimum flight altitude. Once in the acquisition mode, the radar starts sending the de-chirp pulse at a time equivalent to the entered minimum range. The resulting return waveform is run through the OCOG tracker to determine the bin error, ΔR . The de-chirp pulse is then moved to the minimum range plus the step range and again run through the tracker to determine ΔR . This process is repeated at every incremental range up to the maximum range, then the step with the minimum ΔR is used as the acquisition range and the radar enters the normal transmit and track mode. Figure 3.13 illustrates a series of return waveforms in the acquisition mode acquired at increasing increments of 20 meters.

The total acquisition time for this method is

$$\text{Acq time} = \frac{(\text{max height} - \text{min height})}{\text{step size}} \times \left(\frac{1}{PRF} \times \text{num avgs} \right) \quad (3.5)$$

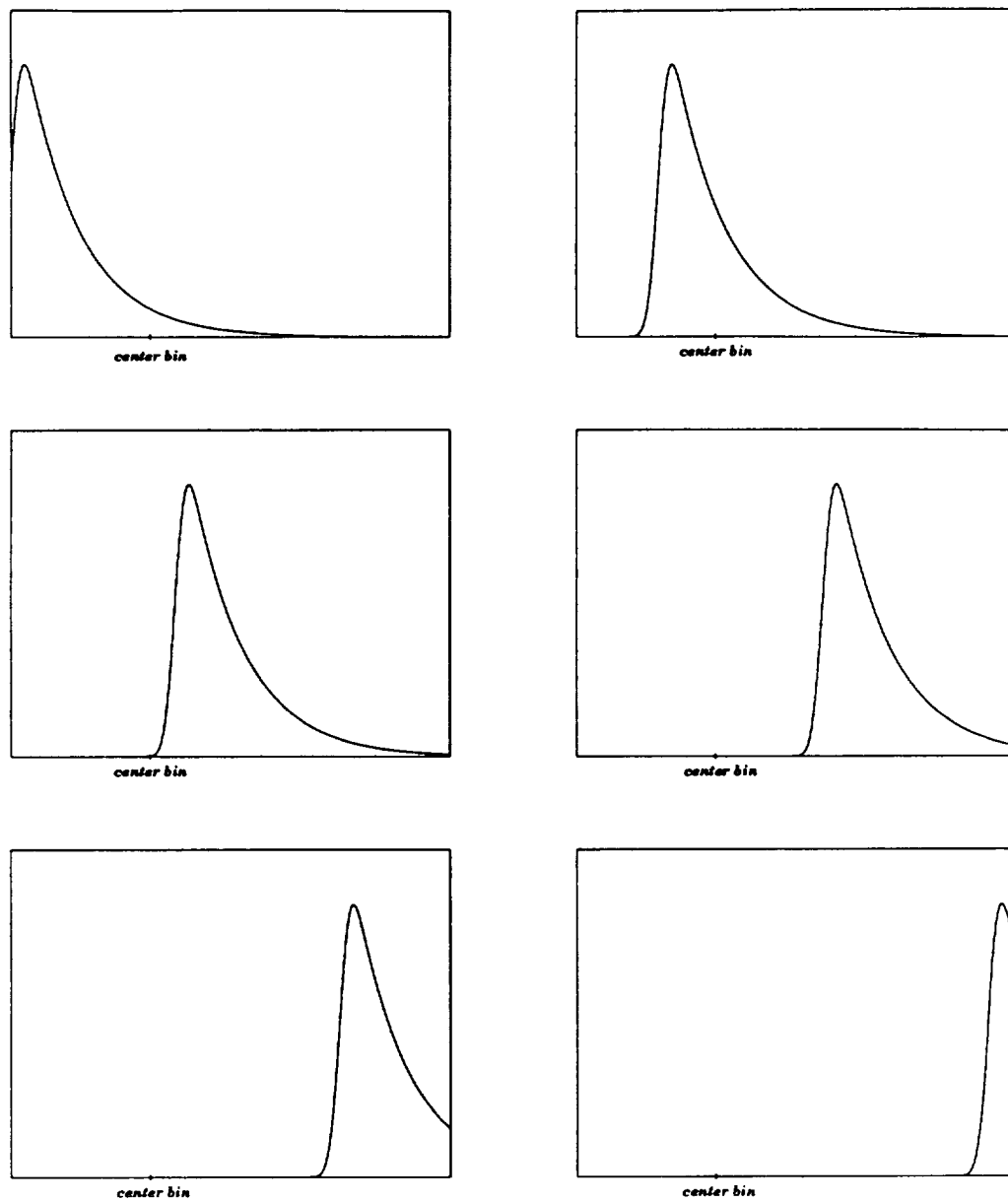


Figure 3.10. A series of waveforms illustrating the acquisition procedure of the AAFE altimeter radar system.

When the radar is operating at a PRF of 750 Hz and averaging 64 waveforms, each averaged waveform is spaced $\frac{1}{750} \times 64$ or .085 seconds apart. If the user enters 800 as the maximum range and 350 as the minimum range, the resulting acquisition time with a step size of 10 meters is 3.8 seconds. If it is necessary to reduce this time, the step size can be easily changed to 20 meters. Doing this would reduce the acquisition time in this example to 1.9 seconds.

This method of acquisition is simple, but there are more efficient ways to acquire lock. For example, the search for the surface could start at the half way point between the maximum and minimum range and look to either side of this range until a small enough value of ΔR is achieved. Rather than searching through the entire set of ranges, this method would stop as soon as lock is acquired.

3.1.6 Control Subsystem

The control subsystem is responsible for setting the state of all RF switches in the transmitter and receiver, for controlling the timing of the chirp and de-chirp pulses and for controlling the state of the AGC in the receiver. As figure 3.14 shows, it consists of two sections, a Stanford Research Systems (SRS) Digital Pulse Generator and a control box containing five wire-wrapped electronic boards. The settings of the SRS Pulse Generator are controlled from the computer over a GPIB IEEE 488 bus. The chirp generator pulse is a 50 nsec pulse produced by the SRS Generator at the chosen pulse repetition frequency, and a signal from the tracking subsystem tells the Generator when to create the de-chirp generator pulse. These two pulses go to the control box where they trigger the signals for all the switches in the transmitter and receiver, the signals for the spectrum generator in the transmitter and the trigger pulse for the data acquisition subsystem. GPIO signals from the HP computer control the state and duration of all pulses leaving the control box and they also control the latches in the control box, which are used to make adjustments

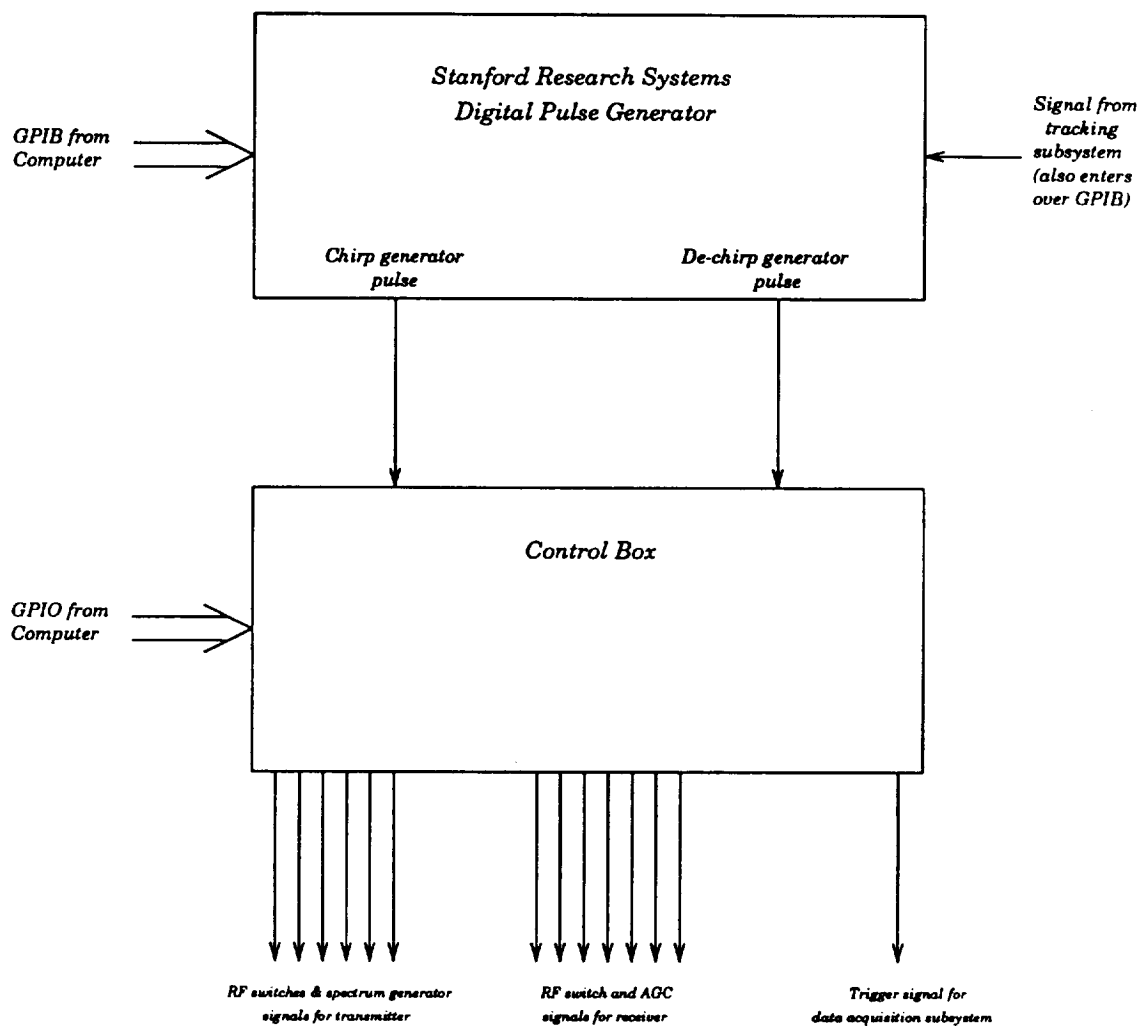


Figure 3.11. Simplified block diagram of the AAFE altimeter control subsystem.

to the AGC in the receiver. A more detailed explanation of the SRS Digital Pulse Generator can be found in the Model DG535 Manual [Stanford, 1987] and the wiring diagrams for the control box are in the Refurbished AAFE Altimeter Manual.

3.2 System Calibration

3.2.1 Internal Calibration

In order to achieve as accurate altitude measurements as possible, all internal delays in the AAFE radar altimeter system must be calibrated. As shown in figure 3.15, there are three places where delays occur: the radar hardware (transmitter and receiver), the waveguide run and the horn antenna. Once these delays have been determined, the reference plane for the altitude measurements is the aperture of the horn antenna.

To measure the internal hardware delays of the system, the AAFE altimeter is put in the calibration mode. In this mode, the RF switches are set so that the chirp does not go to the antenna, but instead passes through couplers and attenuators that knock the signal down 80 dB before it goes to the receiver. Figure 3.16 is a simplified block diagram showing the path taken by the calibration chirp and de-chirp pulse in the transmitter and receiver. The system is designed so that the path taken by the calibration chirp is identical in electrical length to that taken by the de-chirp. Therefore, when the radar is in the calibration mode, a chirp and de-chirp created by the same initial impulse to the RAC device will be aligned perfectly when mixed. The result is an impulse at zero meters as shown by the actual AAFE internal calibration waveform in figure 3.17.

For internal calibration, however, it is necessary to know the additional distance travelled by the chirp all the way to the circulator and back when the system is in the transmit mode. This is done by placing a "short" on the port of the circulator that normally goes to the waveguide run and antenna. In the calibration mode, the

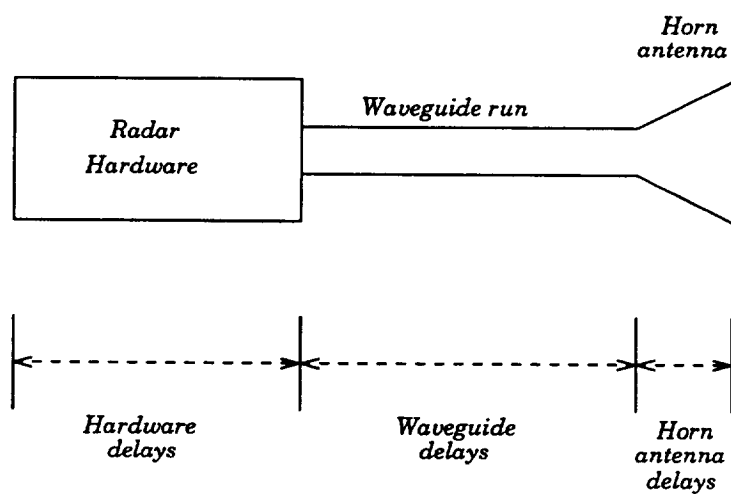


Figure 3.12. Internal delays in the AAFE radar altimeter system.

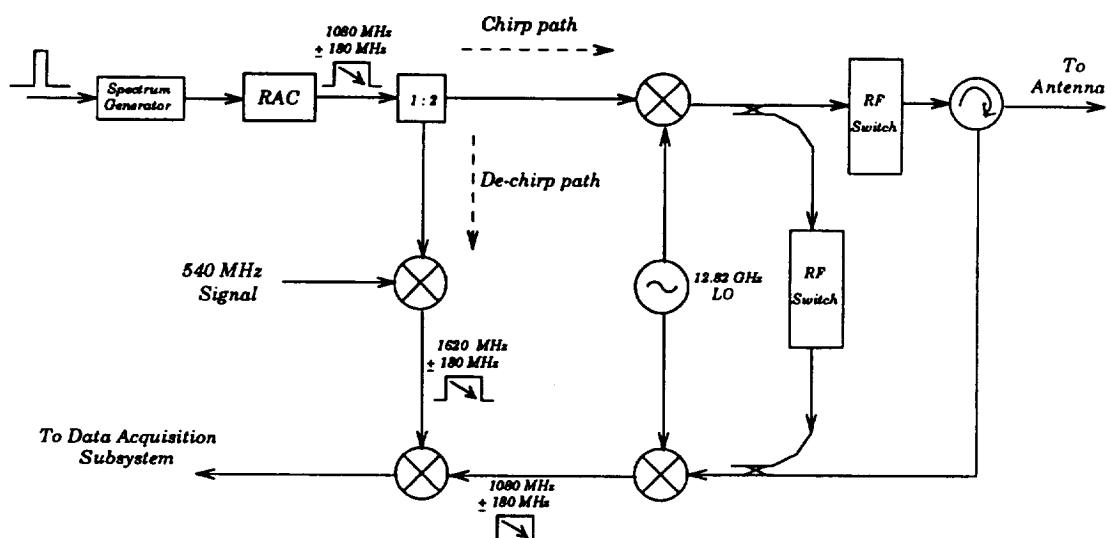


Figure 3.13. Simplified block diagram of the AAFE transmitter and receiver, showing the path taken by the chirp and de-chirp pulse when the system is in the calibration mode.

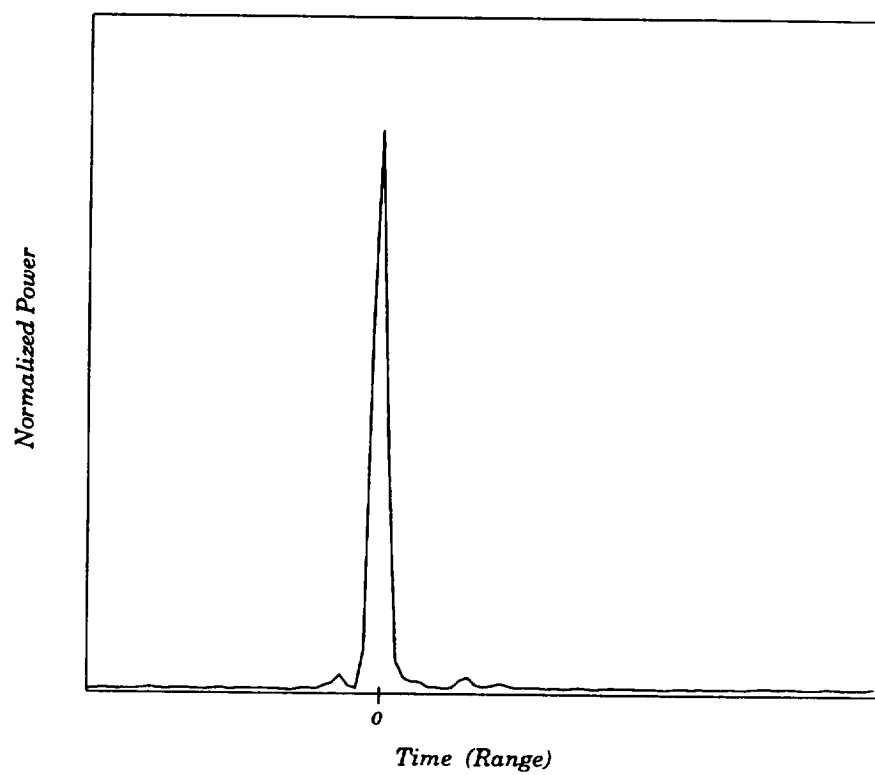


Figure 3.14. Actual internal calibration impulse of the AAFE radar altimeter.

RF switch before the circulator is open or not connected. Some power leaks through this switch, which has 70 dB of isolation, reflects off the "short" and goes into the receiver. The result, as figure 3.18a illustrates, is an impulse located at a delay of $t_{hardware}$, which is equivalent to the internal delays of the radar system.

In a similar manner the waveguide run, which starts at the circulator, passes through the floor of the aircraft and connects to the antenna, is calibrated. A "short" is placed at the end of the waveguide run (before the antenna) and the radar is put in the calibration mode. Leakage through the RF switch passes through the circulator, down the waveguide, reflects off the "short" and returns to the receiver. The result is an impulse located at a time equivalent to the sum of the internal hardware delays and the waveguide delays as shown in figure 3.18b. As a separate check, the delay of the section of waveguide, $t_{waveguide}$, is measured using a Hewlett Packard Network Analyzer.

The AAFE horn antenna has a .092 m x .066 m aperture and is .55 meters long. The resulting maximum phase error across the aperture is less than 3 mm. Since the phase error is negligible, a "short" is placed across the aperture and a measurement made using the radar in the same way as for the waveguide and hardware delays. This measurement represents the total internal delay of the AAFE radar system or

$$t_{system} = t_{hardware} + t_{waveguide} + t_{antenna}. \quad (3.6)$$

Again, a HP Network Analyzer is used to make a measurement of $t_{antenna}$. The result is compared to the $t_{antenna}$ that is calculated by subtracting $t_{hardware}$ and $t_{waveguide}$ from the t_{system} measurement.

Once the value of t_{system} is well quantified, it is removed from the stored value of the delay between the chirp and de-chirp pulse, and the resulting reference plane for the altitude measurements of the radar is the aperture of the horn antenna. It is necessary to make both the "short" and the network analyzer measurements to

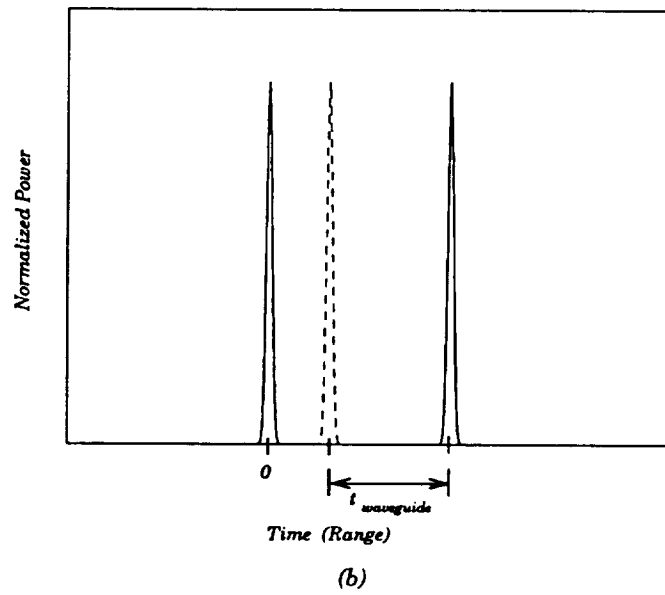
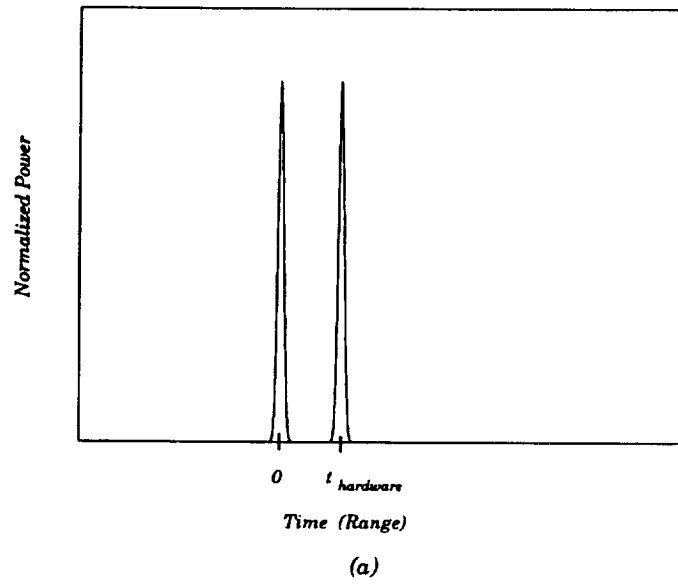


Figure 3.15. Example of measurement of (a) t_{hardware} and (b) $t_{\text{waveguide}}$ for internal calibration.

check for inconsistencies that could be caused by problems, such as a break in the waveguide run or a poor connection to the antenna.

3.2.2 External Calibration

For the external calibration, the distance to the surface below the aircraft is measured with the radar when the aircraft is on the ground, as shown in figure 3.19. A separate independent measurement must be made with a tape measure. When the radar is in the transmit mode, however, the surface must be at least a pulse width or 450 meters away. Even by cutting the pulse width down to 278 meters, the distance is too far to measure by tape measure. As a result, the radar must be in the calibration mode, as described in the internal calibration section. If a reflective surface is placed on the ground, such as a sheet of metal, there is enough leakage through the calibration RF switch for the pulse to travel out the antenna and reflect off the surface below. The resulting radar measurement is compared to the tape measurement and used to quantify the accuracy of the altimeter.

3.3 Noise Analysis

3.3.1 System Signal-To-Noise Ratio

Since added noise changes the shape of the AAFE return waveform and therefore affects the resulting range measurement, as shown in Figure 3.20, the resolution of the radar is fundamentally limited by its system noise level. To quantify the resolution of the instrument, the amount of noise power for a given input signal, or the system signal-to-noise ratio must be determined. This is done by modelling the noisy receiver, depicted in figure 3.21a, as a noiseless receiver with noise added to the input signal, and then using linearity to separate the system into two noiseless receivers, as shown in figures 3.21b and 3.21c respectively.

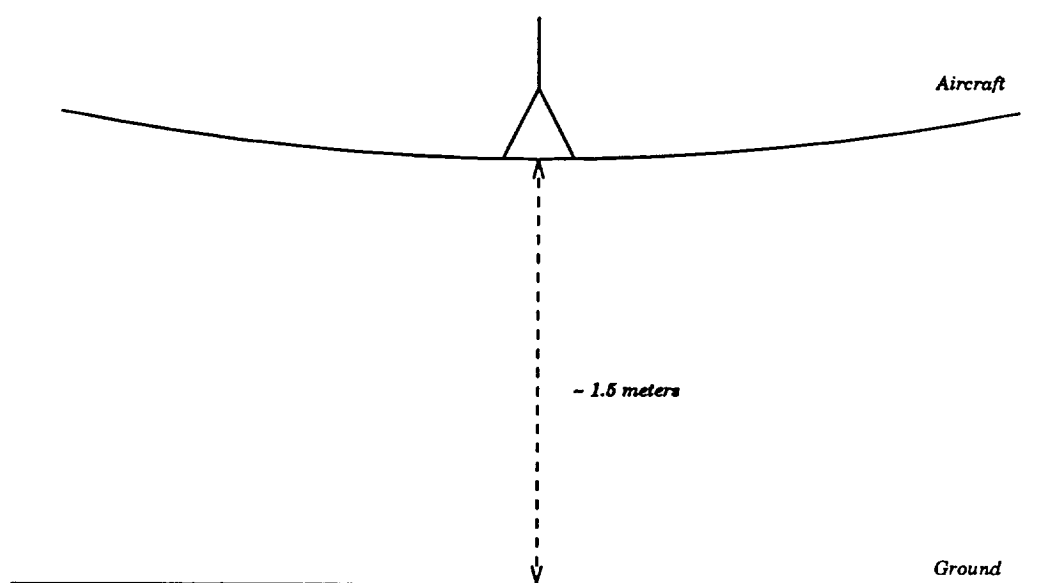


Figure 3.16. Example of external calibration to surface below aircraft, when the aircraft is on the ground.

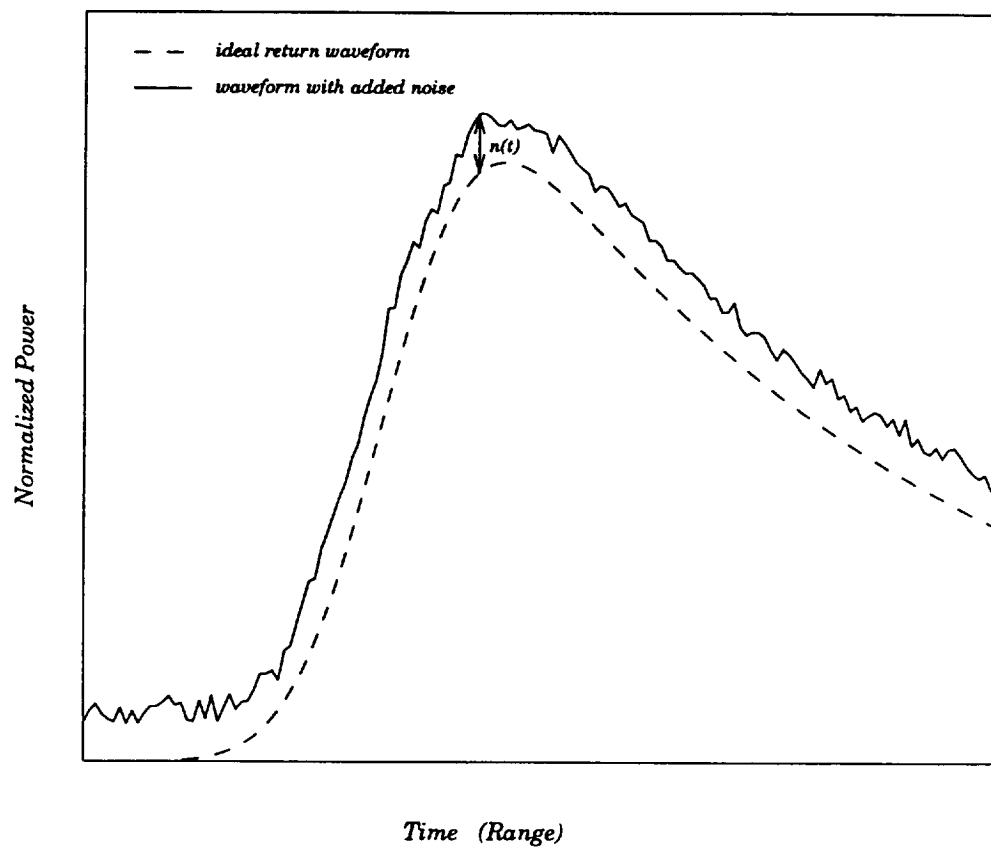
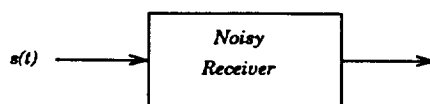
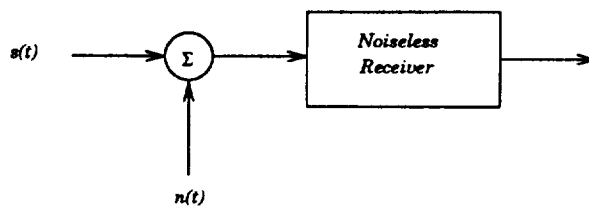


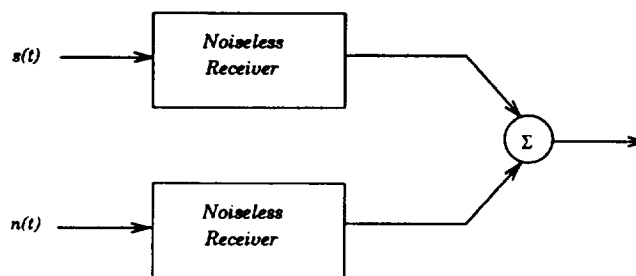
Figure 3.17. Example of how added noise affects the shape of the AAFE altimeter return waveform.



(a)



(b)



(c)

Figure 3.18. Method used to model a noisy radar receiver. (a) Signal entering noisy receiver; (b) equivalent system with noiseless receiver and noise added to input signal; (c) equivalent system using linearity to model the system as two separate noiseless receivers.

Assuming the radar return entering the receiver is from a single point scatterer, the chirp signal is represented as

$$s(t) = A \cos(2\pi f_o t + 2\pi a t^2) \text{rect}\left(\frac{t}{T}\right) \quad (3.7)$$

where $f_o = 13.9$ GHz, a is the slope of the chirp or $\frac{1}{2}\left(\frac{360 \text{ MHz}}{3 \mu\text{sec}}\right)$, T is the actual transmitted pulse width and

$$\text{rect}\left(\frac{t}{T}\right) = \begin{cases} 1 & |t| < \frac{T}{2} \\ 0 & \text{otherwise} \end{cases} \quad (3.8)$$

As the simplified receiver block diagram in figure 3.22 shows, the AAFE return signal is mixed down in frequency and filtered in three different stages. The resulting signals $x_0(t)$, $x_1(t)$ and $x_2(t)$ are

$$x_0(t) = \frac{A}{2} \cos(2\pi(f_o - f_{LO1})t + 2\pi a t^2) \text{rect}\left(\frac{t}{T}\right) \quad (3.9)$$

$$x_1(t) = \frac{A}{4} \cos(2\pi(f_{de\text{-}chirp} - f_o + f_{LO1})t) \text{rect}\left(\frac{t}{T}\right) \quad (3.10)$$

$$x_2(t) = \frac{A}{8} \cos(2\pi f_3 t) \text{rect}\left(\frac{t}{T}\right), \quad (3.11)$$

where $f_{LO1} = 12.82$ GHz, $f_{de\text{-}chirp} = 1620$ MHz, $f_{LO2} = 567$ MHz and $f_3 = f_{LO2} - f_{de\text{-}chirp} + f_o - f_{LO1} = 27$ MHz. After the signal is sampled over the $3 \mu\text{sec}$ pulse, Fourier transformed to

$$Y(f) = \frac{A}{16} [\text{sinc}(T(f - f_3)) + \text{sinc}(T(f + f_3))] \quad (3.12)$$

and then converted to power, the resulting frequency domain signal, $|Y(f)|^2$, as figure 3.23 illustrates, has a power level, P_{signal} , equal to $\frac{A^2}{256}$.

When analyzing the affect of noise power in the system, the two main sources to consider are 1) thermal noise due to the random motion of electrons in a conductor, and 2) receiver noise generated from electronic devices within the receiver [Skolnik, 1980]. Both types of noise have Gaussian statistics and can be modelled as a wide-sense stationary random process, $n(t)$, with zero mean and an autocorrelation

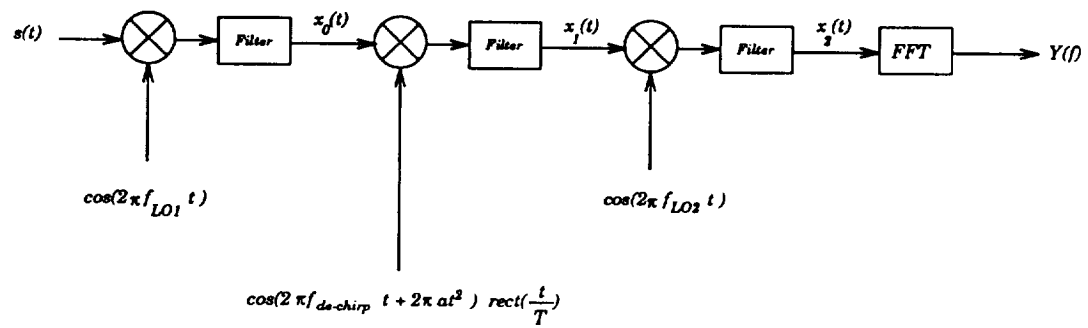


Figure 3.19. Simplified block diagram of the receiver showing the location of each signal in equations 3.9, 3.10 and 3.11.

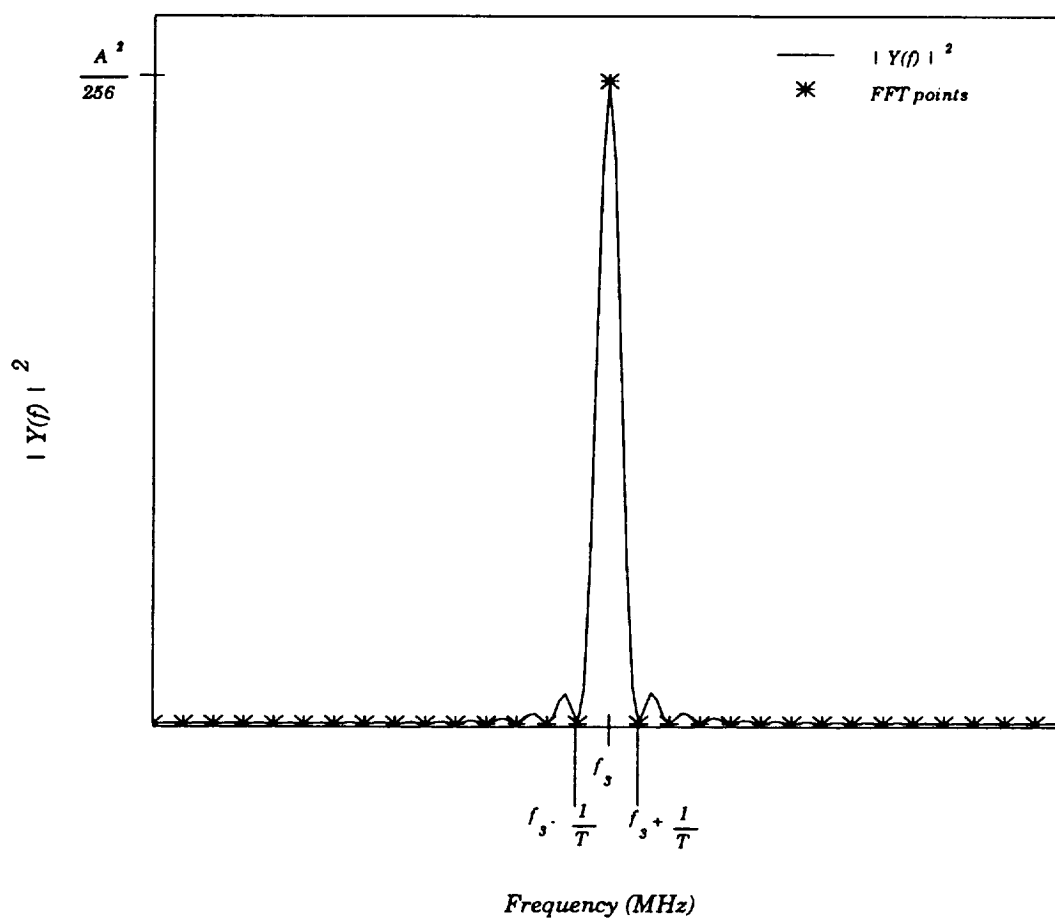


Figure 3.20. Final output of receiver when the input is a return from a single point scatterer.

function, $R_n(\tau) = \frac{N_o}{2}\delta(\tau)$. This idealized form of noise called white noise has a power spectral density, $W_n(f) = \frac{N_o}{2}$, that is independent of frequency. The value of N_o is the variance of $n(t)$ or the noise power at the input stage of the receiver. For a radar system, this is

$$N_o = kT_{rec}, \quad (3.13)$$

where k is Boltzmann's constant and T_{rec} is the equivalent noise temperature of the receiver [Haykin, 1983]. Since this system is modelled as a noiseless receiver the noise figure, F_n , must also be incorporated into the input noise, resulting in $N_o = kT_{rec}F_n$. When this random process is passed through the three stages of the AAFE receiver shown in figure 3.22, the resulting autocorrelation function prior to the FFT stage is

$$R_w(\tau) = \frac{N_o}{64} B_{rec} \text{sinc}(B_{rec}\tau) \quad (3.14)$$

where B_{rec} , the bandwidth of the final receiver filter, is 70 MHz. After being digitized over a 3 μsec period, each resulting noise sample has a Gaussian distribution with zero mean and a variance of $\frac{N_o B_{rec}}{64}$. Since the total average power is equivalent to $R_w(0)$, the final noise power or the variance of the random process is

$$P_{noise} = \frac{N_o B_{rec}}{64} = \frac{kT_{rec}F_n B_{rec}}{64}. \quad (3.15)$$

Using the calculated signal and noise power levels, the resulting AAFE system signal-to-noise ratio is

$$\frac{S}{N} = \frac{P_{signal}}{P_{noise}} = \frac{A^2}{256} \frac{64}{kT_{rec}F_n B_{rec}} = \frac{A^2}{4kT_{rec}F_n B_{rec}}. \quad (3.16)$$

The value of the variable A is determined by calculating the average power level in the received signal and relating this to the radar range equation. By definition, the average power in a signal, $s(t)$, that has a period of T_o is

$$P_{av} = \frac{1}{T_o} \int_{-\frac{T_o}{2}}^{\frac{T_o}{2}} |s(t)|^2 dt, \quad (3.17)$$

[Haykin, 1983] and for the signal defined in equation 3.7, P_{av} is equal to $\frac{A^2 T}{4T_o}$ where T is the actual transmitted pulse width. The average power received by the radar

is also related to the transmitted power, P_t , the antenna gain, G , the wavelength of the transmitted signal, λ , the backscatter coefficient, σ^o , the area of the footprint, A_f , and the range to the surface, R , by

$$P_{av} = \frac{P_t G^2 \lambda^2 \sigma^o A_f T}{(4\pi)^3 R^4 T_o} \quad (3.18)$$

[Skolnik, 1980]. As calculated in chapter 2, the area of the pulse-limited footprint of the altimeter is

$$A_f = \pi R c \tau \quad (3.19)$$

where τ , the effective pulse width, is the inverse of the transmitted bandwidth, and the transmitted power is the peak power multiplied by the compression ratio, BT . The resulting received power for a pulse compression radar is

$$P_{av} = \frac{G^2 \lambda^2 \sigma^o T}{64\pi^3 R^4 T_o} \frac{\pi R c}{B} P_{peak} B T = \frac{P_{peak} G^2 \lambda^2 \sigma^o c T^2}{64\pi^2 R^3 T_o}. \quad (3.20)$$

By equating this to $\frac{A^2 T}{4T_o}$ and substituting the result into equation 3.16, the system signal-to-noise ratio becomes

$$\frac{S}{N} = \frac{P_{peak} G^2 \lambda^2 \sigma^o c T}{64\pi^2 R^3 k T_{rec} B_{rec} F_n}. \quad (3.21)$$

When the altimeter is flown at altitudes below 450 meters (3 μ secs), however, the transmitted pulse width, T , must be cut to prevent receiving and transmitting at the same time. The resulting T is approximately proportional to altitude or

$$T = \frac{2R}{c} \quad \text{for } R < 450 \text{ meters.} \quad (3.22)$$

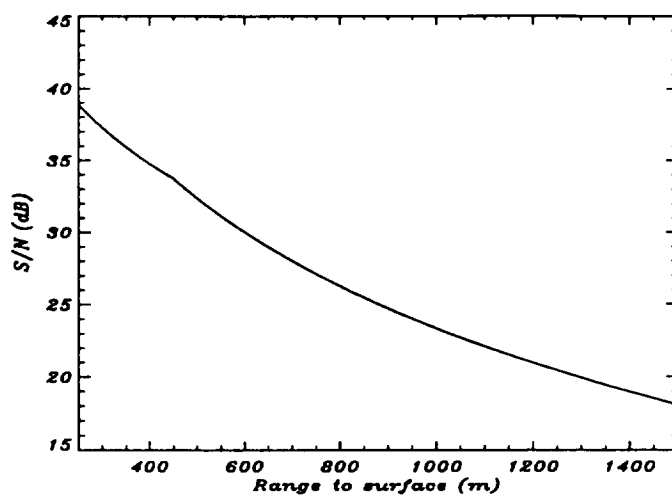
So, the signal-to-noise ratio of the radar altimeter for all ranges is

$$\frac{S}{N} = \begin{cases} \frac{P_{peak} G^2 \lambda^2 \sigma^o c T}{64\pi^2 R^3 k T_{rec} B_{rec} F_n} & \text{for } R > 450 \text{ meters} \\ \frac{P_{peak} G^2 \lambda^2 \sigma^o}{32\pi^2 R^2 k T_{rec} B_{rec} F_n} & \text{for } R < 450 \text{ meters} \end{cases}$$

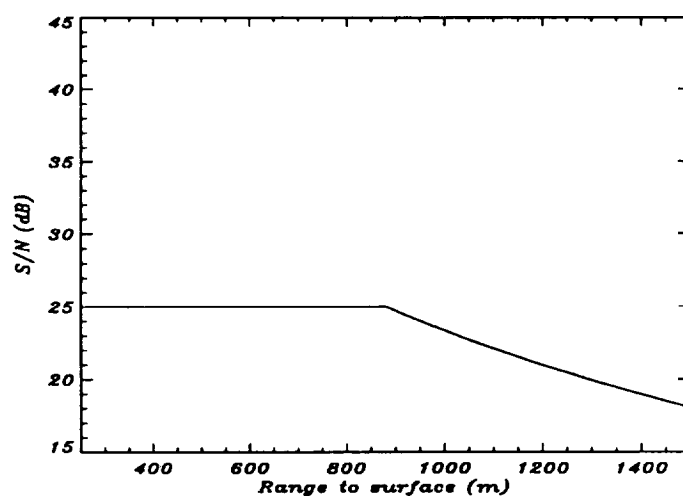
Table 3.1 is a listing of the AAFE altimeter system parameters necessary to compute $\frac{S}{N}$ and figure 3.24a is a plot of the resulting $\frac{S}{N}$ versus altitude using an average value

Table 3.1. Table of AAFE parameters used to calculate the system signal-to-noise ratio.

PARAMETER	VALUE
P_{peak}	.1 Watts
G	21 dB = 144.54
λ	2.16 cm
c	3×10^8 m/sec
k	1.38×10^{-23} J/deg
T_{rec}	310.5 K
B_{rec}	70 MHz
F_n	13.3 dB = 21.38



(a)



(b)

Figure 3.21. Signal-to-noise ratio of the AAFE altimeter versus aircraft altitude using a σ^o of 3 dB. (a) Theoretical $\frac{S}{N}$ for the altimeter and (b) actual $\frac{S}{N}$ due to the limited dynamic range of the receiver.

of 3 dB for σ^0 [Swift et al., 1985]. The dynamic range of the AAFE receiver, however, is limited to 25 dB and therefore, as shown in figure 3.24b, the actual signal-to-noise ratio of the instrument cannot exceed this level.

3.3.2 Range Resolution

Once the signal-to-noise ratio of the radar altimeter is known, the resolution of the system can be calculated. As figure 3.25 shows, for a signal with a high signal-to-noise ratio, the slope of the ideal pulse is approximately the same as the slope of the noisy pulse, or

$$\frac{A}{t_r} = \frac{n(t)}{\Delta t} \quad (3.23)$$

where A and t_r are the amplitude and rise time of the ideal pulse, $n(t)$ is the added noise and Δt is the resulting error in time. Taking the expected value of the square of Δt shows that the error in time is related to $\frac{S}{N}$ as

$$\sqrt{\langle \Delta t^2 \rangle} = \frac{t_r}{\sqrt{\frac{A^2}{\langle n(t)^2 \rangle}}} = \frac{t_r}{\sqrt{\frac{S}{N}}} \quad (3.24)$$

Therefore, the final range resolution of the radar becomes

$$\Delta R = \frac{t_r c}{2\sqrt{\frac{S}{N}}} \quad (3.25)$$

[Skolnik, 1980]. The rise time of the pulse, t_r , is dependent on the bandwidth, B , and the surface roughness, σ_h , or $t_r \approx \frac{1}{B} + \frac{2\sigma_h}{c}$. Figure 3.26a shows a plot of the resulting AAFE range resolution using the system signal-to-noise ratio in figure 3.24b and a typical rise time for glacial ice returns of 5 range bins or 13.88 nsecs. Returns from a rougher surface would have a larger rise time and therefore a higher range resolution. Similarly, returns from a smoother surface would have a shorter rise time and a better range resolution. The extent of the range resolution for most realizable surfaces is shown by the shaded area in figure 3.26b.

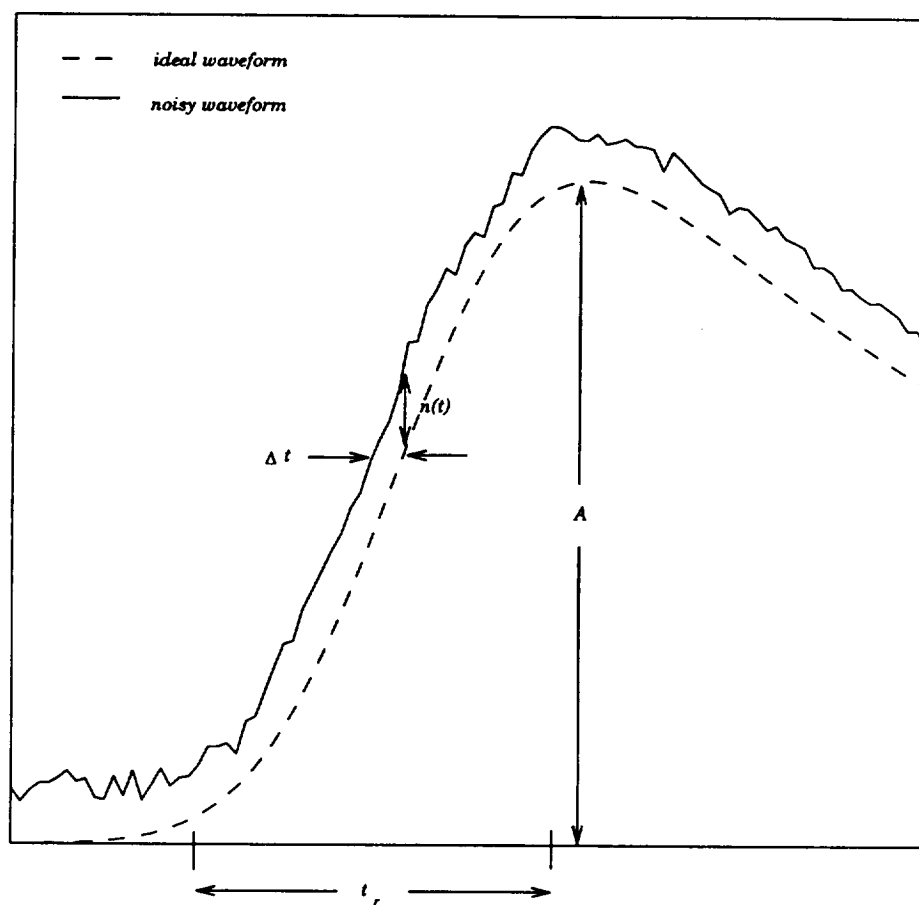
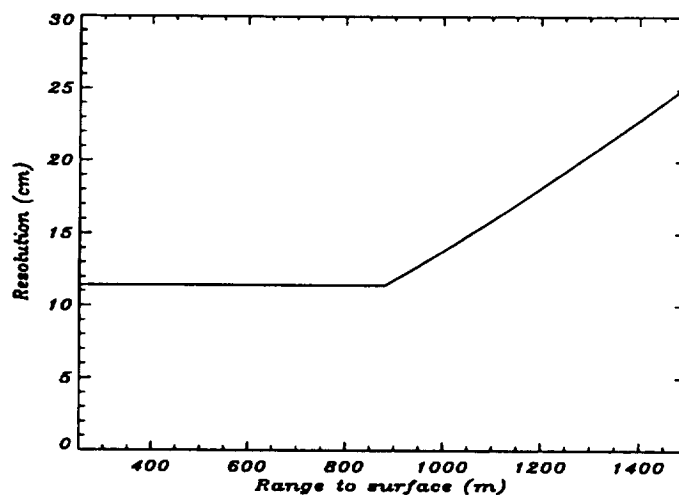
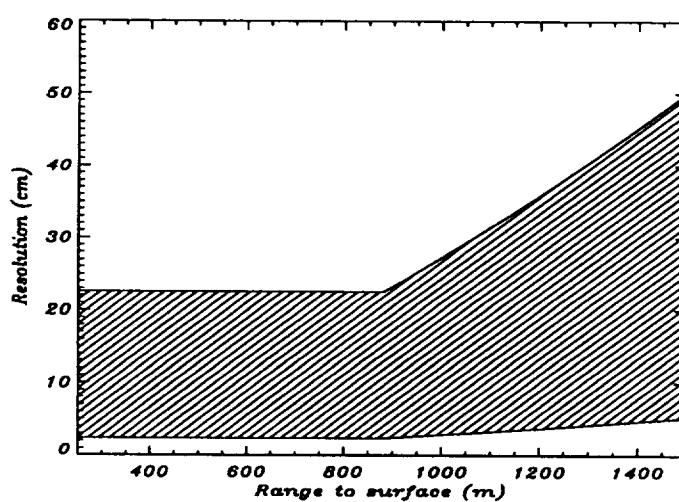


Figure 3.22. Calculation of time error, Δt , using the leading edge of the ideal and noisy pulse.



(a)



(b)

Figure 3.23. Range resolution of the AAFE radar altimeter versus altitude (a) using an approximate leading edge rise time of 13.88 nsecs and (b) using the maximum and minimum realizable values of surface roughness to calculate the leading edge rise time.

3.3.3 Quantization Noise

The signal-to-noise ratio of the radar altimeter is degraded by quantizer noise that is added when the signal is sampled by the digitizer. The effects on the $\frac{S}{N}$ are calculated by performing the same analysis as in section 3.1, but including the error induced by sampling. This yields

$$\frac{S}{N} = \frac{P_{peak} G^2 \lambda^2 \sigma^o c T}{64 \pi^2 R^3 (k T_{rec} B_{rec} F_n + \frac{\sigma_e^2}{G_{rec}})}, \quad (3.26)$$

where σ_e^2 is the variance of the uniformly distributed quantization noise and G_{rec} is the gain of the receiver. However, since the digitizer is preceded by an automatic gain control (AGC) circuit, the gain of the receiver is not a constant. Using a typical gain of 60 dB and the 12 bit digitizer variance of 7.95×10^{-8} , the resulting effect on the signal-to-noise ratio is a reduction of .95 dB. Therefore, the average degradation in range resolution due to quantization noise is .11 cm.

3.3.4 FFT Errors

Additional errors are added to the AAFE return waveform when the Papoulis window and FFT are taken in the data acquisition subsystem. As the radar pulse intersects with the surface, it reflects back at all ranges from nadir to the edge of the beam-limited footprint. When delays in range are converted to shifts in frequency, the resulting return waveform is continuous in the frequency domain, as illustrated by figure 3.11. After the waveform is sampled and transformed, however, it consists of discrete spectral points or bins. This picket fence effect [Harris, 1978] results in a loss of the spectral information between each bin. Fortunately, this information can be retrieved by fitting the discrete points to a continuous model function.

Since the Fast Fourier Transform is over a finite time interval, each single frequency in the input waveform is actually a squared-sinc function in the spectral domain. If an input frequency coincides with the FFT point spacing the result, as

figure 3.23 shows, is a single impulse at the proper frequency and no effect from the sidelobes at other points. Input frequencies that do not line up with the FFT spacing, however, have non-zero sidelobe projections on the FFT points, resulting in spectral leakage from one frequency tone into other parts of the spectrum [Harris, 1978]. Because the AAFE waveform is continuous, it has many frequencies that do not coincide with the FFT spacing and therefore spectral leakage does occur. By windowing the return waveform, the effects of this leakage are reduced and the maximum resulting sidelobe due to a single frequency is -18 dB [Papoulis, 1973].

When the window is applied, each sampled time-domain point is weighted or tapered and some information is lost at the edges of the return pulse. The resulting frequency domain signal, $Y_w(f)$, is a convolution of the actual signal, $Y(f)$, with the transform of the weighting function, $W(f)$, or

$$Y_w(f) = Y(f) * W(f). \quad (3.27)$$

The mean-squared error induced on the final waveform can be approximated using

$$\epsilon^2 = \int |Y_w(f) - Y(f)|^2 df \quad (3.28)$$

[Oppenheim and Schafer, 1989] and converting $Y_w(f)$ and $Y(f)$ to their discrete representations, resulting in

$$\epsilon^2 = \sum_k |Y_w[k] - Y[k]|^2. \quad (3.29)$$

Although this error is difficult to quantify for an AAFE return from a rough surface, it can be calculated for some simple waveforms. The return from a single point scatterer, for example, has a mean-squared error due to weighting of approximately .1 or -10 dB over the entire range window.

CHAPTER 4

ALTIMETRY MEASUREMENTS OF THE GREENLAND ICE SHEET

4.1 1991 Greenland Experiment

4.1.1 Experiment Description and Flight Lines

In 1991, NASA conducted a multisensor airborne altimetry experiment over the Greenland ice sheet. This experiment was the first in a series of biennial experiments aimed at measuring small-scale changes in the topography and mass balance of the ice sheet, and at understanding the effects of penetration of a Ku-band radar altimeter pulse into the ice sheet. The NASA Advanced Application Flight Experiment (AAFE) Ku-band radar altimeter, refurbished by the Microwave Remote Sensing Laboratory at the University of Massachusetts in 1990-1991, participated in this experiment along with the NASA Airborne Oceanographic Lidar (AOL), the NASA Airborne Terrain Laser Altimeter System (ATLAS) and the NASA Ka-band Surface Contour Radar (SCR). The experiment consisted of ten flights over the Greenland ice mass between August 22, 1991 and September 20, 1991 aboard the NASA P-3 aircraft. Positional information provided by three Global Positioning System (GPS) receivers aboard the NASA P-3 was used to control the autopilot of the aircraft. This system allowed accurate positioning under the European Remote Sensing satellite (ERS-1) trajectory and enabled accurate repeat missions on all flight lines. The missions were flown from Sondrestrom Air Force Base (now known as Kangerlussuaq) on the west coast of Greenland over the ice sheet at an average altitude of 400 meters above the surface.

All of the remote sensing radar and laser instruments provided information about the aircraft altitude above the ice sheet. The GPS receivers, on the other hand, calculated the aircraft altitude above the ellipsoid, which is a reference sphere around the surface of the earth. The difference between these two measurements, as shown in figure 4.1, is the actual ice sheet altitude above the ellipsoid.

The ten flight lines covered an area between 65° N and 75° N and were mainly concentrated on the western half of the Greenland ice sheet. Since there were technical problems with the GPS instruments for the first three flights, only data from the last seven flights is presented. Figures 4.2 and 4.3 show the maps of these seven flight lines, which were created using processed GPS data files. To investigate the ability to repeat lines using the GPS autopilot system, the flight paths for the last three missions were approximately the same. The comparison between the aircraft position on September 18, 1991 and September 19, 1991 shown in figure 4.4 reveals that the autopilot kept the aircraft within an rms distance of 50 meters from its intended trajectory. This accuracy was achieved with post processing and by using differential GPS, a technique of placing additional GPS receivers at stationary locations to remove errors such as ionospheric effects. For this experiment, differential GPS receivers were placed in Sondrestrom, Jacobshavn and on the east coast near Angmagssalik. Figure 4.5 shows the location of these receivers as well as all the 1991 flight lines.

4.1.2 Runway Ground Truth Comparison

By comparing AAFE altitude results with independent ground truth measurements, the system biases and noise levels of the instrument have been determined. In the 1991 Greenland experiment, a ground survey was conducted on the Sondrestrom runway with a GPS receiver mounted on a truck. Since the truck could move slowly down the runway, each GPS three dimensional measurement was averaged

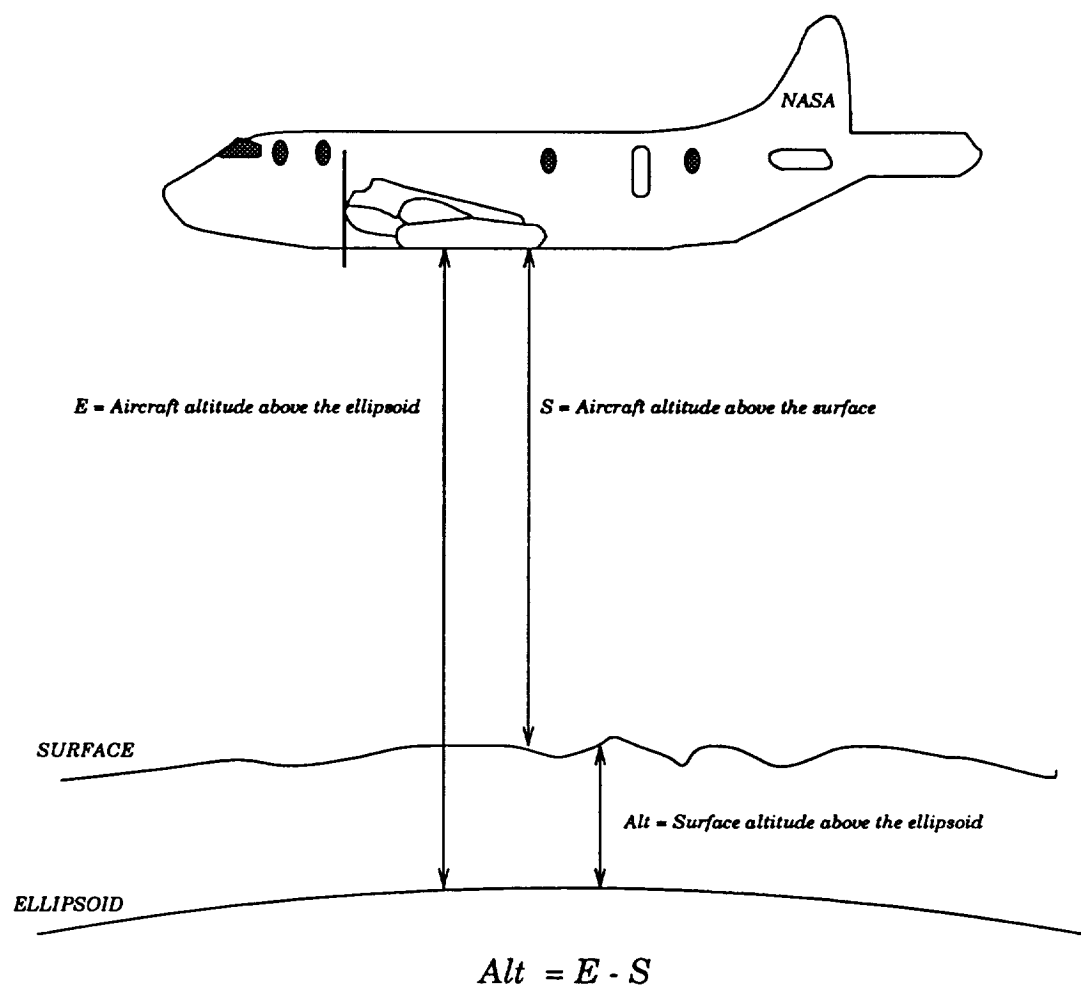


Figure 4.1. Illustration of the measurement of the ice sheet altitude above the ellipsoid.

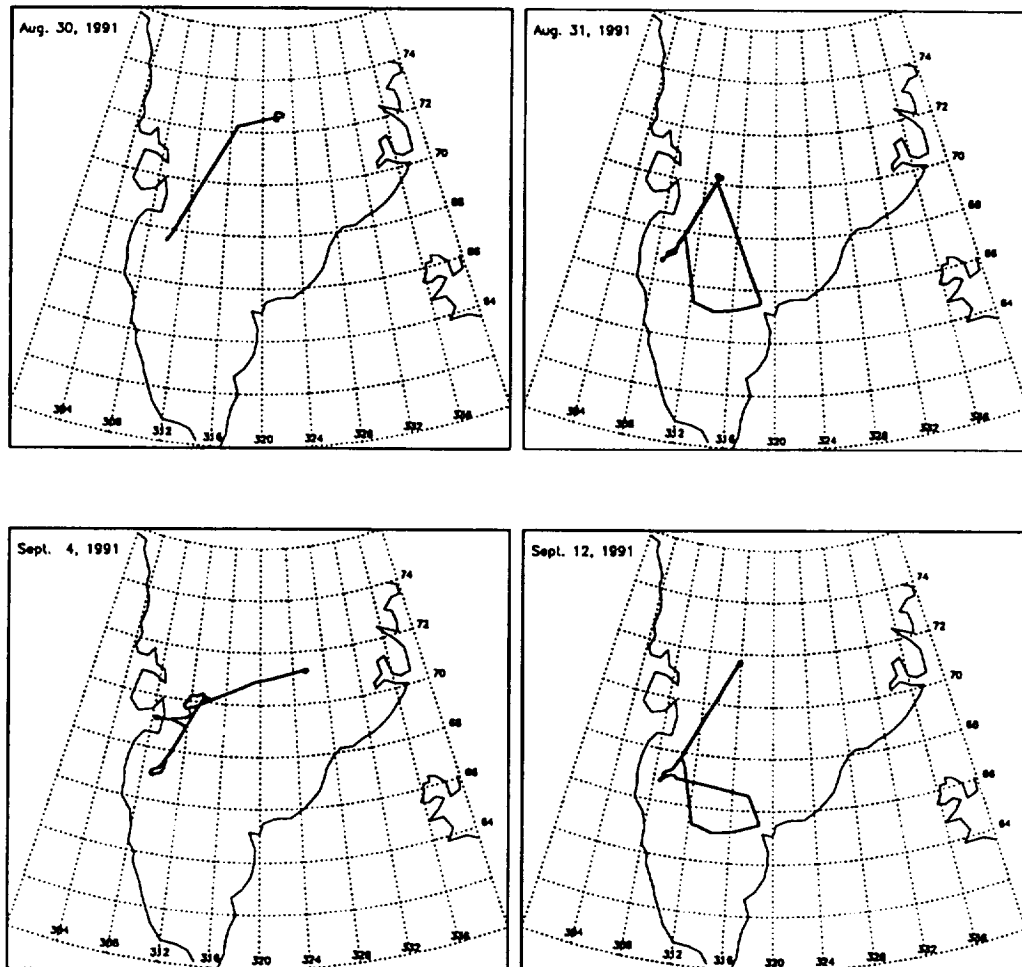


Figure 4.2. Four of the flight lines in the 1991 Greenland experiment.

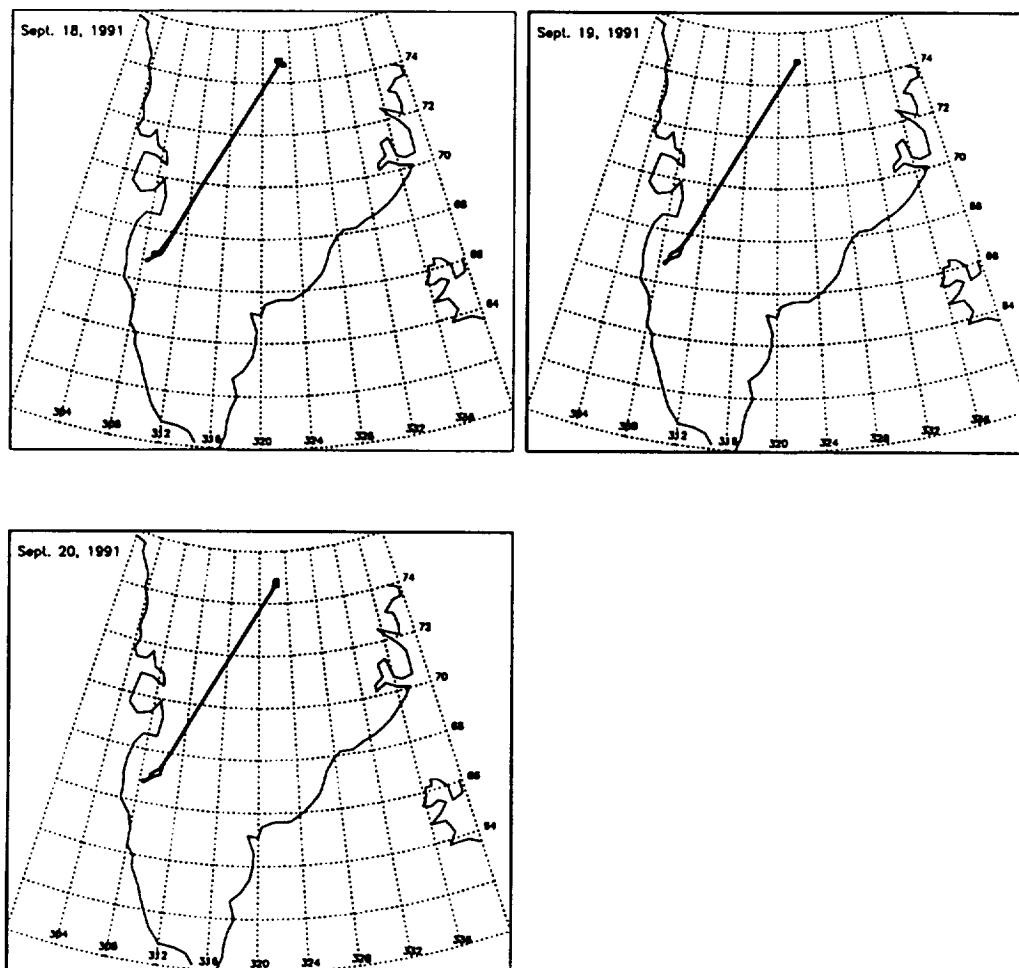


Figure 4.3. The final three flight lines in the 1991 Greenland experiment, which were all under the ERS-1 trajectory.

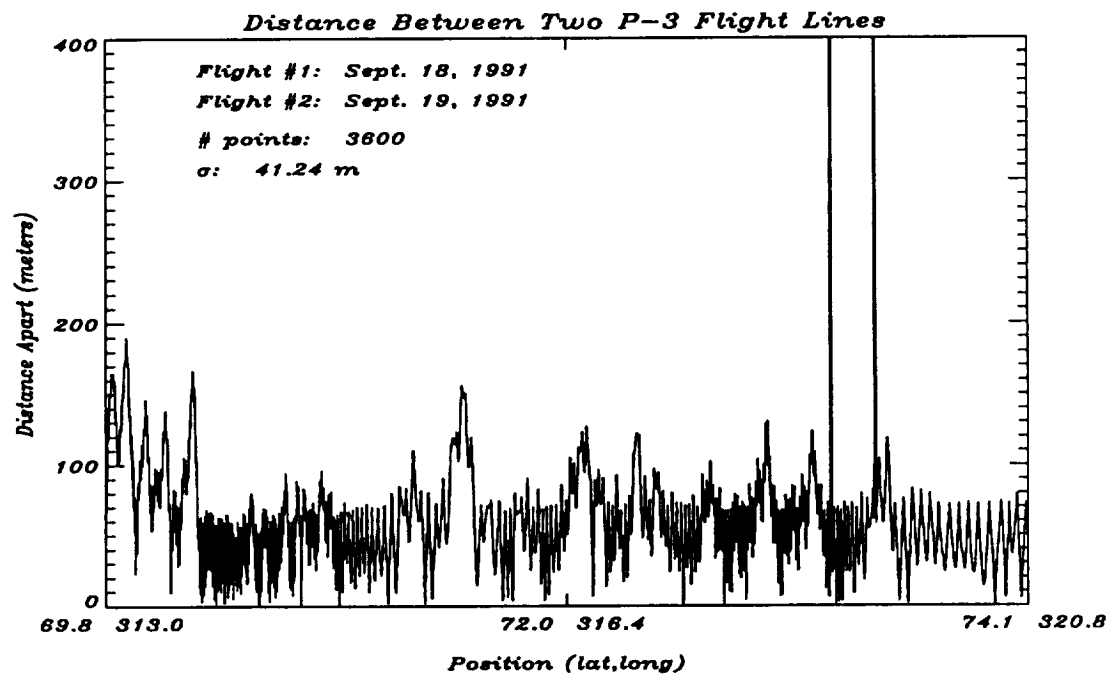


Figure 4.4. A comparison between the aircraft position on September 18, 1991 and September 19, 1991.

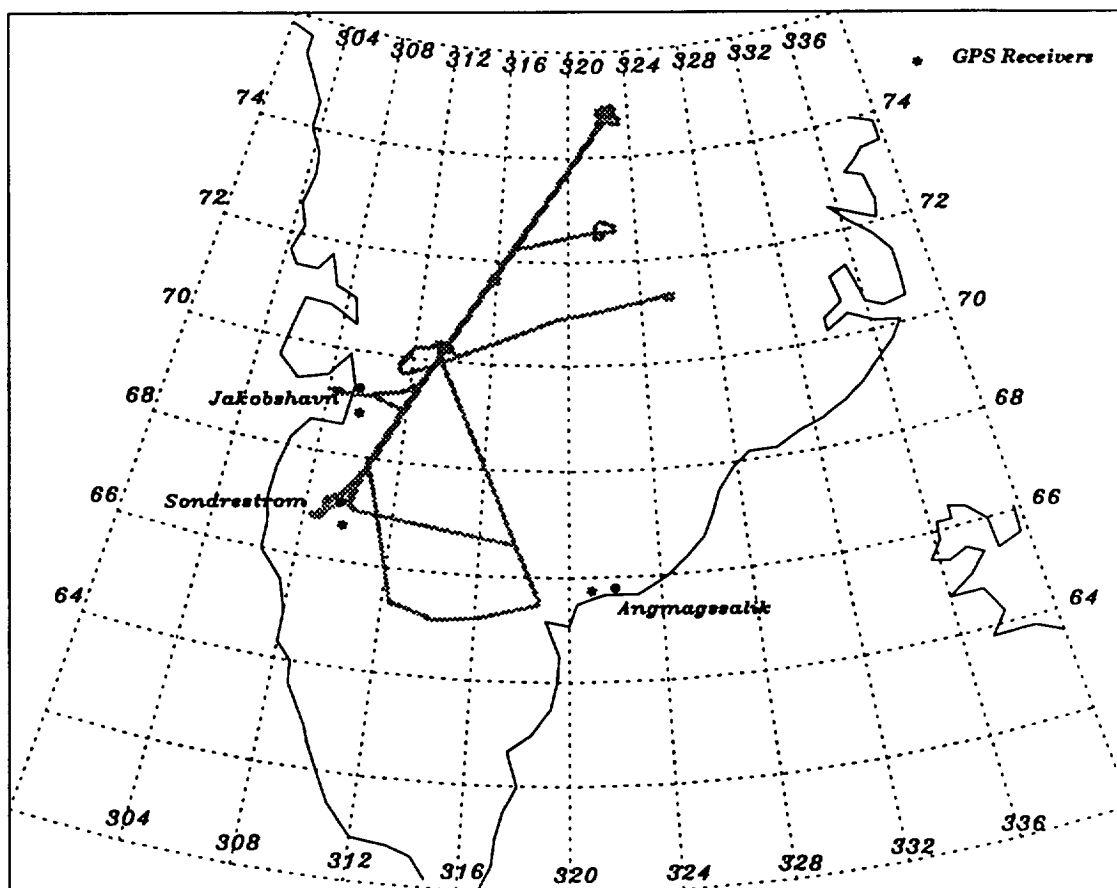


Figure 4.5. Location of differential GPS receivers and all of the 1991 flight lines.

for several seconds. Comparisons to traditional survey results and between data sets on different days, reveal that these runway ground truth data have a maximum bias of 1 cm and a maximum noise level of 3 cm.

Figure 4.6 shows a typical AAFE return waveform from the Sondrestrom runway. Because the runway is such a flat smooth surface, each runway waveform is retracked using a flat surface response model [Brown, 1977]. The asterisks in figure 4.6 represent the actual sampled data points while the dashed and solid lines represent the model and the resulting retracked altitude point, respectively. When the aircraft flew over the runway, the AAFE altimeter was able to take about one hundred and fifty altitude measurements spaced approximately ten meters apart. Since the GPS ground truth data set has many more samples, all the ground-based measurements that fall within a single pulse-limited footprint of the altimeter are averaged together before being compared to the retracked AAFE altitude. Figure 4.7a shows this using AAFE altimeter results from September 18, 1991 and ground-based GPS measurements from September 10, 1991. Since the two data sets agree so well, the best way to determine the system bias and noise level is to analyze the difference between them. The plot of the AAFE altitude minus the ground GPS altitude in figure 4.7b shows that the mean altitude difference is -8 cm and the noise level of the difference is 12 cm. Similar comparisons for runway passes on other flight days reveal that the mean difference remains between -6 and -8 cm and the noise level stays between 12 and 14 cm. From these results, the maximum range resolution of the AAFE altimeter altitude measurements for the 1991 Greenland experiment is determined to be 14 cm.

4.1.3 Comparison with the AOL Laser Altimeter

The NASA Airborne Oceanographic Lidar (AOL) is a 523 nm wavelength scanning laser altimeter. As its $.04^\circ$ beamwidth antenna rotates at 5 Hz it makes a conical

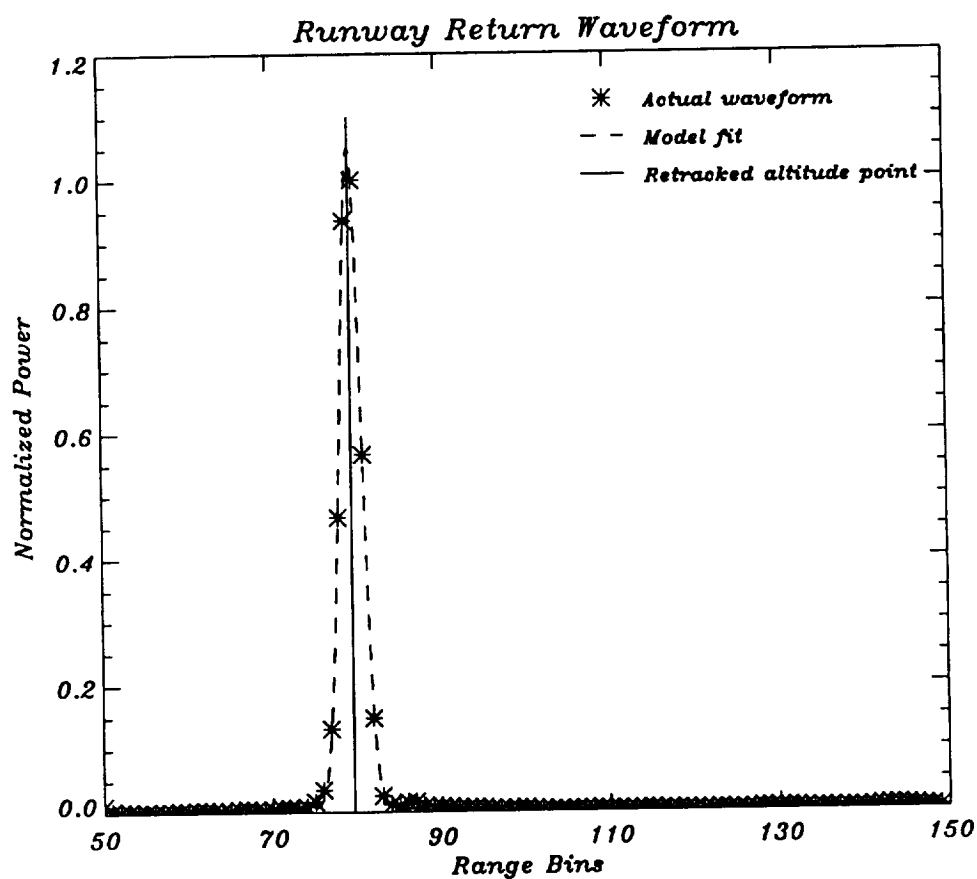
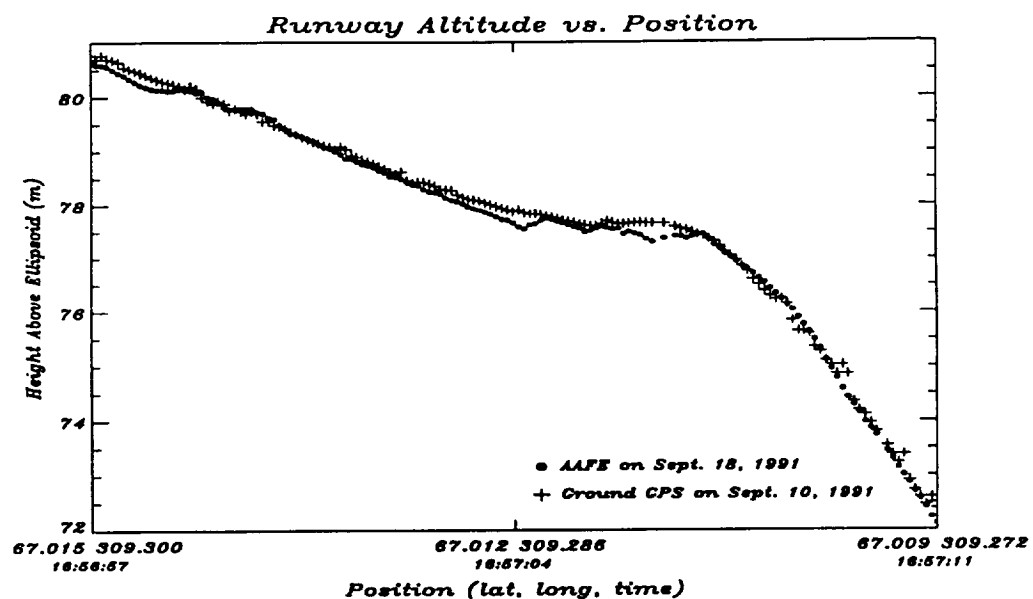
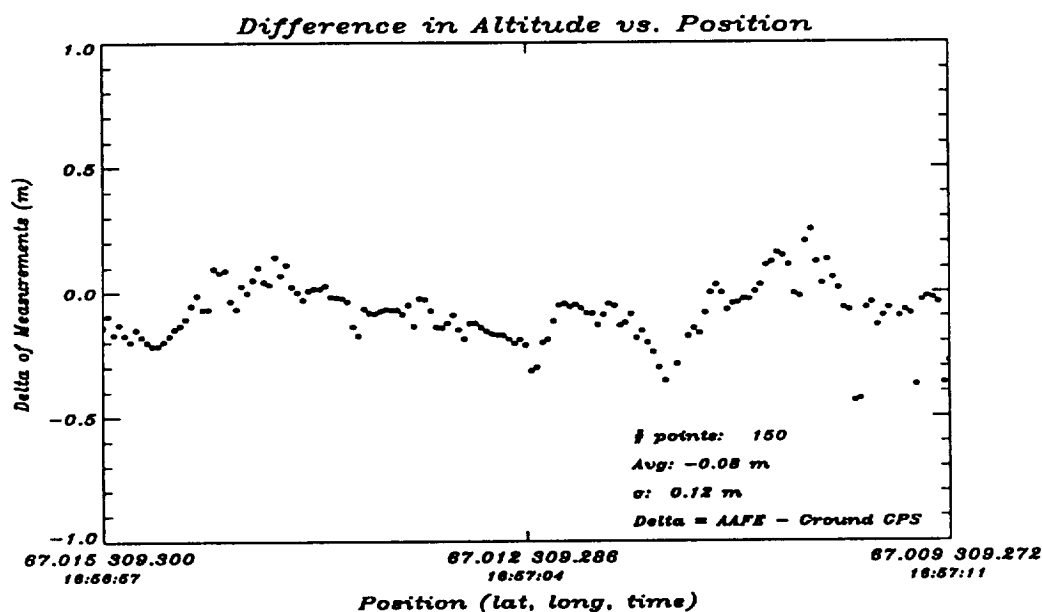


Figure 4.6. A typical AAFE return waveform from the Sondrestrom runway with the actual data points (asterisks), the model fit to the waveform (dashed line) and the resulting retracked altitude point (solid line).



(a)



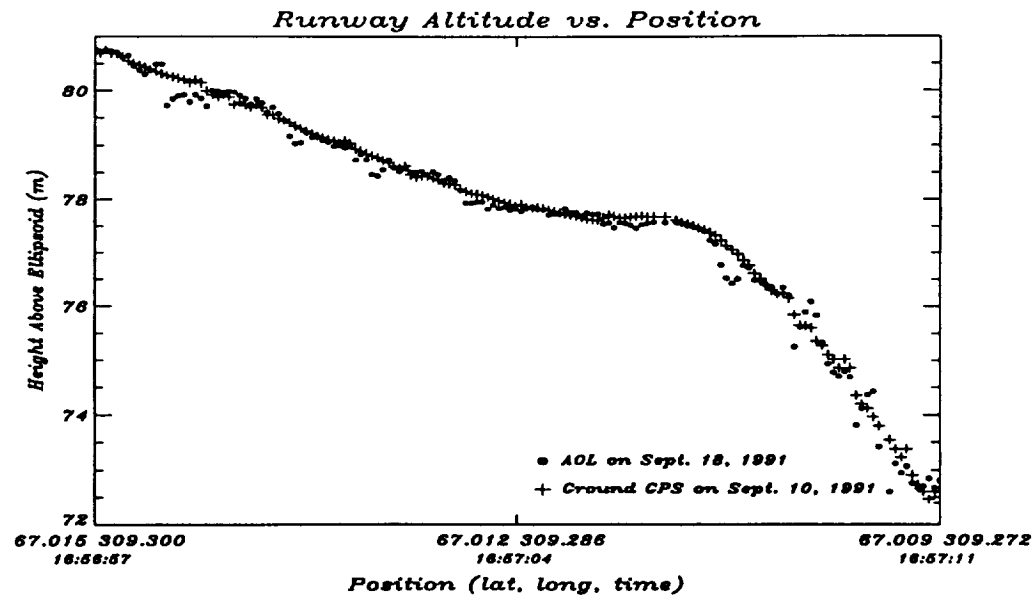
(b)

Figure 4.7. A comparison between the AAFE altimeter altitude measurements on September 18, 1991 and the ground-based GPS altitude measurements on September 10, 1991. (a) The actual AAFE and ground GPS altitude measurements and (b) the difference between the two data sets calculated by subtracting the ground GPS altitude measurements from the AAFE altitude measurements.

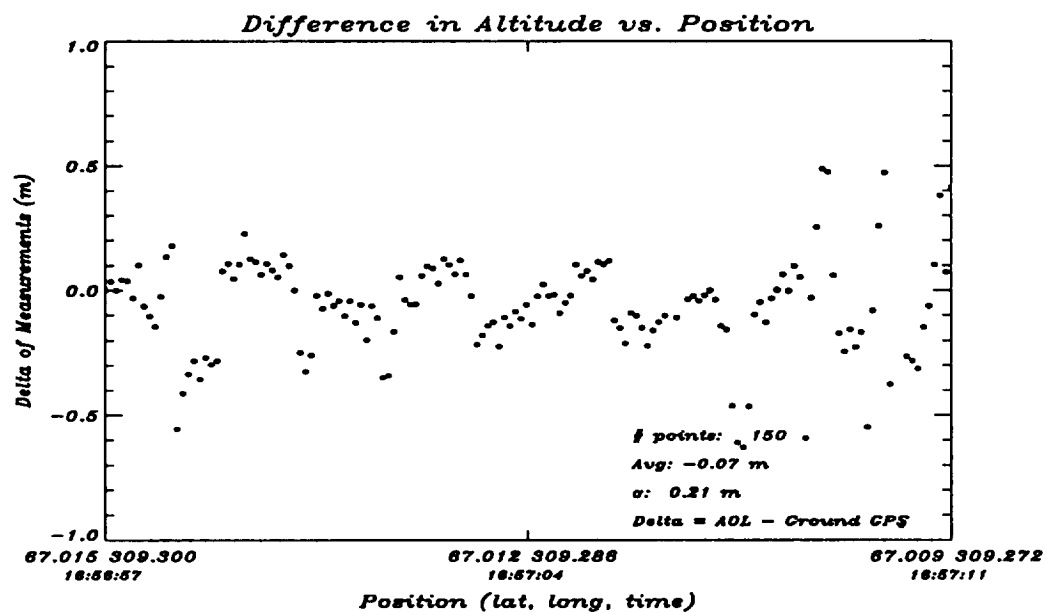
scan at 15° off nadir with 80 observations per scan. Since the AOL is believed to have centimeter altitude precision and its short wavelength prevents it from penetrating into glacial ice, AAFE altimeter measurements have been compared to the AOL to determine accuracy and to study the effects of penetration of the Ku-band AAFE pulse into the ice.

Figure 4.8a compares the AOL runway altitudes on September 18, 1991 and the ground GPS data from September 10, 1991. Taking the difference between the two data sets, as figure 4.8b shows, results in an average difference of -7 cm and a standard deviation of 21 cm. AOL runway data for September 19, 1991, however, only has a mean difference from the ground GPS of -5 cm and a standard deviation of 7 cm. In general, for the 1991 experiment, the bias of the AOL remained less than -5 cm, but the noise level fluctuated between 7 and 21 cm.

To make a comparison with the AOL altitude measurements, each AAFE altimeter waveform is retracked using a least mean-square-error fit to a rough surface scattering model (over the ice sheet) or a flat surface scattering model (over the runway) [Brown, 1977]. A single retracked AAFE altimeter return waveform yields a measurement of the mean altitude within the pulse-limited footprint of the system, which is approximately 40 meters in diameter at an altitude of 450 meters. The AOL, on the other hand, measures the surface altitude in a footprint that is less than .5 meters in diameter. Figure 4.9 illustrates how the AAFE and AOL measurements interact. The solid black circle represents the pulse-limited footprint of the AAFE, the thin black circle shows the extent of the beam of the AAFE and each of the small gray dots represents a single AOL measurement. Approximately 20 to 25 AOL altitude measurements fall within a single AAFE altitude measurement. In order to perform a legitimate comparison of the two altitude measurements, all the AOL data points within the AAFE pulse-limited footprint are averaged into a single altitude measurement before being compared with the AAFE altitude.



(a)



(b)

Figure 4.8. A comparison between the AOL altitude measurements on September 18, 1991 and the ground-based GPS altitude measurements on September 10, 1991. (a) The actual AOL and ground GPS altitude measurements and (b) the difference between the two data sets calculated by subtracting the ground GPS altitude measurements from the AOL altitude measurements.

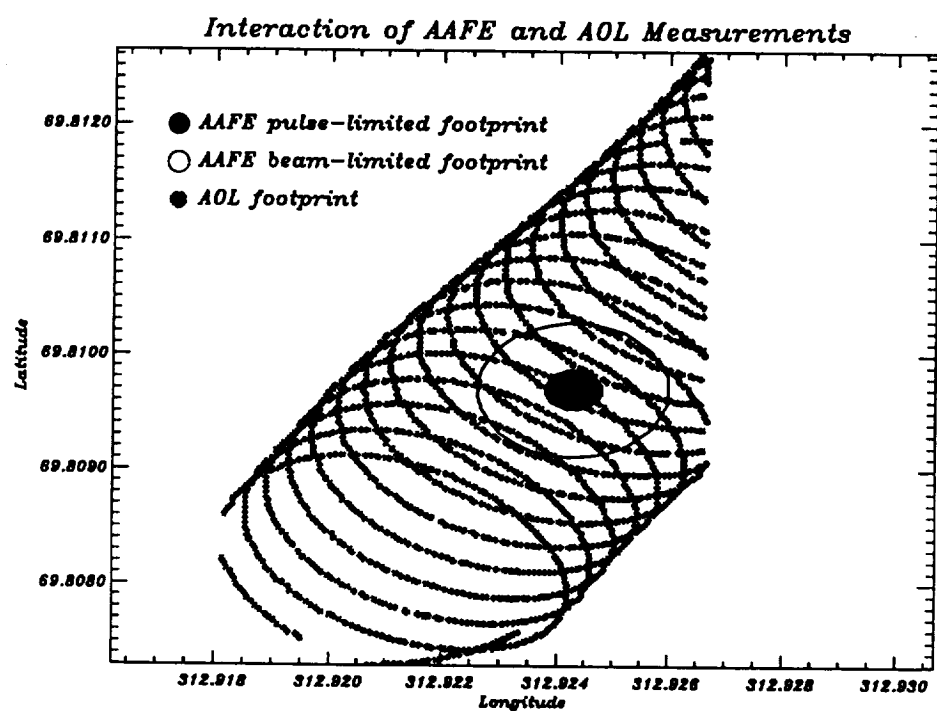
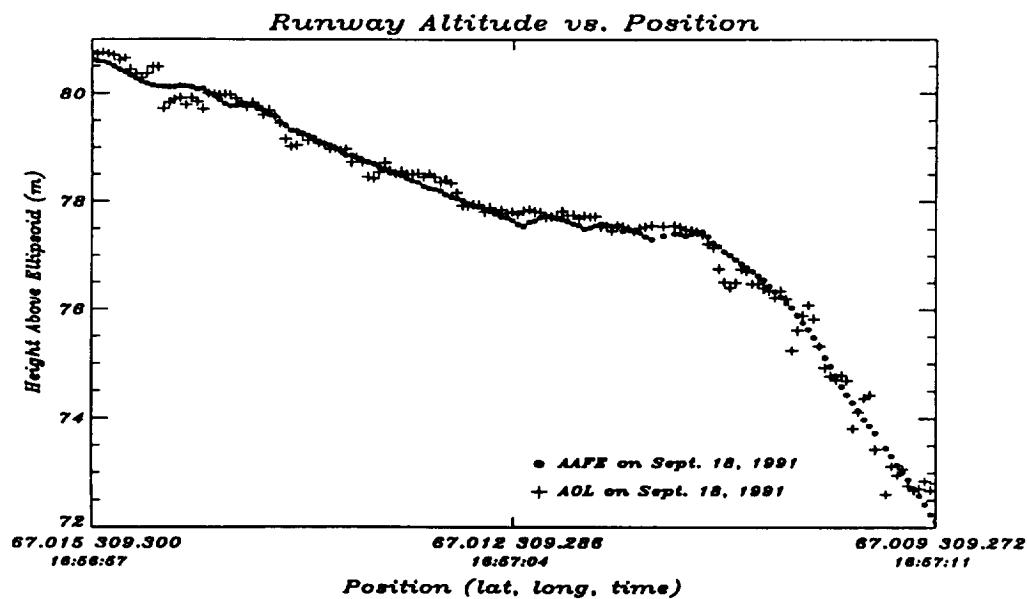


Figure 4.9. Interaction of the AAFE radar altimeter footprint and the AOL laser footprint.

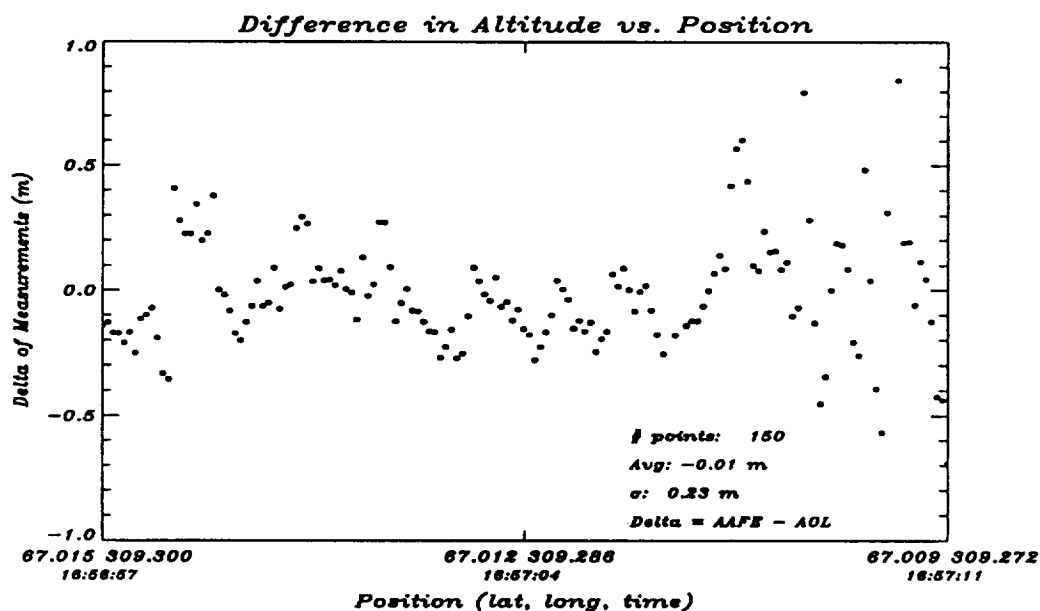
Figure 4.10a displays the AAFE and AOL altitude measurements of the Sondrestrom runway on September 18, 1991, while figure 4.10b shows the difference between the two instruments, which has an average of -1 cm and a standard deviation of 23 cm. The previous comparisons with ground GPS data enable the 23 cm noise level to be broken into its source components of 12 cm from the AAFE and 21 cm from the AOL. This is expected because the variance of the differences should add together, or $12^2 + 21^2 = 23^2$.

Knowing the bias and noise level of each instrument allows comparisons over the Greenland ice sheet to be conducted and areas of penetration to be identified. A comparison between the AAFE and AOL over a 10 kilometer section of the ice sheet is shown in figure 4.11a. In the region of the ice sheet where these data were taken, the water content of the surface snow is high and therefore there is little penetration of the AAFE altimeter pulse into the ice sheet. As the difference plot in figure 4.11b shows, the average difference between the AAFE and AOL is 1 cm and the standard deviation is 13 cm. These results agree with the runway comparisons and demonstrate that both instruments are operating properly over the ice sheet.

On the September 18, 1991 mission the aircraft flew from Sondrestrom toward the north-east portion of the ice sheet and passed over the wet-snow, percolation and dry-snow diagenetic zones. Figure 4.12a shows the AAFE and AOL altitude measurements taken during this flight along with the approximate transitions of the diagenetic zones according to Benson [Benson, 1962]. Since the ice sheet altitude changed from 1200 meters to over 3000 meters, the scale makes it impossible to distinguish between the two sets of measurements. The break in the data at 70.54, 314.00 is due to missing AOL data caused by the laser losing lock on ice fog above the surface of the ice sheet. The -28 cm average difference in figure 4.12b is due to an instrumental bias in the AOL data. This bias has been removed for the comparisons in figure 4.10 and 4.11, but this AOL data set was obtained prior to

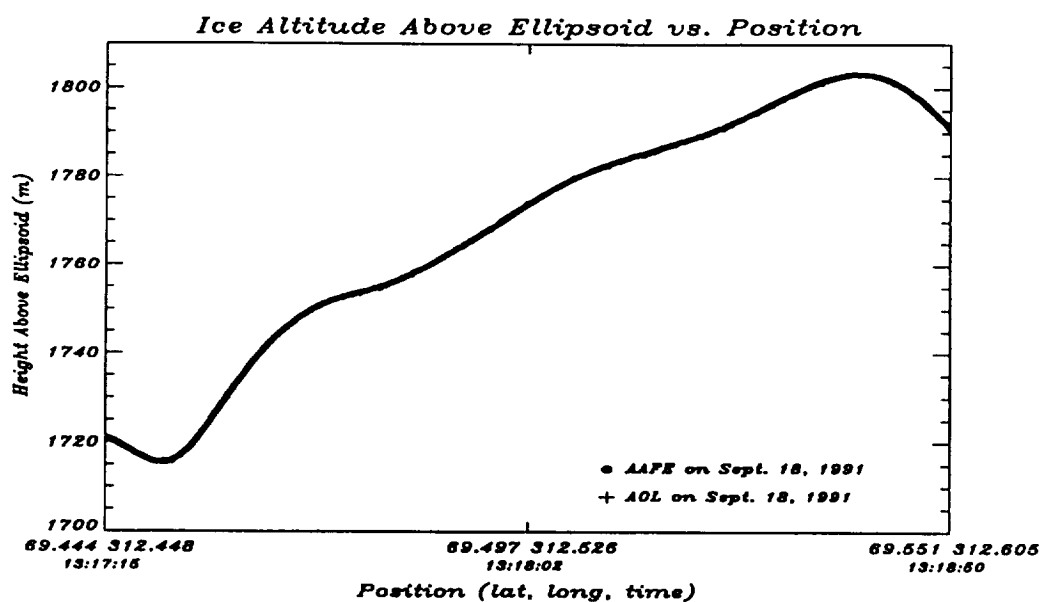


(a)

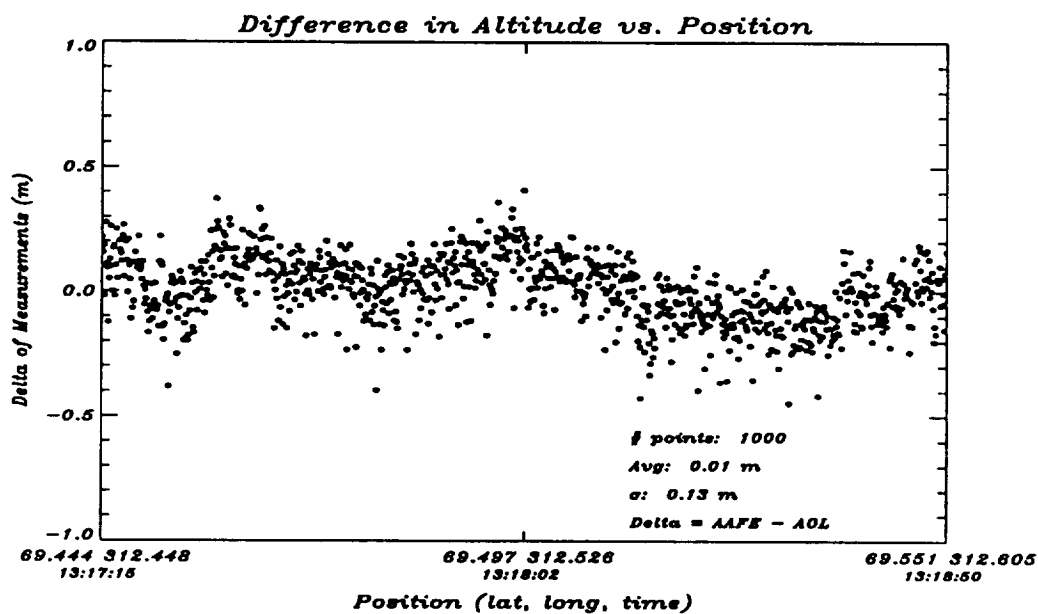


(b)

Figure 4.10. A comparison between AAFE and AOL altitude measurements on September 18, 1991 over the Sondrestrom runway. (a) The actual AAFE and AOL altitude measurements and (b) the difference between the two data sets calculated by subtracting the AOL altitude measurements from the AAFE altitude measurements.

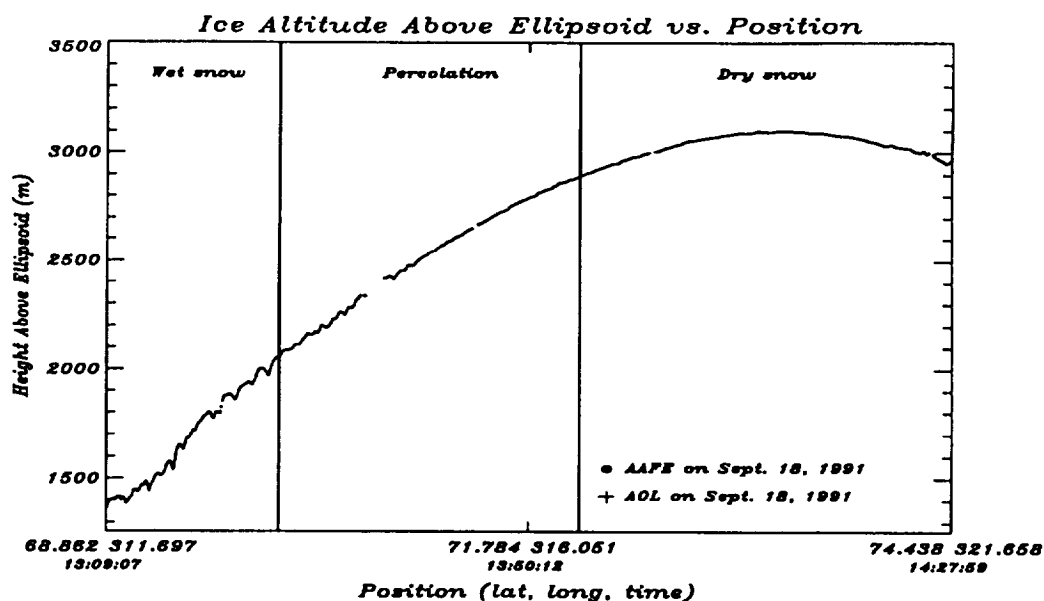


(a)

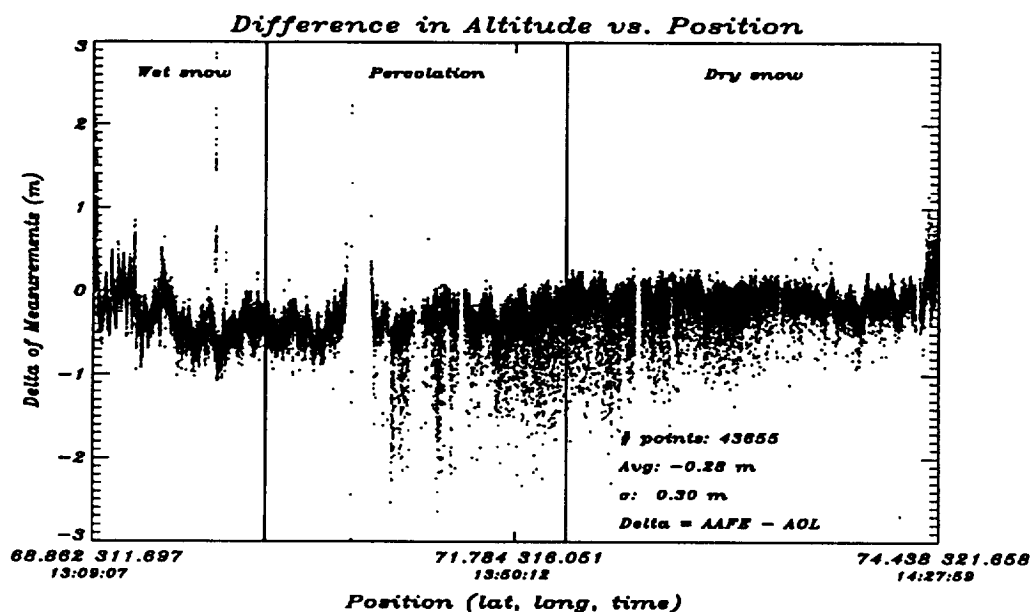


(b)

Figure 4.11. A comparison between AAFE and AOL altitude measurements on September 18, 1991 over a 10 kilometer section of the ice sheet. (a) The actual AAFE and AOL altitude measurements and (b) the difference between the two data sets calculated by subtracting the AOL altitude measurements from the AAFE altitude measurements.



(a)



(b)

Figure 4.12. A comparison between AAFE and AOL altitude measurements on September 18, 1991 over an entire south-west to north-east pass over the ice sheet. (a) The actual AAFE and AOL altitude measurements and (b) the difference between the two data sets calculated by subtracting the AOL altitude measurements from the AAFE altitude measurements.

the discovery of the source of the bias. The plot in figure 4.12b also reveals that the difference between the AAFE and AOL changes in the different regions of the ice sheet. In the wet-snow zone, the two instruments agree very well, except for the large thin spikes on the left side of the difference plot which are due to aircraft maneuvering and a large mispointing angle. In the percolation zone, however, the difference increases dramatically to as much as 2 meters and is then reduced back to 20 cm in the dry-snow zone. This increase in the percolation zone is due to the effects of sub-surface and volume scatterers on the AAFE return waveform. The scattering mechanisms taking place in each of the diagenetic regions are discussed in greater detail in Chapter 5.

4.1.4 Comparison of Flight Line Cross-over Points

During the 1991 Greenland experiment, the aircraft passed over the same areas of the ice sheet many times. In some instances, the pulse-limited footprint of the AAFE altimeter overlapped with the location of the footprint on a previous flight. These aircraft cross-over points are often used to determine system repeatability and analyze system drift. In 1991 there were 14650 points where the area of the AAFE footprint overlapped with a previous measurement by more than 50%. The difference between the two altitude measurements at each cross-over point was calculated and the results are displayed in the histogram in figure 4.13. The two circles in the upper left corner of figure 4.13 illustrate the amount of overlap that occurs between the two AAFE footprints when they cross-over. The mean altitude difference at the cross-over points is -3 cm and the standard deviation is 39 cm.

Since the altitude measurements contain errors from the AAFE radar system, the aircraft GPS receivers and from the aircraft Inertial Navigation System (INS), the 39 cm noise level represents a combination of these errors. The daily runway comparisons showed that the AAFE system noise remained below 14 cm, but since

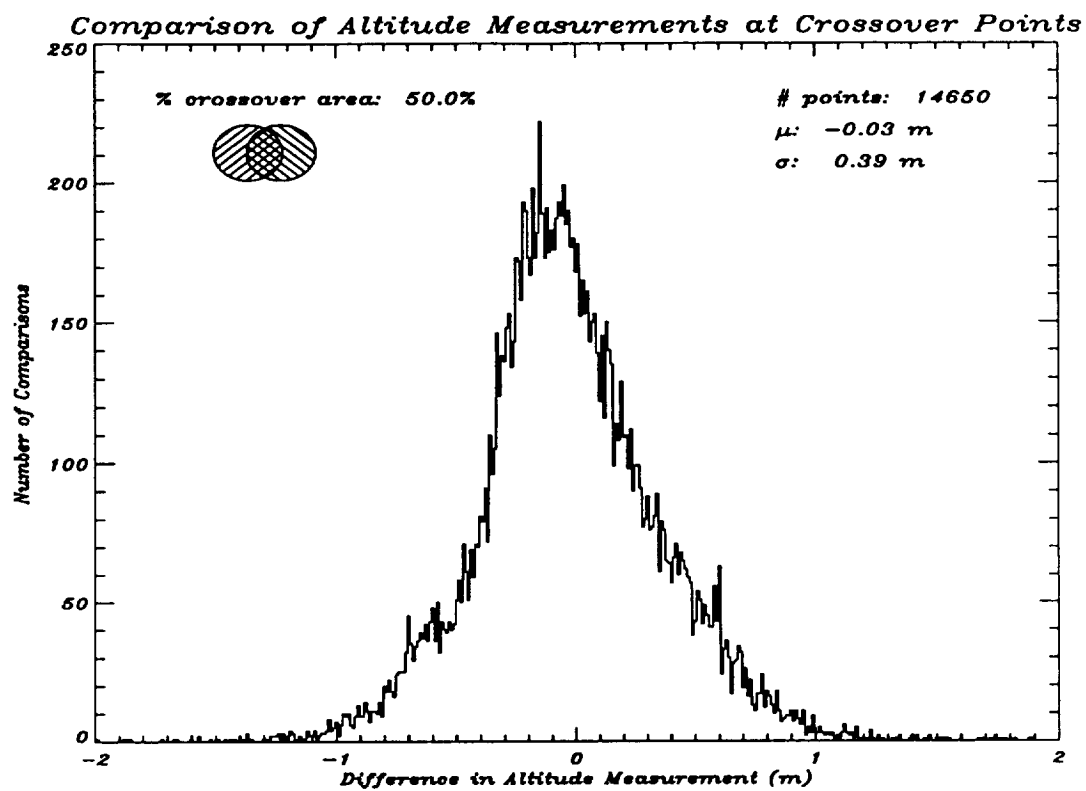


Figure 4.13. A histogram of the difference in altitude at the cross-over points of the AAFE altimeter taken on different days in the 1991 Greenland experiment.

the cross-over points were all obtained on the ice sheet, there may be additional noise due to the effects of sub-surface ice features on the return waveform. Errors in the aircraft GPS measurements are mainly from varying satellite configurations during the course of a flight. On several of the missions, the aircraft made a south-west to north-east pass in the morning and returned on a north-east to south-west pass over the same area in the afternoon. Figure 4.14 shows a histogram of these cross-over points taken on the same day. The 27 cm average reveals that the GPS altitude measurements are changing by this amount during the course of the day. Since the GPS receivers are calibrated before the beginning of a flight, the GPS measurements taken with the same satellite configuration have 1 to 3 cm accuracy. During the course of the flight, however, the satellite configuration changes and measurements taken 5 to 6 hours later have 20 to 30 cm accuracy [Krabill, 1994]. This explains the 27 cm bias in figure 4.14. In the 1993 experiment, this problem was somewhat alleviated because a larger number of satellites were in orbit. By keeping lock on several satellites at once, the GPS receiver can reduce errors such as ionospheric delays and orbital errors. In 1991, however, these errors could only be reduced when the GPS receiver was stationary or within close proximity of a stationary receiver.

4.1.5 Altitude Results

All of the AAFE return waveforms for the 1991 experiment have been retracked and the resulting elevations measured by the radar are shown in figure 4.15. Although the detail and accuracy of the AAFE data is not shown, the map reveals the general topography of Greenland and the location of the summit and lower dome of the ice sheet.

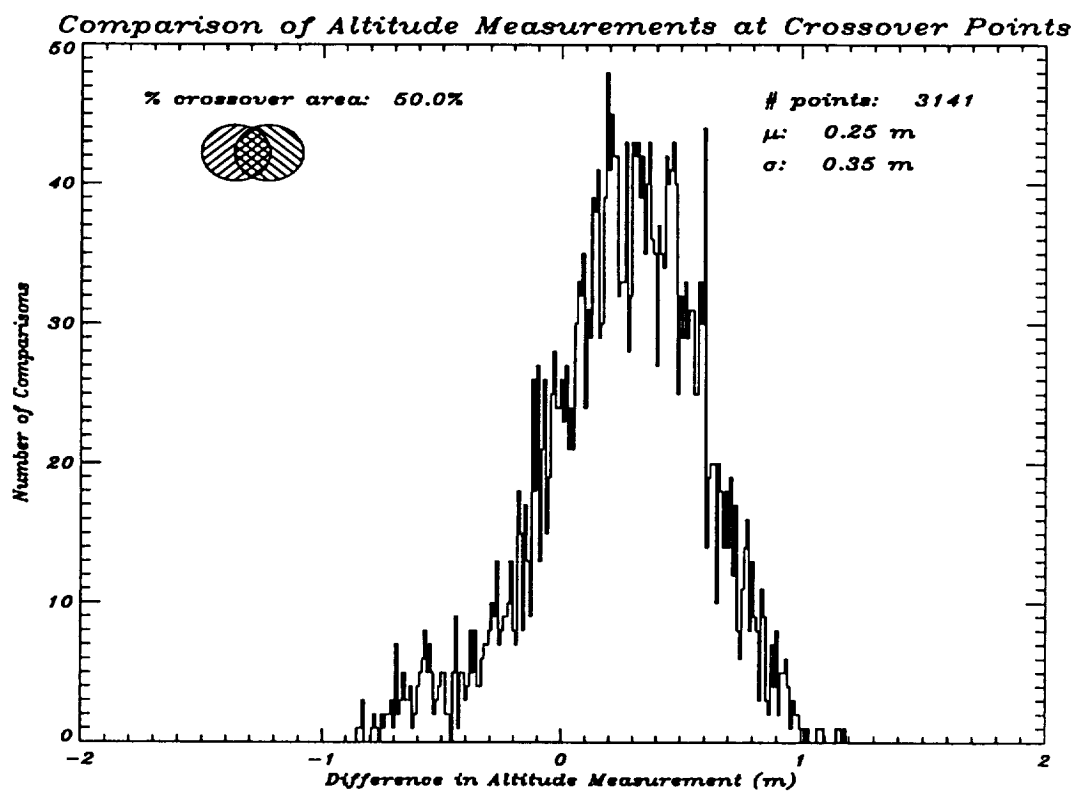


Figure 4.14. A histogram of the difference in altitude at the cross-over points of the AAFE altimeter taken on the same day in the 1991 Greenland experiment.

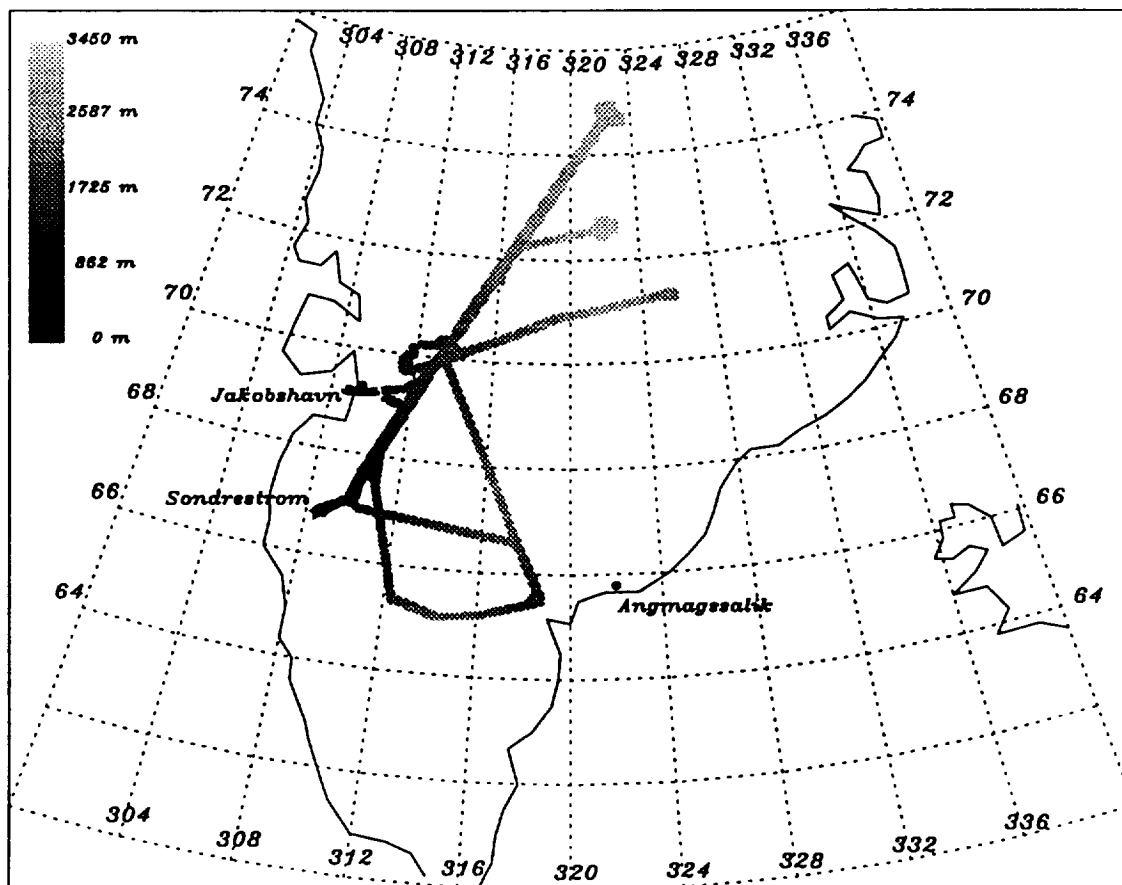


Figure 4.15. A map of the elevations measured by the AAFE altimeter in the 1991 experiment. The location of the highest measured elevation at 72.8° N latitude, 322.0° longitude and the lower dome near 65.2° N latitude, 314.0° longitude can be noted.

4.2 1993 Greenland Experiment

4.2.1 Experiment Description and Flight Lines

In 1993 the AAFE radar altimeter, AOL laser altimeter and ATLAS laser altimeter all participated in the Greenland experiment again, but the SCR was replaced by the Coherent Antarctic Radar Depth Sounder (CARDS) built by the University of Kansas. Between June 23 and July 9, 1993 the NASA P-3 aircraft flew eleven missions that covered an area between and 61° N and 74° N on the ice sheet. Although a larger portion of Greenland was mapped during this experiment, fewer flight lines were repeated than in 1991. Figures 4.16, 4.17 and 4.18 are maps of each of the individual flight lines in the 1993 experiment and figure 4.19 shows all of the flight lines combined on a single map. Again, differential GPS receivers were used to increase position accuracy, but they were only placed in Sondrestrom for this experiment.

During the 1993 airborne experiment, a ground truth experiment was also conducted on the ice sheet at Dye 2 (66.48° N latitude, 313.73° longitude), which is in the percolation zone. A sample distribution of the ice layers, lenses and pipes was obtained by probing a 5 x 3 meter area of the snow pack. Measurements of snow density, dielectric constant, temperature and crystal size were also acquired down to a depth of 2 meters at several sites around Dye 2. During the four week period of the experiment, the AAFE radar altimeter flew directly over the Dye 2 camp site five times, obtaining waveforms during several stages of the melt period. Radar measurements were also taken with a small Ku-band ground-based FMCW radar, built and operated by the Ohio State University [Zabel et al., 1994].

In addition, a ground crew traversed from 69.8° N latitude, 313.0° longitude to 65.1° N latitude, 314.32° longitude on snowmobiles carrying several GPS receivers

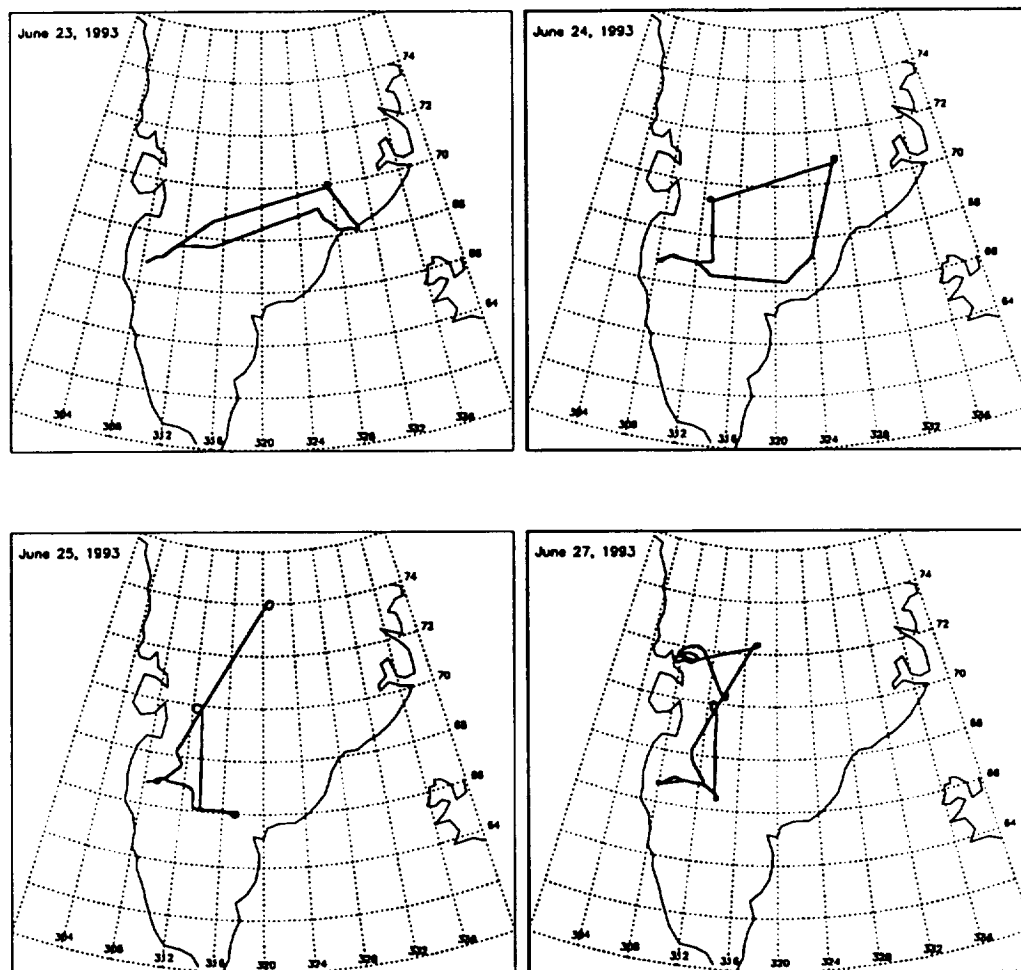


Figure 4.16. The first four flight lines in the 1993 Greenland experiment.

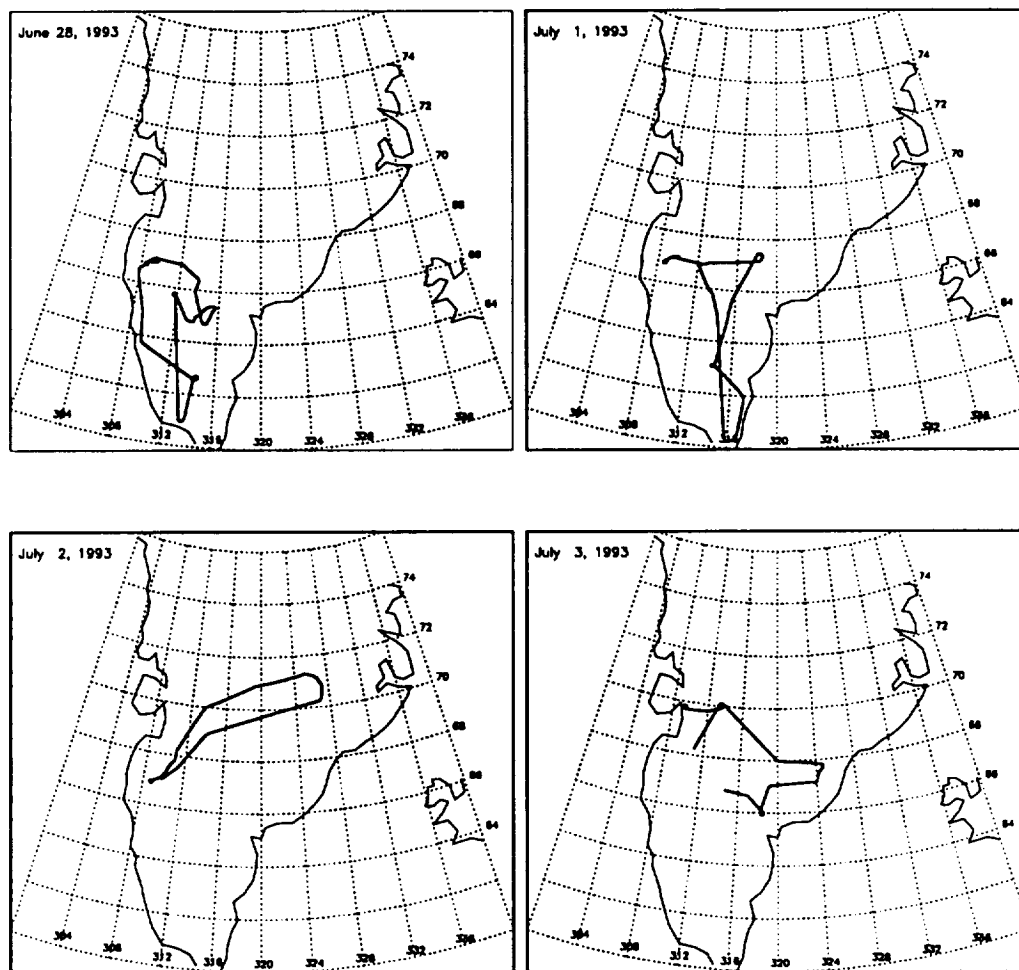


Figure 4.17. The fifth through eighth flight lines in the 1993 Greenland experiment.

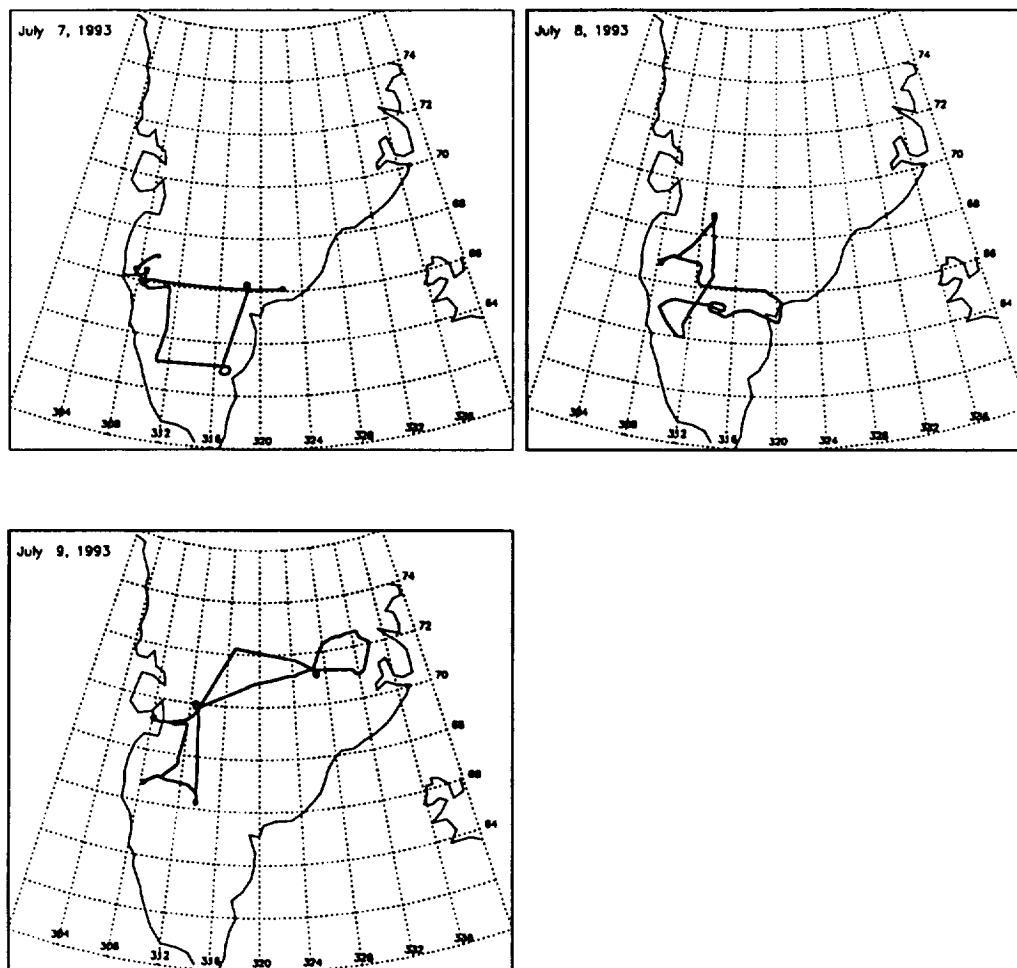


Figure 4.18. The final three flight lines in the 1993 Greenland experiment.

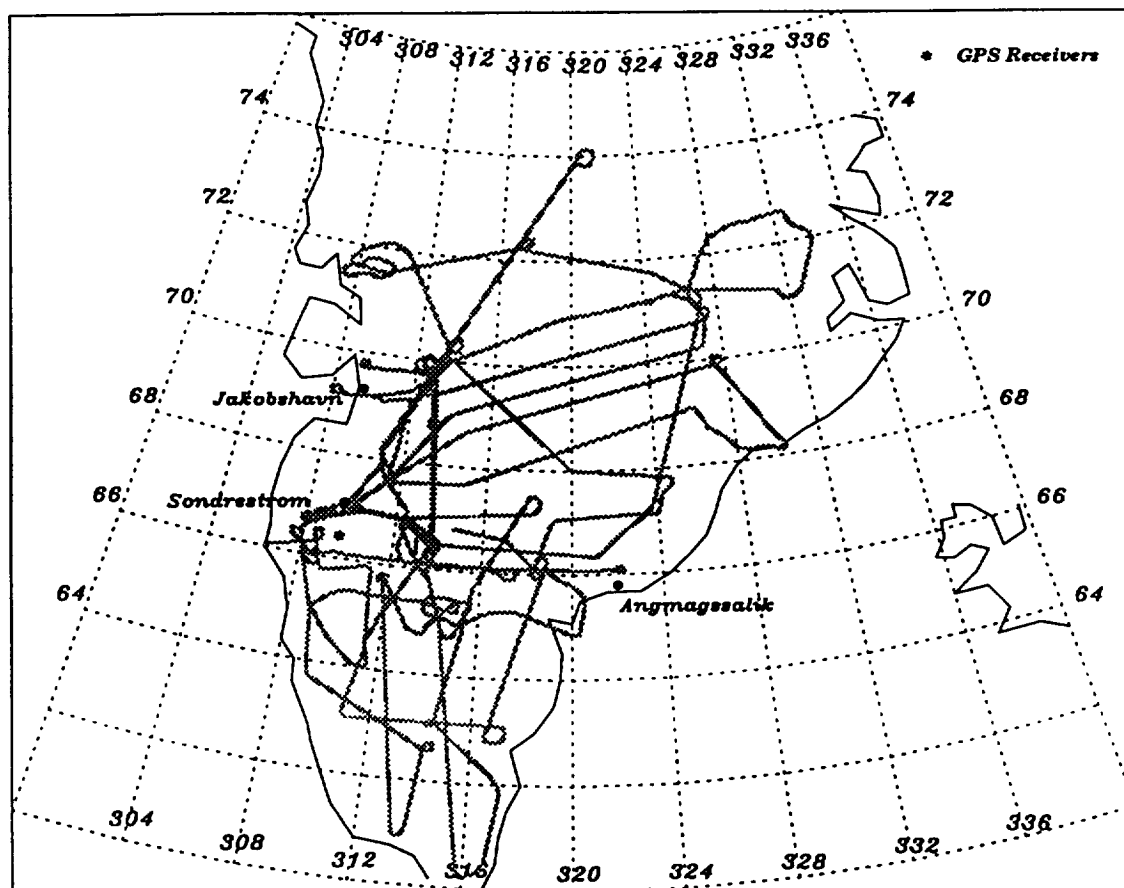


Figure 4.19. All of the flight lines in the 1993 Greenland experiment and the location of the differential GPS receivers.

mounted on sleds. The aircraft also flew over this traverse line several times during the experiment.

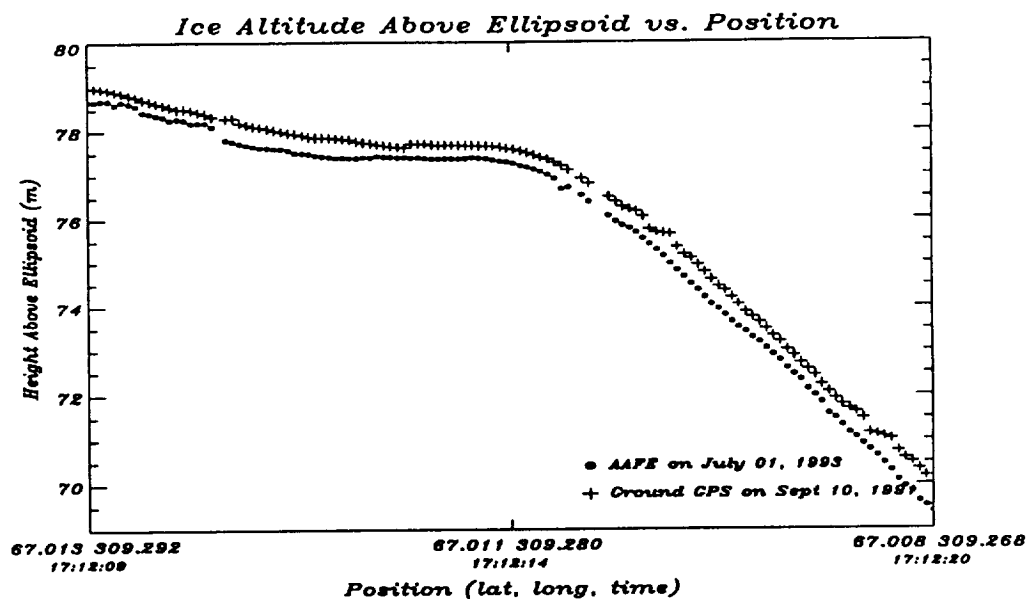
4.2.2 Runway Ground Truth Comparison

Figure 4.20a is a comparison between AAFE runway data on July 1, 1993 and GPS ground truth data taken on September 10, 1991. The difference plot in figure 4.20b shows that the AAFE has a bias of 41 cm and a noise level of 12 cm. Although the AAFE radar was calibrated for the 1993 experiment, it is possible this increased system bias is due to an error in the measurement of the waveguide length. The system noise level for the 1993 experiment fluctuates between 12 and 21 cm for different runway passes. This increase in the noise level is due to a degradation in the system signal-to-noise ratio. A failing 1620 MHz amplifier in the radar receiver caused a significant increase in the instrument noise figure and reduced output power from the 1974 Traveling Wave Tube (TWT) amplifier resulted in lower transmitted signal power. The failed amplifier has been replaced and a 2 watt solid state amplifier is now used instead of the TWT.

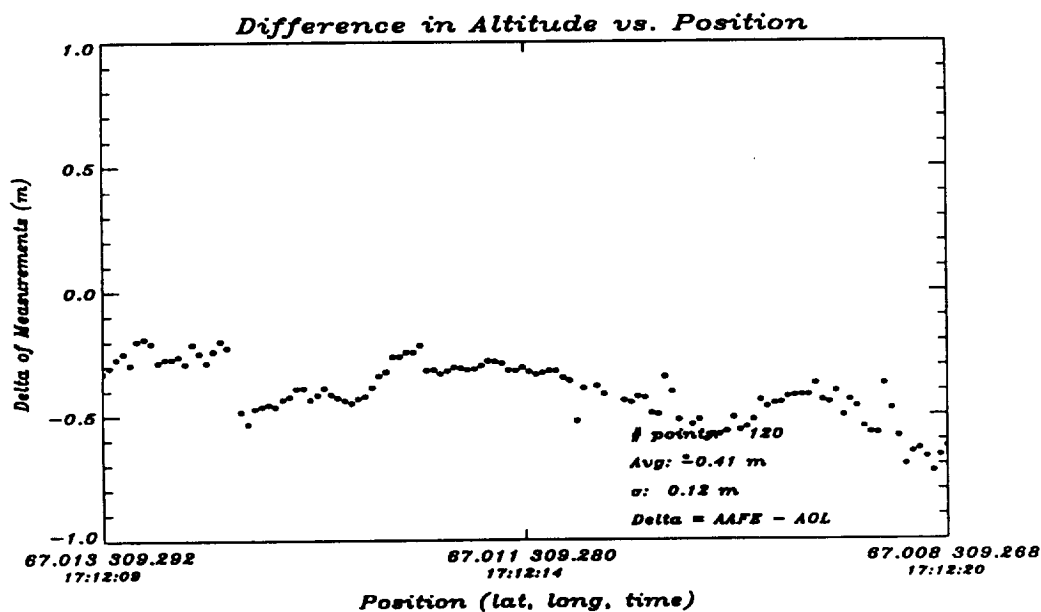
The maximum range resolution of the AAFE altimeter measurements for the 1993 Greenland experiment is determined to be 21 cm based on the runway comparison results. These results are preliminary, however, because the 1993 GPS aircraft data are still being processed.

4.2.3 Altitude Results

Figure 4.21 shows preliminary altitude results for the entire 1993 Greenland experiment. Some of these measurements were processed without INS data and others with preliminary GPS files, so the altitudes may have an error of up to 4 meters. Despite this, the map reveals the general topography of the ice sheet and covers a much greater area than the 1991 results shown in figure 4.15.



(a)



(b)

Figure 4.20. A comparison between the AAFE altimeter altitude measurements on July 1, 1993 and the ground-based GPS altitude measurements on September 10, 1991. (a) The actual AAFE and ground GPS altitude measurements and (b) the difference between the two data sets calculated by subtracting the ground GPS altitude measurements from the AAFE altitude measurements.

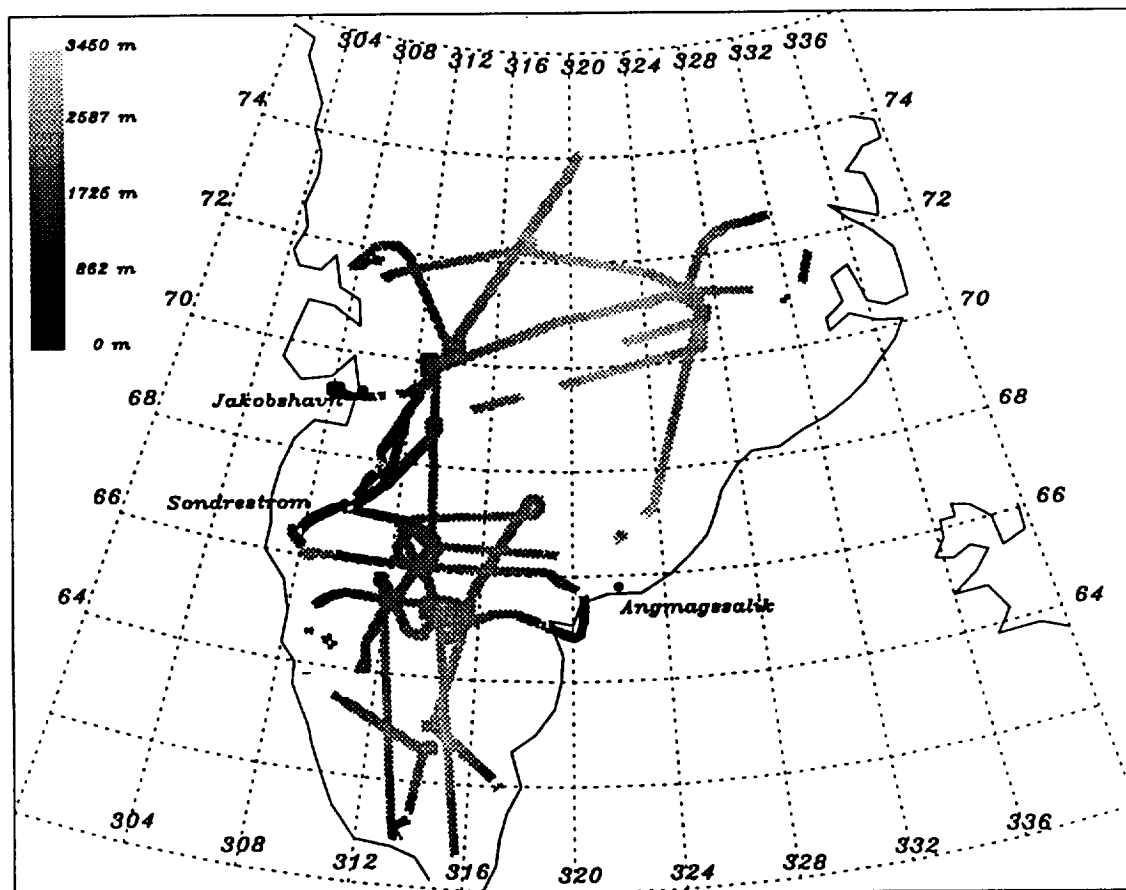


Figure 4.21. A map of the elevations measured by the AAFE altimeter in the 1993 experiment.

4.3 Comparison of 1991 and 1993 Elevation Measurements

Although a large area of the ice sheet was covered in the 1993 Greenland experiment, most of the 1991 flight lines were not repeated. Figure 4.22 shows the major segments that were measured in both 1991 and 1993. The European Glaciologique International au Groenland (EGIG) line (solid line) was covered on September 4, 1991 and on July 9, 1993 while, the ERS-1 line (dashed line) was measured on September 18, 19 and 20 in 1991 and on June 27 and July 9 in 1993.

The AAFE altitude measurements of the ERS-1 line from September 18, 1991 and July 9, 1993 are shown in figure 4.23a. The scale makes it impossible to distinguish between the two data sets, but the difference plot in figure 4.23b shows an average change of -26 cm. Using the 1991 and 1993 system biases determined in figures 4.7 and 4.20, the actual average altitude change is $(1993 \text{ alt} + 41 \text{ cm}) - (1991 \text{ alt} + 8 \text{ cm}) = (-26 \text{ cm} + 33 \text{ cm}) = 7 \text{ cm}$. Since the 71 cm standard deviation of the difference far exceeds this mean, no conclusions can be drawn about the growth or decay of the ice sheet. The undulations on the far left side of the difference plot are approximately 2 meters high and 10 km wide. These variations correspond in location to the hummocks in the actual altitude measurements of figure 4.23a, therefore they may be due to slight shifts in the ice sheet. They may also be the result of the spatial difference between the two flight lines. As figure 4.23c shows, the horizontal distance between the location of the 1991 altitude measurement and the 1993 altitude measurement usually remained less than 100 meters, however, the left side of figure 4.23c has undulations that are equivalent in frequency to those in figure 4.23b. This reveals one of the difficulties in measuring ice sheet small scale surface changes, which is distinguishing between actual changes in altitude and deviations due to horizontal displacement.

Figures 4.24a and 4.24b show the AAFE altitude measurements of the EGIG line from September 4, 1991 and July 9, 1993 and the difference between the two

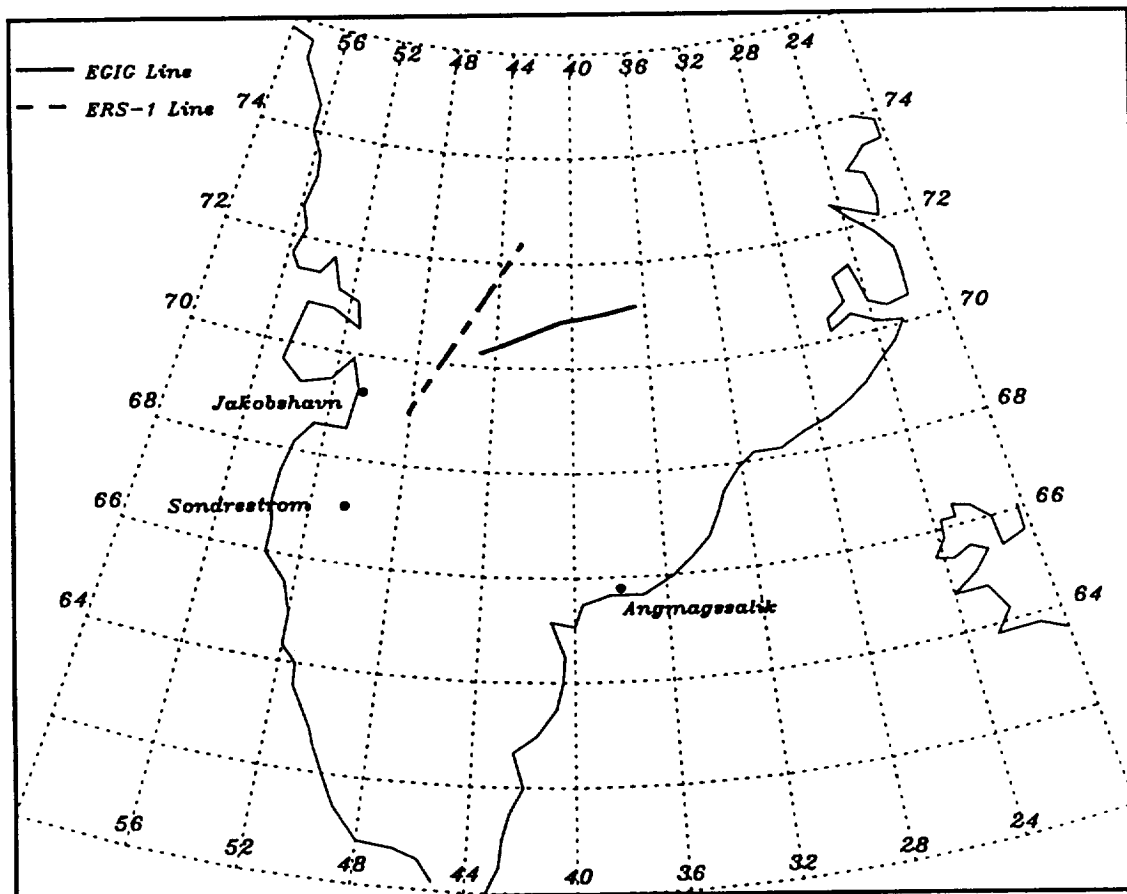


Figure 4.22. A map of the major areas that were covered in both the 1991 and 1993 Greenland experiments.

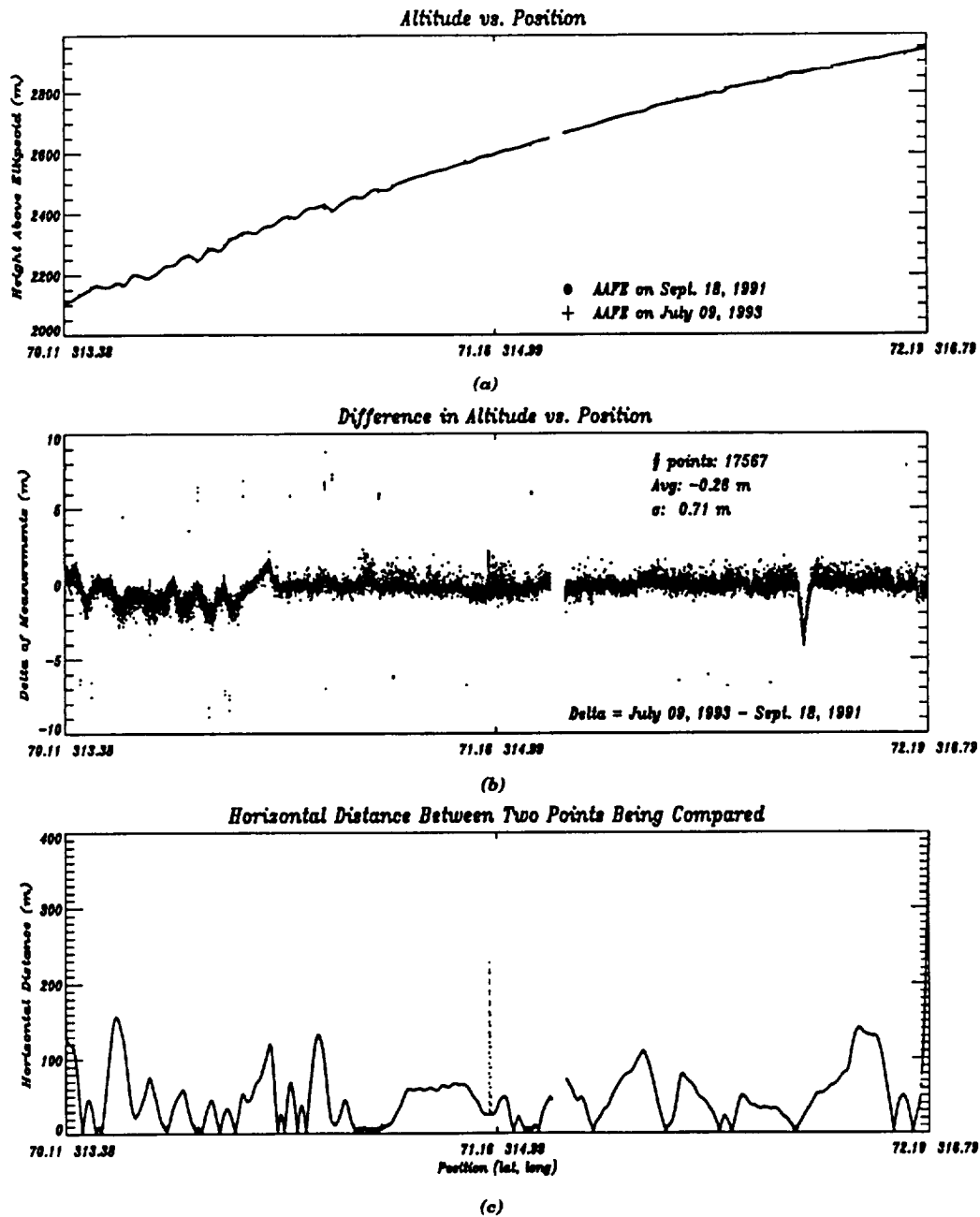


Figure 4.23. A comparison between AAFE altitude measurements of the ERS-1 line on September 18, 1991 and July 9, 1993. (a) The actual altitude measurements, (b) the difference between the two data sets calculated by subtracting the 1991 data from the 1993 data and (c) the horizontal distance between the location of the 1991 altitude measurement and the 1993 altitude measurement.

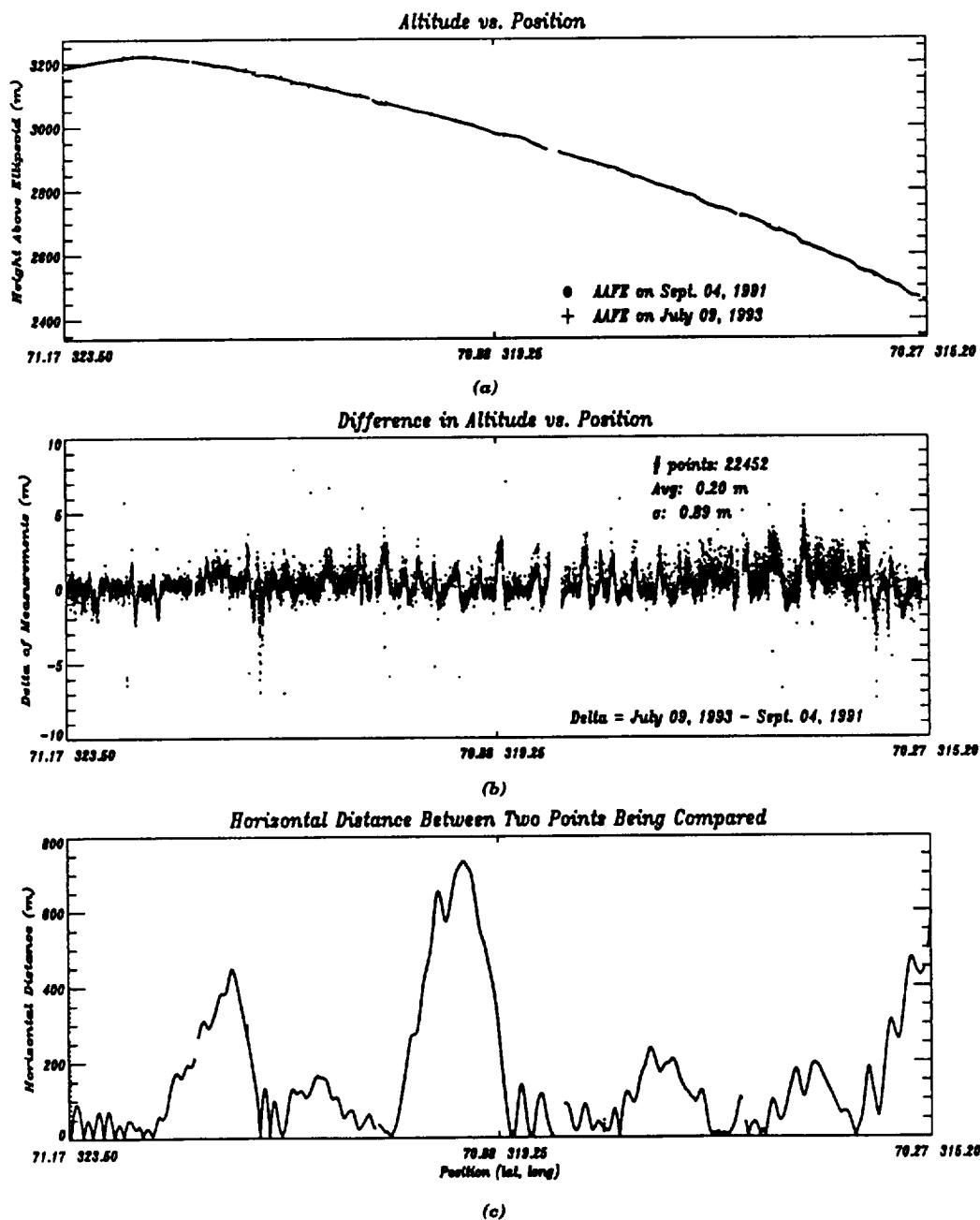


Figure 4.24. A comparison between AAFE altitude measurements of the EGIG line on September 4, 1991 and July 9, 1993. (a) The actual altitude measurements, (b) the difference between the two data sets calculated by subtracting the 1991 data from the 1993 data and (c) the horizontal distance between the location of the 1991 altitude measurement and the 1993 altitude measurement.

data sets, respectively. Over this section of the ice sheet there has been an average increase in ice altitude of $(20 \text{ cm} + 33 \text{ cm})$ or 55 cm. Again the 89 cm noise level makes it difficult to identify changes in the ice sheet, but it appears there has been little variation between 1991 and 1993. Oscillations appear again in the difference plot, but they occur over most of the flight line and at a much higher frequency. Their spike-like appearance suggests they are probably the result of a system error and since they do not show up in AAFE comparisons with the AOL over the same section of the ice sheet, they are not an artifact of the AAFE system. They could, however, be an artifact of the GPS or INS data, which both the AAFE and AOL use to calculate the final altitude. Another possible cause is the increased spatial difference in the two EGIG flight lines. As figure 4.24c shows, the two flight lines often deviated by more than 400 meters.

Although it is too early to derive conclusions from the 1991 to 1993 ice sheet elevation comparisons, future flights over these lines will help build a data base and allow long term changes to be monitored.

CHAPTER 5

ANALYSIS OF WAVEFORMS FROM THE GREENLAND ICE SHEET

The 1991 and 1993 experimental flights over Greenland passed over the wet-snow, percolation and dry-snow diagenetic zones of the ice sheet and, as the six representative waveforms in figure 5.1 show, the AAFE radar altimeter returns received from the various zones differed significantly in shape. Each of the waveforms in figure 5.1 is normalized in power with a single range bin equivalent to 2.77 nanoseconds or 41.67 centimeters and the latitude and longitude where each waveform was received along with the ice altitude above the ellipsoid at that point are noted. These variations in the waveform shape are due to differences in the scattering properties of the various zones of the ice sheet. Figure 5.2 shows the boundaries of the diagenetic zones in Greenland as well as the location on the ice sheet where each waveform was obtained. Waveforms 1 and 2, which have a large slope or sharp leading edge and a sharp trailing edge, come from the wet-snow zone. The trailing edges on waveforms 3 and 4, which are from the percolation zone, have a smaller slope than waveforms 1 and 2, while the leading edges remain sharp. Waveform 6, which was obtained near the summit in the dry snow zone, still has a sharp leading edge, but the trailing edge is long and gently sloping.

The interaction of the AAFE altimeter 13.9 GHz pulse with the different diagenetic zones can be determined by calculating the dielectric properties of the snow and the depth of penetration in each region. Since snow is a heterogeneous mixture of air, ice and liquid water, which all have known dielectric constants, the dielectric constant of snow, ϵ_s , can be approximated. Measurements in the microwave region

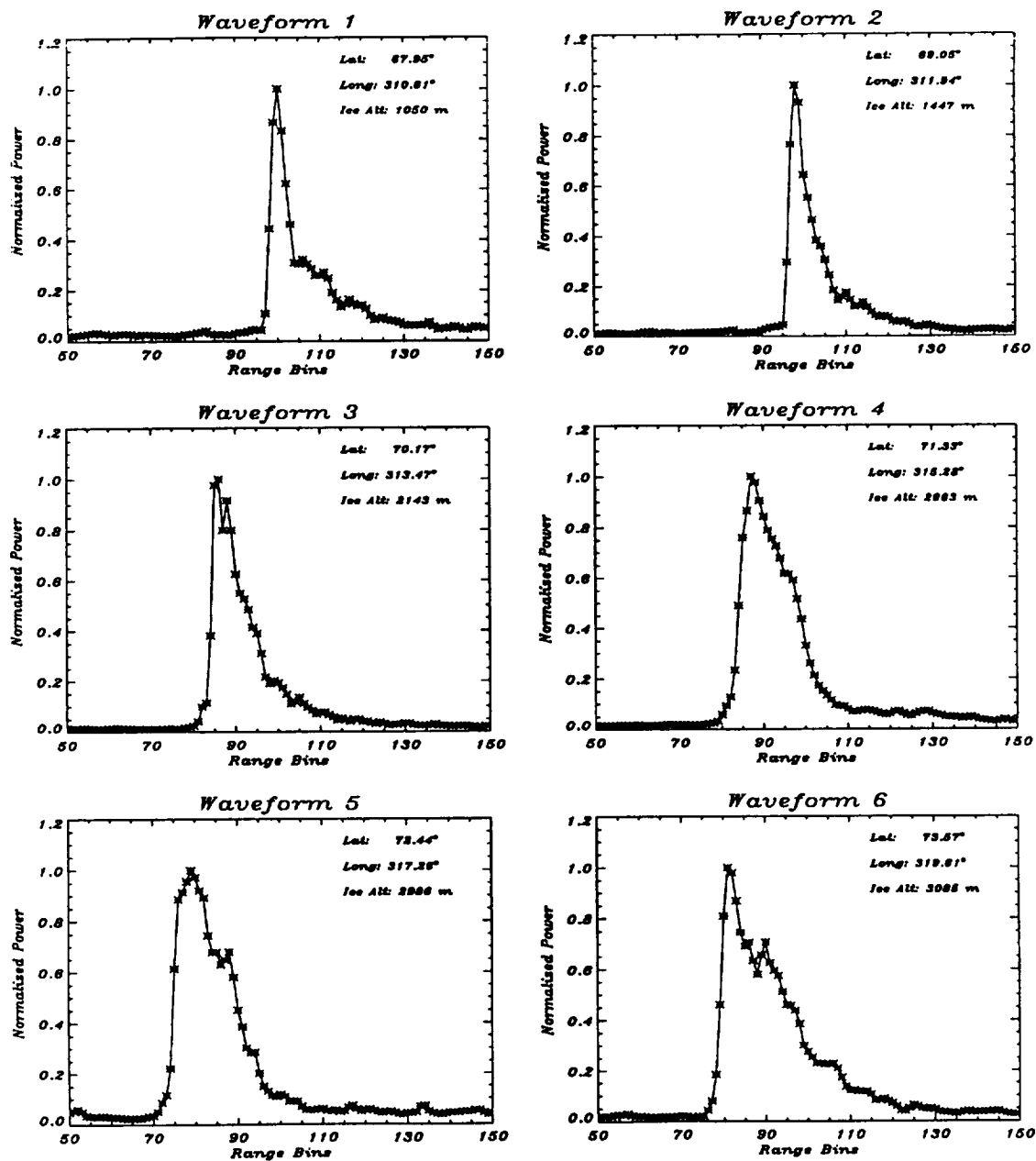


Figure 5.1. Six altimeter return waveforms from the Greenland ice sheet.

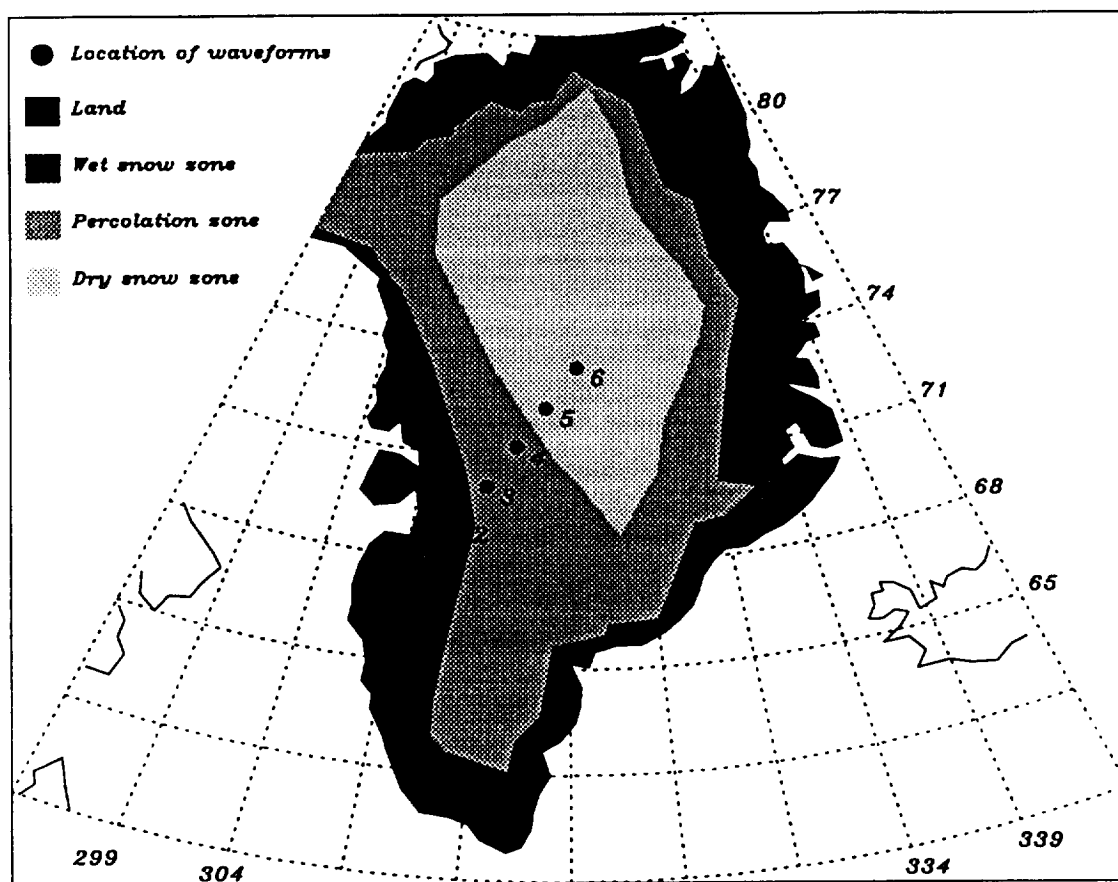


Figure 5.2. Distribution of the diagenetic zones in Greenland according to Benson and the location of the six altimeter waveforms of figure 5.1.

show that at a given frequency ϵ_s depends mainly on the density of the snow, ρ_s , and the percentage of liquid water content, m_v . As the percentage of liquid water content increases, both the real, ϵ'_s , and imaginary, ϵ''_s , parts of the dielectric constant increase. An increase in density also causes an increase in the dielectric constant. This increase, however, mainly affects the real part of ϵ_s . Dry snow, which has a liquid water content of zero, has an ϵ'_s that depends only on the snow density and an ϵ''_s that depends on the snow density and on the dielectric constant of pure ice, ϵ_i , at the measurement frequency [Ulaby et al., 1986]. Models, such as the Debye-like model and the Polder Van Santeen model can be used to calculate the dielectric constant of snow. For snow that has some water content, the Debye-like model approximates the dielectric constant, ϵ_{ws} , as

$$\begin{aligned}\epsilon'_{ws} &= 1 + 1.83\rho_s + .02m_v^{1.015} + \frac{.073m_v^{1.31}}{1 + (f/f_o)^2} \\ \epsilon''_{ws} &= \frac{.073(f/f_o)m_v^{1.31}}{1 + (f/f_o)^2}\end{aligned}\quad (5.1)$$

where the effective relaxation frequency of wet snow, f_o , is 9.07 GHz [Hallikainen et al., 1986]. On the other hand, the Polder Van Santeen model approximates the dielectric constant of dry snow, ϵ_{ds} , as

$$\begin{aligned}\epsilon'_{ds} &= (1 + .51\rho_s)^3 \\ \epsilon''_{ds} &= 3.275\rho_s\epsilon''_i \frac{(\epsilon'_{ds})^2(2\epsilon'_{ds} + 1)}{(\epsilon'_i + 2\epsilon'_{ds})(\epsilon'_i + 2(\epsilon'_{ds})^2)}\end{aligned}\quad (5.2)$$

[Ulaby et al., 1986]. Both models agree well with measured results [Stiles and Ulaby, 1980], [Ulaby and Stiles, 1980], [Hallikainen et al., 1986]. Once the dielectric constant of snow at 13.9 GHz has been estimated, the attenuation coefficient, α , and the depth of penetration, δ_p , at this frequency are calculated using

$$\alpha = \frac{2\pi}{\lambda} |Im\sqrt{\epsilon}| \quad (5.3)$$

and

$$\delta_p = \frac{1}{2\alpha} \quad (5.4)$$

[Ulaby et al., 1982]. Knowing the depth of penetration, the type of scattering in the wet-snow, percolation and dry-snow zones can be determined and used to model the altimeter return waveform.

5.1 Scattering Models of the Diagenetic Zones of Greenland

5.1.1 Wet-snow Zone Model

Studies of the wet-snow zone in Greenland reveal that the upper layers of snow are wet and dense due to melting. Measurements of snow density range from .4 to .6 g/cm³ [Benson, 1962], and the percentage of liquid water content may be as high as 3%. Estimating the dielectric constant of the snow using the Debye-like model and then calculating α and δ_p with equations 5.3 and 5.4 gives an attenuation coefficient greater than 21 Np/m or 186 dB/m, and a depth of penetration less than 2.0 cm at 13.9 GHz. As a result, there is little surface penetration at 13.9 GHz and the radar altimeter returns are predominantly due to surface scattering.

Surface scattering from a randomly distributed rough surface has been described by Brown [Brown, 1977] as the convolution of the flat surface impulse response with the distribution of height scatterers. The flat surface impulse response, $P_{fs}(t)$, is calculated by assuming a transmitted impulse and using the radar range equation

$$P_{fs}(t) = \frac{P_t \lambda^2}{(4\pi)^3} \int_{\text{illum area}} \frac{\delta(t - \frac{2R}{c}) G^2(\theta) \sigma^o(\theta)}{R^4} dA \quad (5.5)$$

where the gain of the radar antenna is approximated as

$$G(\theta) = G_o e^{-4 \ln 2 \theta^2 / \theta_B^2} \quad (5.6)$$

[Barrick, 1972]. The backscatter coefficient for the surface is

$$\sigma^o(\theta) = \frac{\Gamma(0^\circ)}{s^2 \cos^4 \theta} e^{-\tan^2 \theta / s^2} \quad (5.7)$$

[Jackson et al., 1992] where $\Gamma(0^\circ)$ is the power reflection coefficient at nadir and s is the rms surface slope, but for small incidence angles, it can be approximated by

$$\sigma^o(\theta) = \frac{\Gamma(0^\circ)}{s^2} e^{-\theta^2/s^2}. \quad (5.8)$$

Convolving $P_{fs}(t)$ with a Gaussian height distribution of scatterers with a standard deviation of σ_h leads to a rough surface impulse response of

$$P_{rs}(\tau) = \frac{C_0}{H^3 s^2} e^{(t_p/t_s)^2} e^{-(2\tau/t_s)} \text{erfc}\left(\frac{t_p}{t_s} - \frac{\tau}{t_p}\right) \quad (5.9)$$

where

$$C_0 = \frac{P_t \lambda^2 G_o^2 \Gamma(0^\circ)}{32\pi^2}, \quad (5.10)$$

$$\tau = t - \frac{2H}{c}, \quad (5.11)$$

$$t_p = \frac{2\sqrt{2}\sigma_h}{c}, \quad (5.12)$$

$$t_s = \frac{2H}{c} \frac{1}{\frac{8\ln 2}{\theta^2} + \frac{1}{s^2}} \quad (5.13)$$

and erfc is the complementary error function. [Barrick, 1972], [Brown, 1977]. The total rough surface system response is then calculated by convolving the rough surface impulse response with the system point target response, which can be approximated as a Gaussian pulse with a 3 dB width of τ_p and a standard deviation of $\sigma_p = .425\tau_p$ [Brown, 1977]. The result is the same as equation 5.9, except t_p is now defined as

$$t_p = \sqrt{2} \sqrt{\left(\frac{2\sigma_h}{c}\right)^2 + \sigma_p^2}. \quad (5.14)$$

Figure 5.3 illustrates the wet-snow zone surface scattering model of equation 5.9 and defines the variables used in the model. The rms surface height, σ_h , and rms surface slope, s , are the two surface parameters that determine the shape of the return waveform. The set of curves in figures 5.4a and 5.4b show how a change in σ_h affects the slope of the leading edge of the return waveform while a change in s affects the slope of the trailing edge. To determine values of σ_h , s and H or

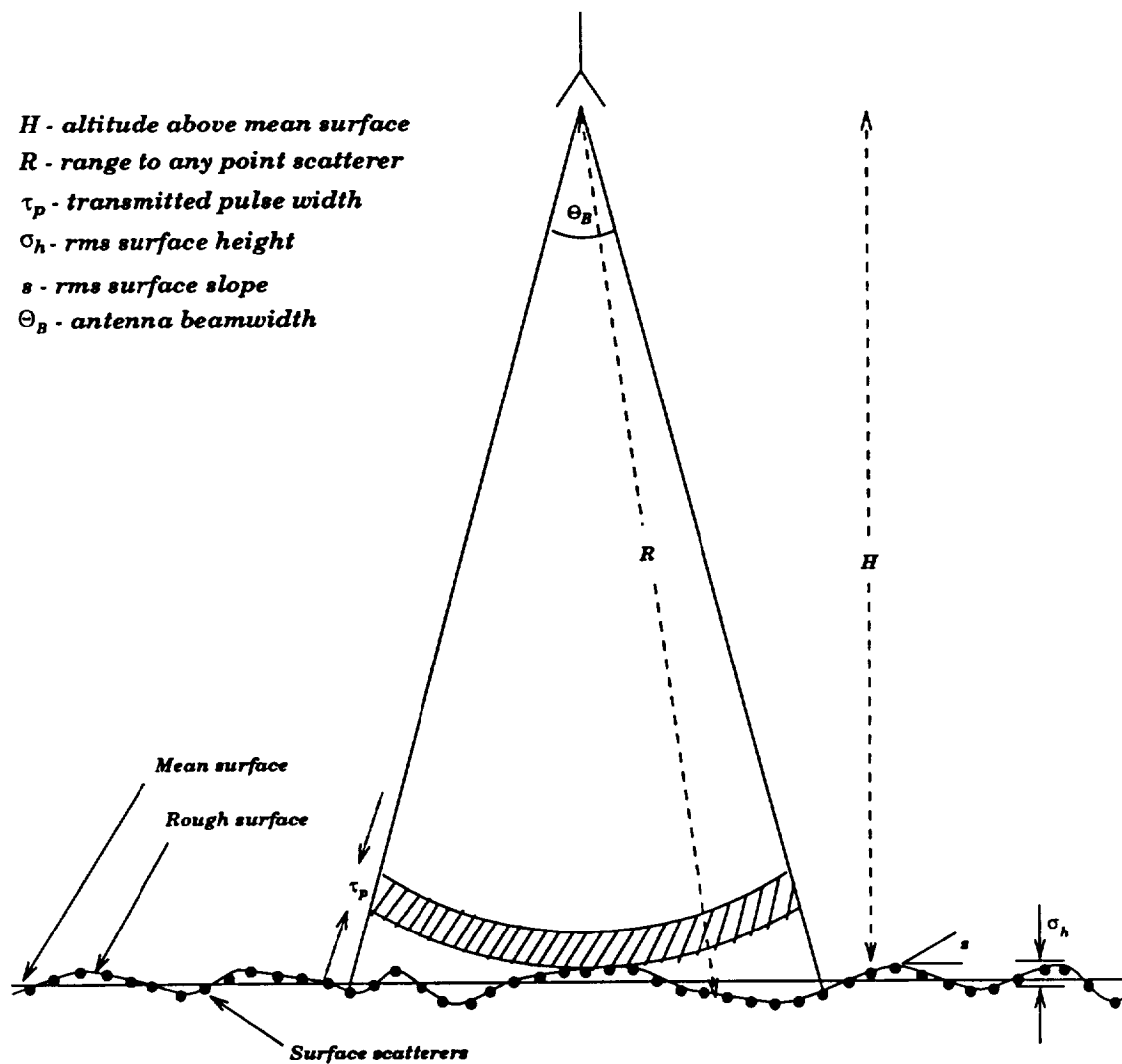
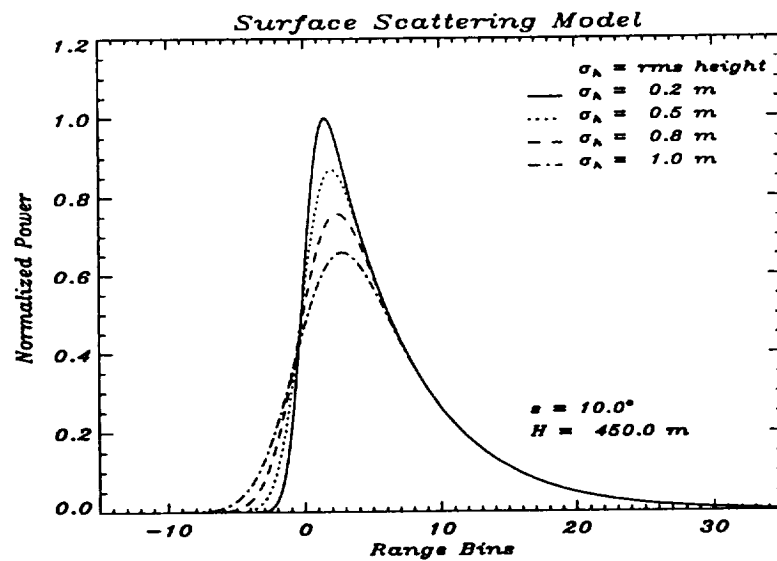
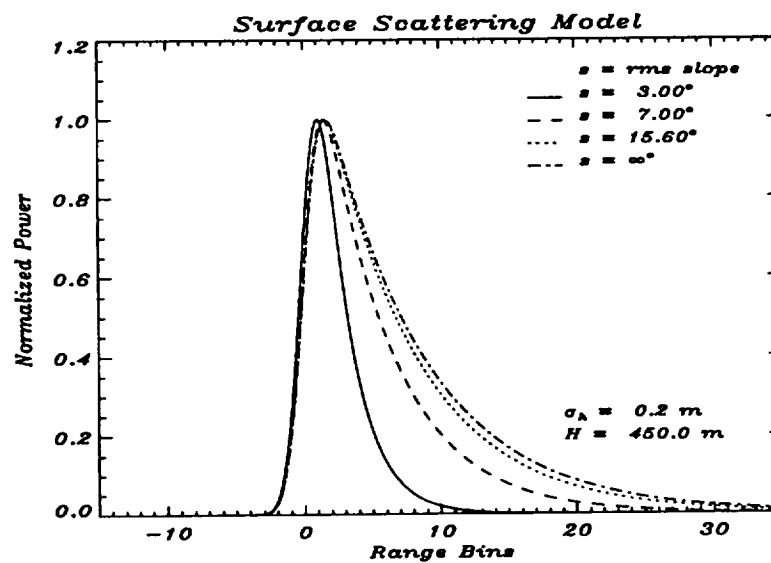


Figure 5.3. Model of surface scattering in the wet-snow zone of the Greenland ice sheet.



(a)



(b)

Figure 5.4. Surface scattering model for radar altimetry (each range bin = 2.77 nsec). (a) The effects of varying rms surface height, σ_h , on the surface scattering model and (b) the effects of varying rms surface slope, s , on the surface scattering model.

range, AAFE return waveforms are fit using the least-mean-squared error (LMSE) method [Carnahan et al., 1969], [Press et al., 1988] to a nonlinear five parameter model, which is equation 5.9 plus a parameter, a , representing the noise floor of the waveform, or

$$P_{rs}(fit)(\tau) = a + \frac{C_0}{H^3 s^2} e^{(t_p/t_s)^2} e^{-(2\tau/t_s)} \operatorname{erfc}\left(\frac{t_p}{t_s} - \frac{\tau}{t_p}\right). \quad (5.15)$$

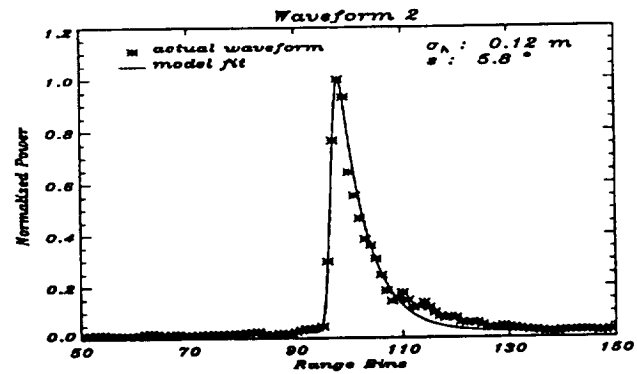
Table 5.1 lists and defines the five parameters used when fitting waveforms to the surface scattering model in equation 5.15.

Altimeter waveforms from the wet-snow zone have the same shape as the model waveforms depicted in figures 5.4a and 5.4b. When the surface scattering model is fit to waveform 2 of figure 5.1, as shown in figure 5.5a, the least-mean-squared error fit yields a σ_h of .12 meters and a s of 5.8° . In the percolation zone, however, return waveforms, such as waveforms 3 and 4 of figure 5.1, do not look like typical surface scattering returns. Waveform 4, shown in figure 5.5b along with the model fit, has a trailing edge that differs considerably from a surface scattering waveform. Although waveforms in the dry snow zone, such as waveform 6 in figure 5.1, look like surface scattering returns, fitting them to the surface scattering model, as shown in figure 5.5c, results in abnormally high values of s . It is unlikely that surface scattering is the only component contributing to the return waveform in the percolation and dry snow zones.

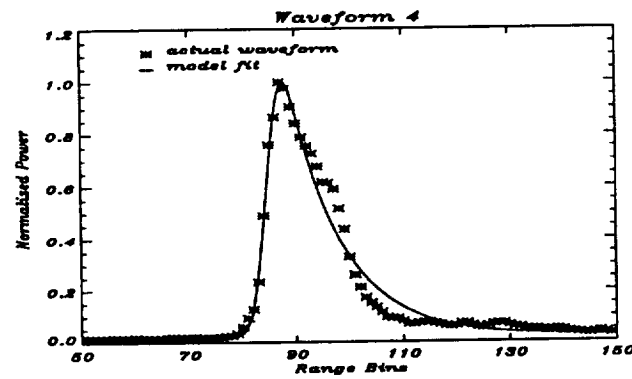
Even though the trailing edge of the waveform is sensitive to the different diagenetic zones of the ice sheet, there is always a surface component in the return due to the dielectric interface between the air and the snow pack. This return from the surface creates the sharp leading edge shown in all of the waveforms in figure 5.1. Since the rms surface height, σ_h , is determined from the leading edge of the return, it can be measured by fitting equation 5.15 to AAFE waveforms. Figure 5.6a shows the ice altitudes from a south-west to north-east pass over the ice sheet and figure 5.6b shows the corresponding rms surface height values over the flight line, where each

Table 5.1. Table of the five parameters used in the least-mean-squared error fit to the surface scattering model.

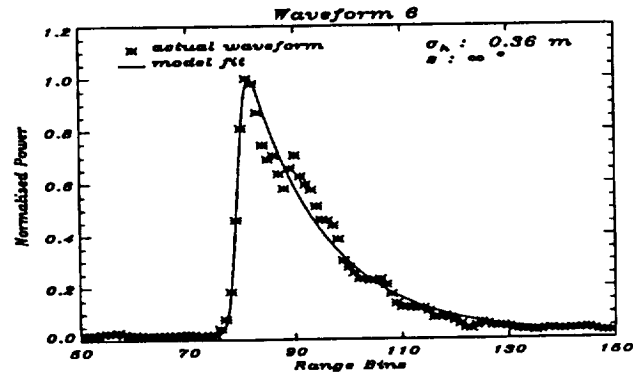
PARAMETER	VARIABLE
Range or height to mean surface	H
RMS surface height	σ_h
RMS surface slope	s
Amplitude	C_0
Noise floor	a



(a)



(b)



(c)

Figure 5.5. (a) Surface scattering model fit to waveform 2 of figure 5.1., (b) surface scattering model fit to waveform 4 of figure 5.1., and (c) surface scattering model fit to waveform 6 of figure 5.1.

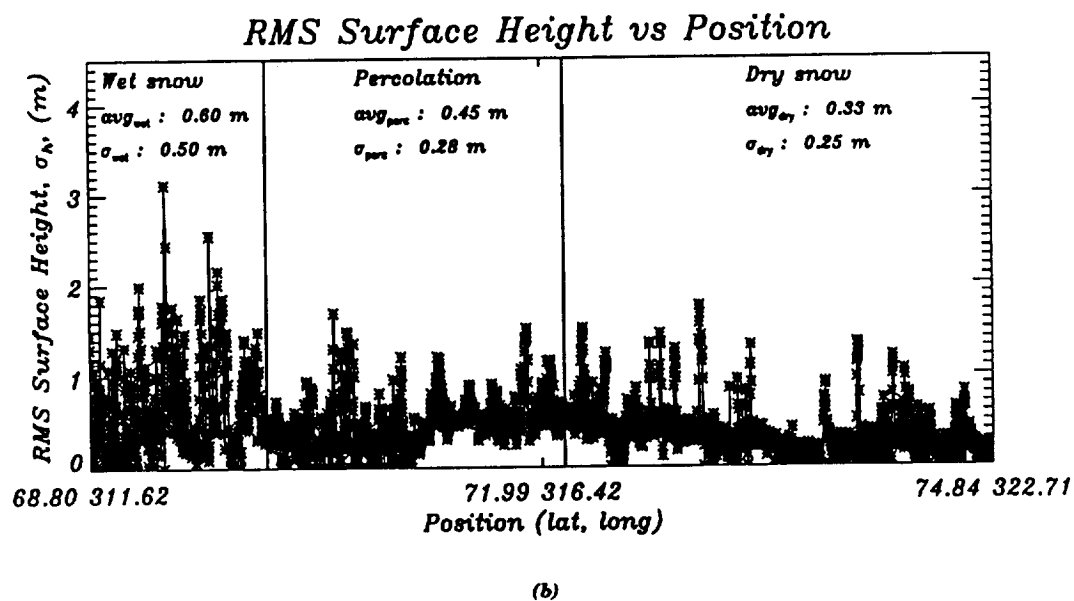
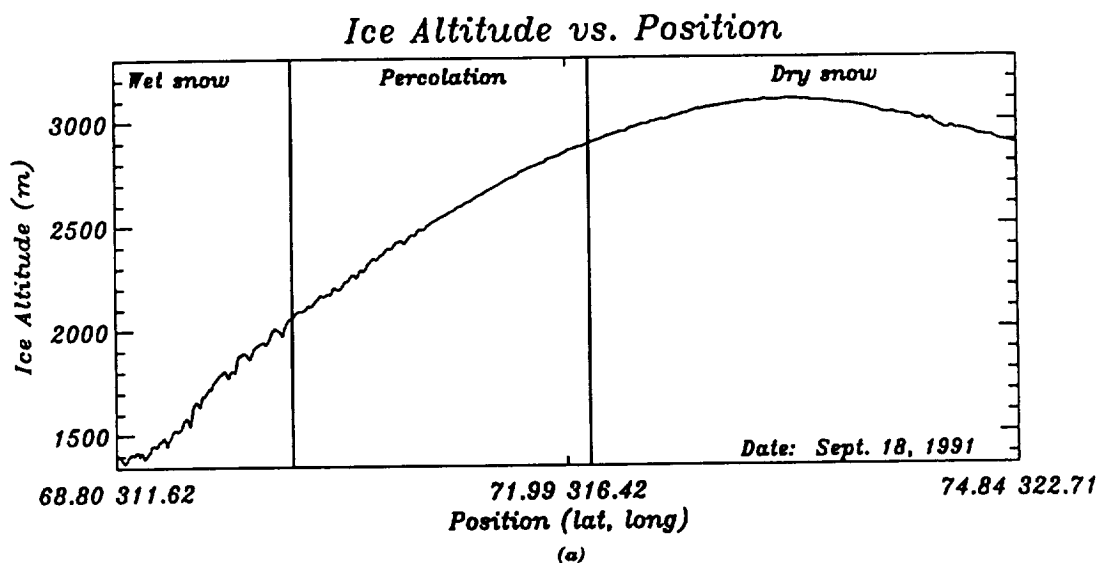


Figure 5.6. Measurements of the rms surface height over a south-west to north-east flight line. (a) The actual altitudes measured and (b) the rms surface height determined by fitting 960 averaged waveforms to the surface scattering model in equation 5.9.

measurement represents a fit to 960 averaged waveforms. The average rms surface height over this section of the ice sheet is 42 cm and the standard deviation from the mean is 33 cm. Figure 5.6b shows the mean and standard deviation of the rms surface height for each individual diagenetic region of the ice sheet. The higher values for σ_h in the wet-snow zone correspond to the greater variability in ice altitude in figure 5.6a, while the lower values in the dry-snow zone correspond to the smoother ice altitudes.

Since the trailing edge of the altimeter waveform is affected by sub-surface and volume scattering, it is not possible to determine the rms surface slope, s , by fitting return waveforms from the percolation and dry-snow zones to a surface scattering model. Returns from the wet-snow zone, however, are predominantly due to surface scattering and therefore can be used to measure s . Figure 5.7a shows the ice altitudes over a section of the wet-snow zone and figure 5.7b shows the corresponding rms surface slope values resulting from fitting equation 5.15 to AAFE return waveforms. Since a value of s that is greater or equal to 15.6 degrees represents a full antenna beam, any s greater than this is meaningless. Over this flight section the average and standard deviation of s are 9.0° and 3.6° respectively, but these slopes appear to be higher than expected, since typical ocean rms slope values range between 5° and 8° [Jackson et al., 1992]. The trailing edge of the return waveform is also affected by aircraft mispointing angle and slope-induced error, which is the error induced on the return waveform due to a sloping surface within the radar altimeter footprint [Brenner et al., 1983]. Both mispointing angle and slope-induced error cause the trailing edge of the waveform to extend out further and therefore would create a larger value of s when the waveform is fit to the surface scattering model. Since the average mispointing angle over the flight section is less than 1.2° and the more reasonable values of s correspond to the flat regions in figure 5.7a while the high values correspond to the high slope areas, it is quite probable that the high values of

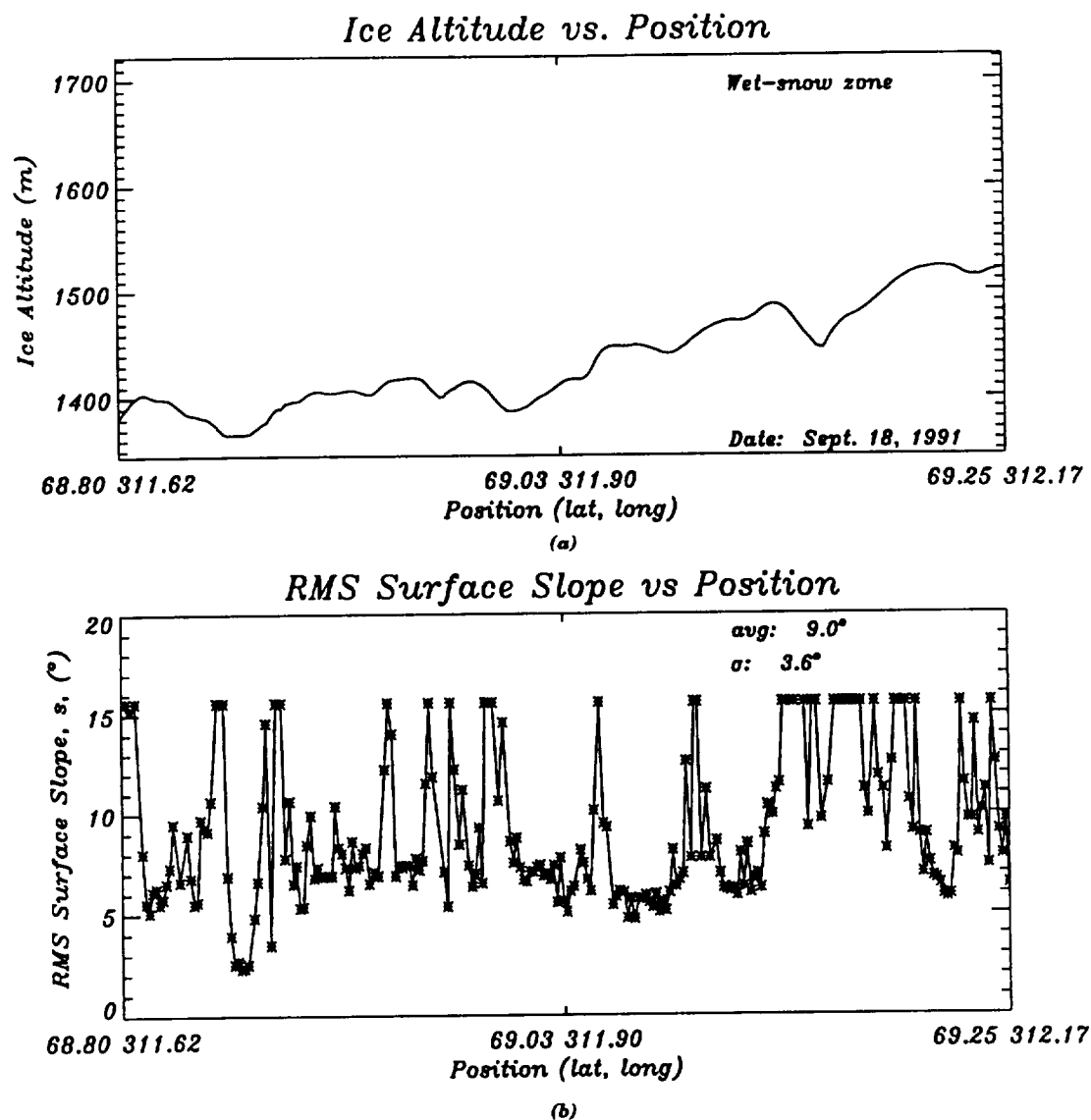


Figure 5.7. Measurements of the rms surface slope over a flight section in the wet-snow zone. (a) The actual altitudes measured and (b) the rms surface slope determined by fitting 960 averaged waveforms to the surface scattering model in equation 5.9.

s are the result of slope-induced error. For aircraft radar altimeter measurements, these errors only affect the shape of the trailing edge and therefore, if they are not exceptionally large, they do not affect the range measurement, which is taken from the leading edge.

5.1.2 Percolation Zone Model

In the percolation zone, where there is some summer melting, liquid water percolates down into the sub-surface snow and refreezes into ice layers, ice pipes and ice lenses. Stratigraphy studies reveal that these ice structures can be located anywhere between .1 meters and 5 meters below the ice sheet surface [Benson, 1962]. Figure 5.8 illustrates the sub-surface stratigraphy in the percolation zone. Since this zone is a transition region between the wet-snow and dry-snow zones, the liquid water content may vary from 3% near the border of the wet-snow zone to 0% near the dry-snow zone. Similarly, the density of the snow may range from .5 to .3 g/cm³. Such a large change in the snow properties results in a vast range of attenuation coefficients and depths of penetration in this region.

The numerous odd-shaped sub-surface structures in the percolation zone as well as the range of penetration depths, make it more difficult to model than the wet-snow zone. As the six altimeter return waveforms in figure 5.9 show, the sub-surface ice features in the percolation zone are affecting the waveform shape. Since the ice lenses, pipes and layers are usually greater than 10 cm in diameter and are large relative to the 2.16 cm altimeter wavelength, the resulting scatter from these ice structures is in the optical regime or the geometric optics limit [Ulaby et al., 1981]. Therefore, the return from the ice features dominates any scattering from the surrounding snow and the percolation zone can be modelled as large volume scatterers in a constant dielectric medium. As a result, the radar altimeter return

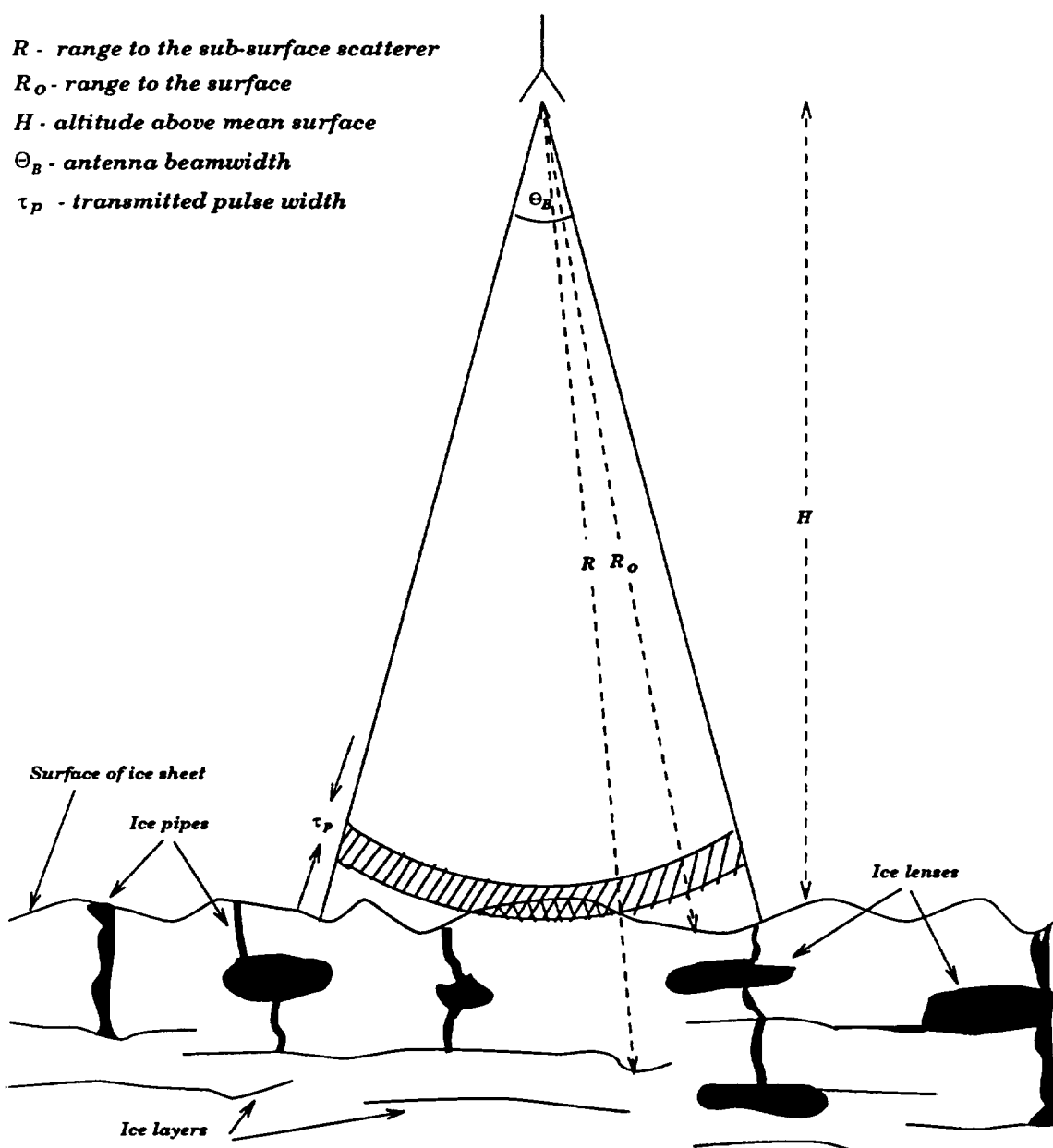


Figure 5.8. Model of sub-surface scattering in the percolation zone of the Greenland ice sheet.

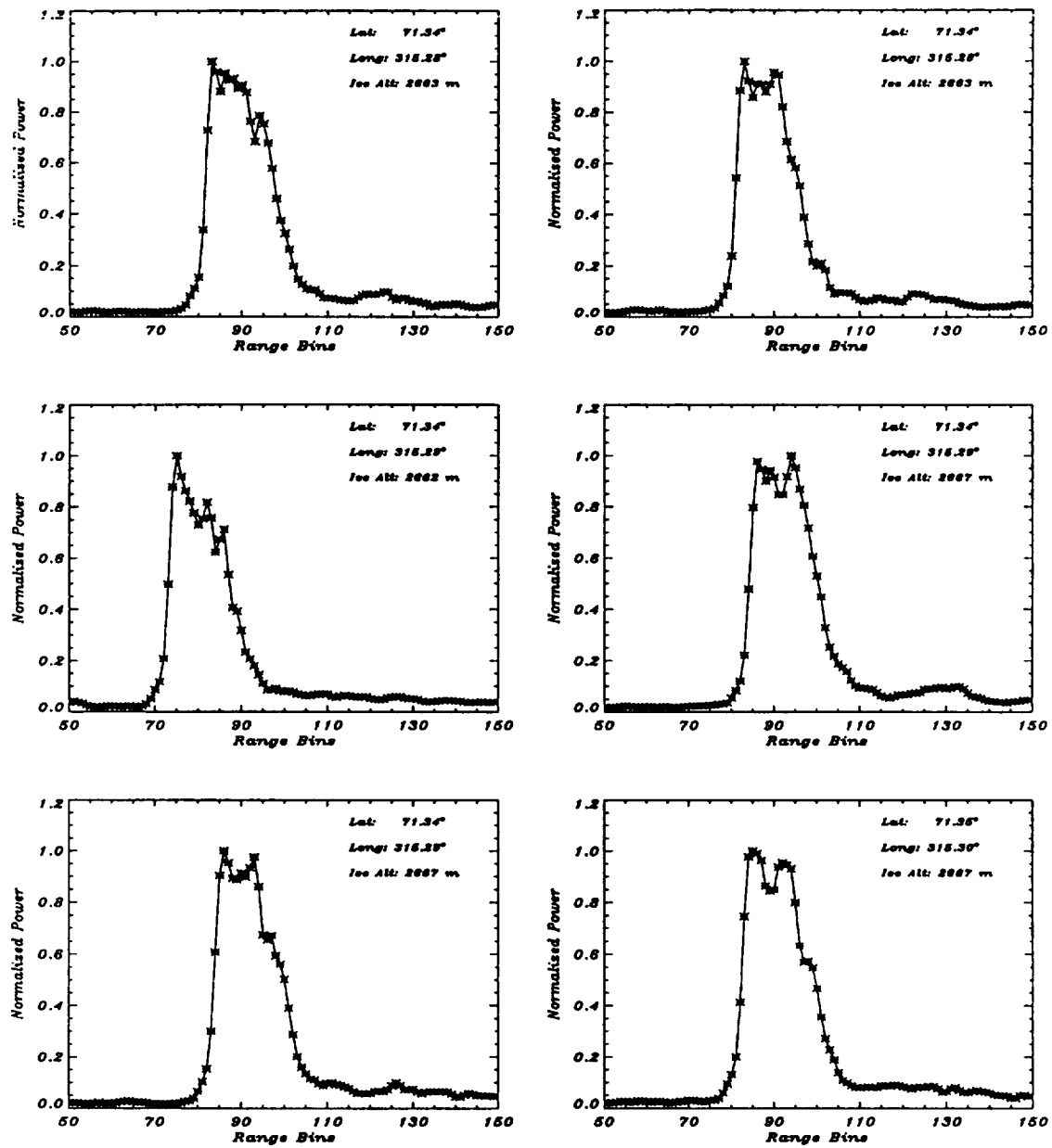


Figure 5.9. Six sample altimeter return waveforms from the central part of the percolation zone of Greenland.

is calculated using the volume scattering radar range equation [Swift et al., 1985], which is

$$P_{rv}(t) = \frac{P_t \lambda^2 T^2}{(4\pi)^3} \int_{illum vol} \frac{\delta(t - 2(\frac{R_o}{c} + \frac{R-R_o}{c_s})) G^2(\theta)}{R^4} e^{-2\kappa_e(R-R_o)} \eta_v dV \quad (5.16)$$

where the antenna gain $G(\theta)$ is defined in equation 5.6, T is the power transmission coefficient, R_o is the distance from the radar to the surface, R is a variable representing the range to the sub-surface scatterers and $c_s = \frac{c}{\sqrt{\epsilon_s}}$ is the velocity of propagation in the snow. This analysis is carried out in cylindrical coordinates and therefore $dV = \rho d\rho d\phi dh$ where h is the depth below the surface. The extinction coefficient, κ_e , is defined as the sum of the power absorption coefficient, κ_a , and the power scattering coefficient, κ_s , or $\kappa_e = \kappa_a + \kappa_s$. Since the scattering losses in snow are negligible relative to the absorption losses at frequencies below 15 GHz [Hallikainen et al., 1986], [Stiles and Ulaby, 1981], κ_e for the percolation zone is

$$\kappa_e = \kappa_a = 2\alpha \quad (5.17)$$

where α is the attenuation coefficient of the snow. Thus, the exponential component in equation 5.16 represents the two-way power attenuation in the lossy dielectric media.

The volume backscatter coefficient, η_v , in equation 5.16 is due to the ice lenses, pipes and layers and is defined as the product of σ_B , the backscatter cross section per particle and n , the density per unit volume, or

$$\eta_v = n\sigma_B \quad (5.18)$$

[Swift et al., 1985]. In the percolation zone, however, the ice features are not distributed evenly with depth and may be larger at certain depths. Therefore,

$$n = n(\rho, \phi, h) = n(\rho, h) \quad (5.19)$$

$$\sigma_B = \sigma_B(\rho, \phi, h) = \sigma_B(\rho, h) \quad (5.20)$$

assuming independence of ϕ . For a first order approximation, a uniform distribution over ρ is assumed resulting in $n(h)$ and $\sigma_B(h)$.

Substituting these results into equation 5.16 and performing the integral gives

$$\begin{aligned} P_{rv}(\tau) &= C_1 e^{\frac{-8\ln 2}{\sigma_B^2} \frac{c}{H} \tau} \int_{t=0}^{\tau} e^{\frac{8\ln 2}{\sigma_B^2} \frac{c}{H} t} e^{-2\alpha c_s t} n\left(\frac{c_s t}{2}\right) \sigma_B\left(\frac{c_s t}{2}\right) dt & \tau > 0 \\ P_{rv}(\tau) &= 0 & \tau < 0 \end{aligned} \quad (5.21)$$

where C_1 and τ are defined as

$$C_1 = \frac{P_t \lambda^2 T^2 G_o^2}{32\pi^2 H^3} \quad (5.22)$$

$$\tau = t - \frac{2H}{c} . \quad (5.23)$$

In the percolation zone, the surface backscatter component of the altimeter return waveform is due to the air-snow boundary, while the volume backscatter component is due to the optical volume scattering in the sub-surface snow. As a result, the total return power, $P_r(\tau)$, is the incoherent sum of these two components,

$$P_r(\tau) = A P_{rs}(\tau) + B P_{rv}(\tau) \quad (5.24)$$

where A and B are the percentages of surface and volume return power respectively.

To determine the volume scattering component of the radar return, it is important to know the distribution of n and σ_B versus depth. Unfortunately, there is limited documentation on these parameters due to the difficulty in obtaining the measurements. Thus, in the 1993 Greenland ground truth experiment at Dye 2, a sample distribution of ice layers, lenses and pipes was obtained. A 5 x 3 meter area of the ice sheet was probed at 10 cm increments using a marked steel rod and pressing it into the snow pack until it hit ice. The raw data from this experiment are shown in figure 5.10. To validate this probing experiment, a pit was dug alongside the 5 x 3 meter area and each 10 cm vertical wall was documented for size and location of ice features. Figure 5.11 shows an example of the results from wall #1.

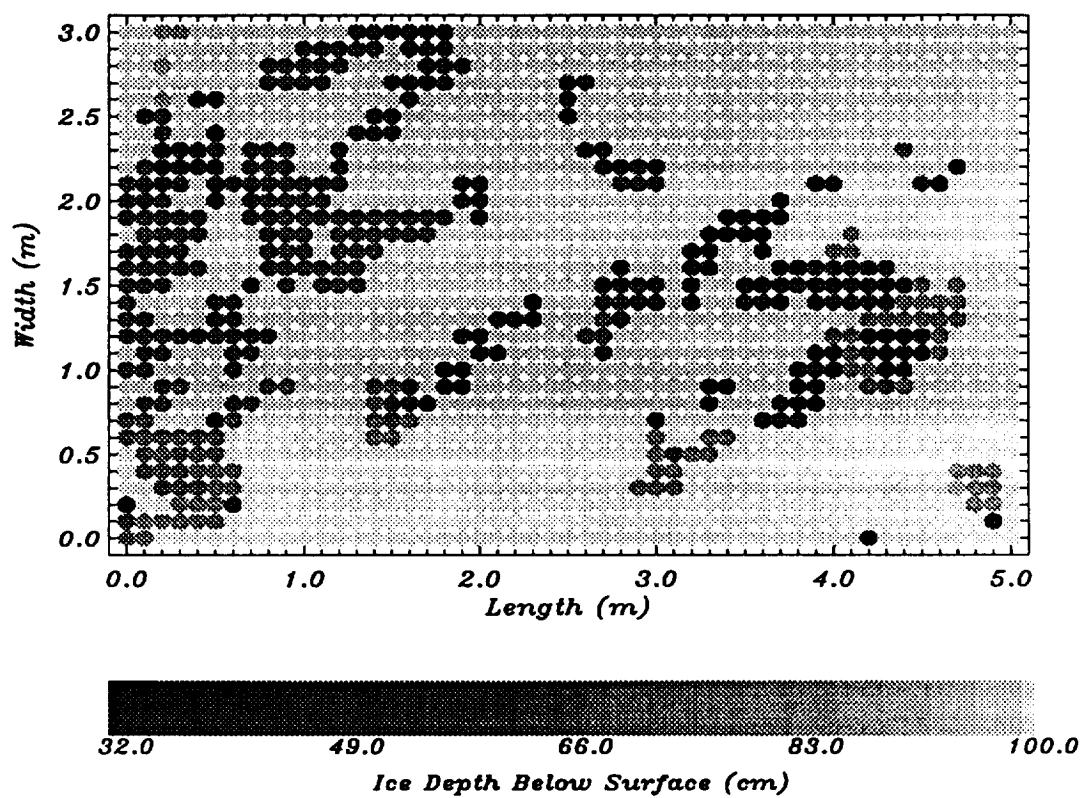


Figure 5.10. A sample distribution of the ice features in a 5 x 3 meter area of the Greenland ice sheet at Dye 2. Each measurement represents the depth that the steel rod hit ice.

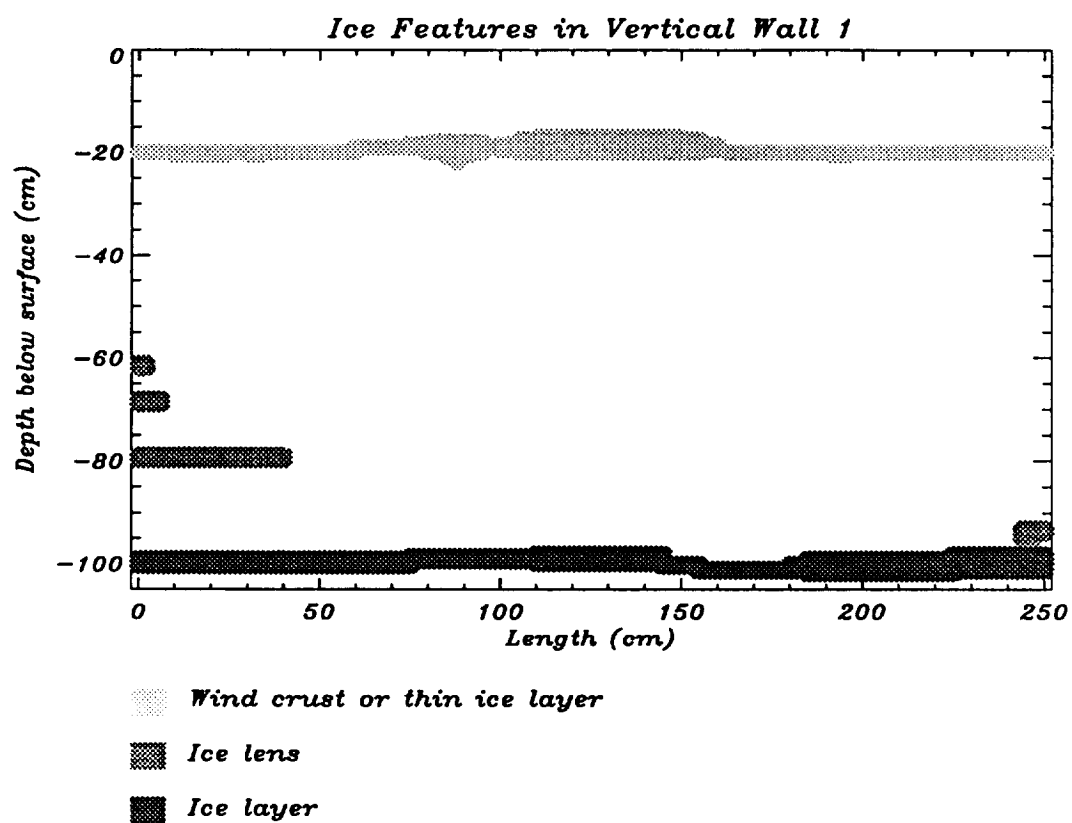


Figure 5.11. The ice features in vertical wall # 1 of the 5 x 3 meter pit. The features shown were located from 0 to 2.5 meters along the 5 meter length of the wall.

As both figures 5.10 and 5.11 show, there was a continuous ice layer at a depth of 1 meter and the thickness of this layer fluctuated between 1 and 3 cm. Other sample pits dug several hundred meters away from this pit also had an ice layer at a depth of 1 meter. This layer may have been the surface from a previous summer and it shows that some ice layers in the percolation zone may extend over very large areas. The results from this probing experiment were used to create the sample distribution of $n(h)$ shown in figure 5.12. It is clear from this sample that the ice features do not have a standard distribution. In this particular case, they tended to be located between 37 and 42 cm, between 46 and 49 cm, between 59 and 61 cm, between 65 and 70 cm and between 78 and 81 cm. The ice layer at 1 meter is not included in this distribution.

Determining the backscatter coefficient σ_B is as difficult as calculating $n(h)$. Figures 5.13 and 5.14 are pictures of an ice pipe and an ice lens respectively, taken during the 1993 experiment. Since the AAFE altimeter is nadir-viewing, these ice features would be viewed by the instrument from their top surface. In the optical regime, a target with gradual curving surfaces and an arbitrary shape has a backscatter coefficient of

$$\sigma_B = \pi a_1 a_2 |r(0)| \quad (5.25)$$

where $r(0)$ is the reflection coefficient at normal incidence and a_1 and a_2 are the radii of curvature in the two planes of observation [Swift et al., 1985]. Density measurements of the ice features taken during the 1993 experiment were between .86 and .91 g/cm³. Since this is very close to the density of pure ice, which is .916 g/cm³, the dielectric constant of pure ice, ϵ_i , may be used to calculate $r(0)$ or

$$r(0) = \frac{\sqrt{\epsilon_i} - \sqrt{\epsilon_s}}{\sqrt{\epsilon_i} + \sqrt{\epsilon_s}}. \quad (5.26)$$

Ground truth measurements of snow density and water content were used along with the Debye-like model in equation 5.1 to approximate the dielectric constant of

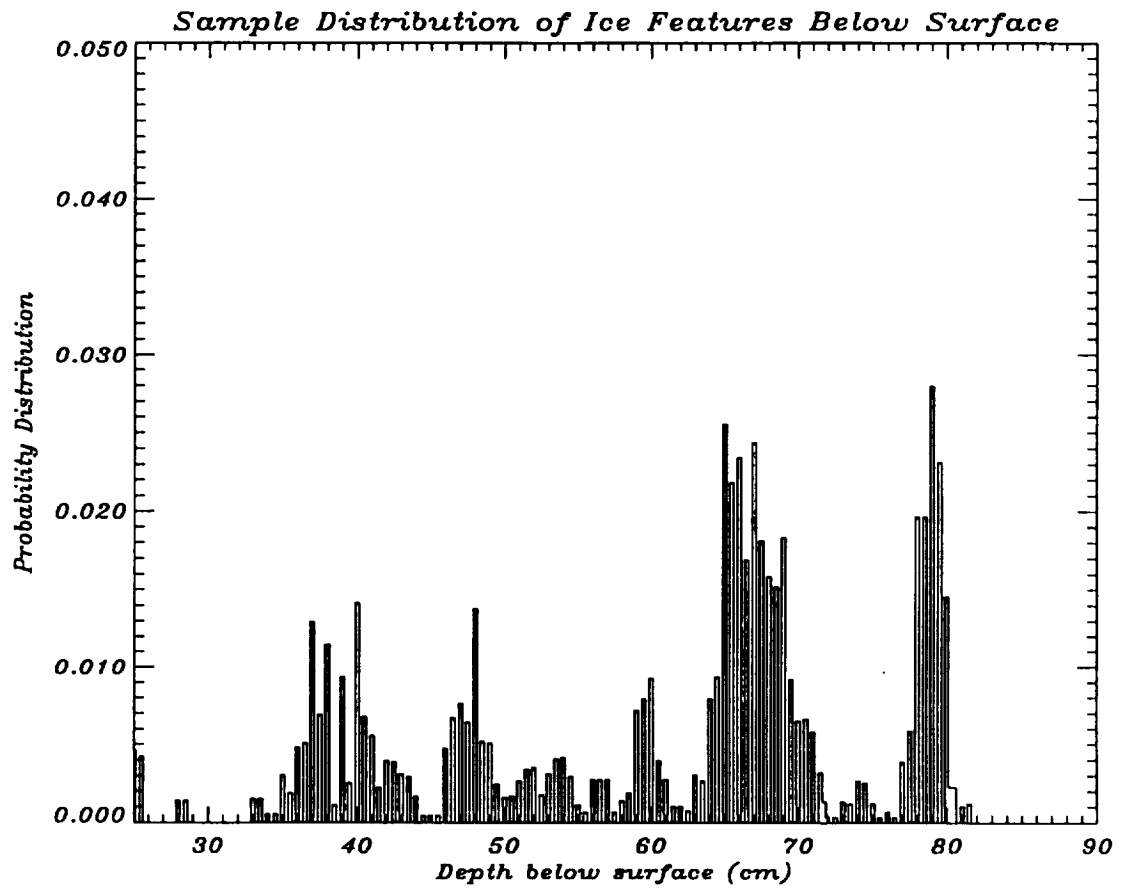


Figure 5.12. A sample distribution of the location of ice features below the surface or $n(h)$ in the Greenland snow pack at Dye 2.



Figure 5.13. Picture of an ice pipe taken during the 1993 Greenland ground truth experiment at Dye 2.

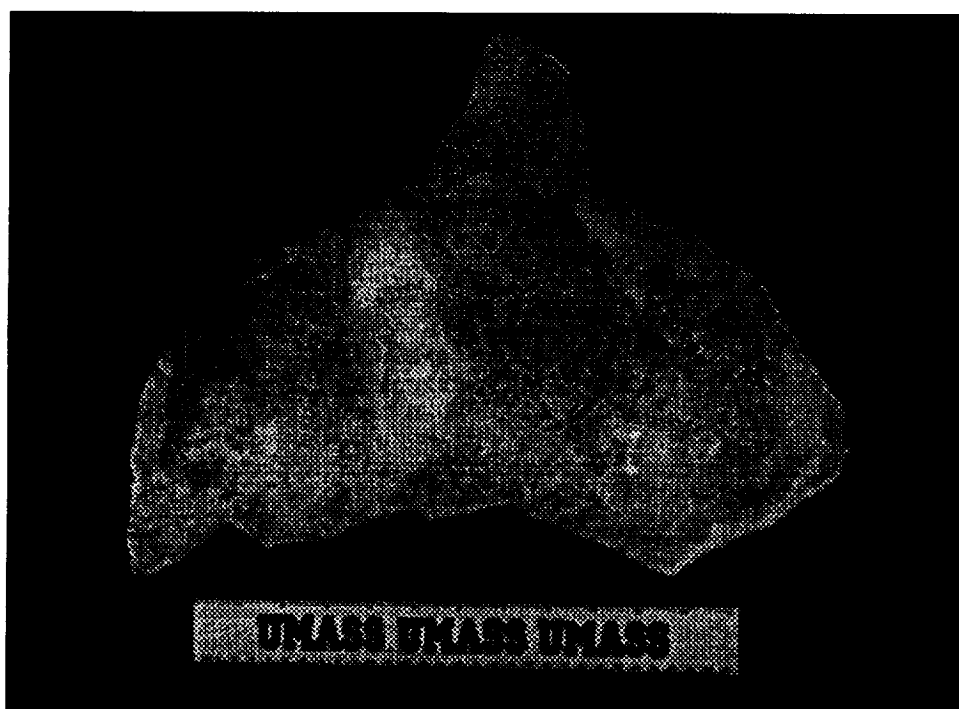


Figure 5.14. Picture of an ice lens taken during the 1993 Greenland ground truth experiment at Dye 2.

the surrounding snow, ϵ_s , which ranged from $1.76 + j.001$ to $1.83 + j.05$ and resulted in a $r(0)$ between $.13 - j.006$ and $.17 - j.008$.

Ice pipes in the percolation zone are typically 4 to 7 cm in diameter and their size is independent of depth in the first meter of the snow pack. In addition, since they are viewed by the radar altimeter from their top surface, they appear to be circular. Therefore, the average backscatter cross section of an ice pipe in the percolation zone is $\sigma_{B \text{ ice pipe}}(h) = \sigma_{B \text{ ice pipe}} \approx -28$ dB. The ice lenses, on the other hand, are larger at greater depths, as shown in figure 5.11. Lenses within 60 cm of the surface are typically 10 to 20 cm in diameter, while those closer to 80 cm are often 50 to 60 cm in diameter. The resulting average backscatter cross section for such ice lenses is $\sigma_{B \text{ ice lens}}(h = 60 \text{ cm}) \approx -20$ dB and $\sigma_{B \text{ ice lens}}(h = 80 \text{ cm}) \approx -8$ dB. Finally, a continuous ice layer, such as the one throughout the Dye 2 area located at 1 meter, is larger than the area of the AAFE footprint and therefore its backscatter cross section is limited by the footprint area to $\sigma_{B \text{ ice layer}}(h = 1 \text{ m}) \approx 20$ dB. Since the ice feature with the largest contributing backscatter cross section in the percolation zone is the continuous ice layer, it is the dominant scatterer, but the ice lenses and pipes are closer to the surface and the incoming signal is not attenuated as much before it interacts with them.

Although these ground truth data give an idea of the size and distribution of ice features, they represent only one sample in the percolation zone, which covers a large area of the ice sheet. These results can be inserted into equation 5.21, however, to get an idea of their effects on the return waveform. For example, figure 5.15a shows a model optical volume scattering return created using equation 5.21, the sample distribution of $n(h)$ in figure 5.12 along with the ice layer at one meter and the ground truth values of σ_B . To get the total return power, P_r , in equation 5.24, this optical volume scattering model is combined with a model surface return having

typical values of .20 m and 8° for σ_h and s , resulting in the final model percolation zone waveform in figure 5.15b.

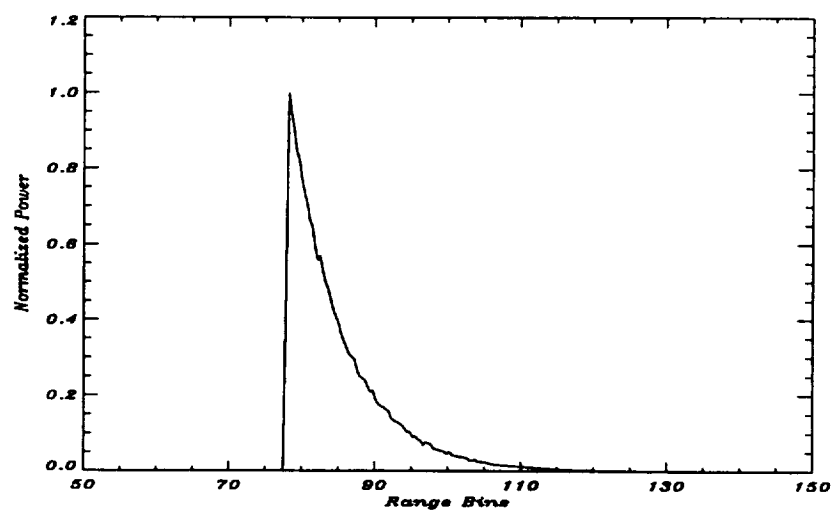
As expected, the ice layer has the largest effect on the waveform, creating the second peak at one meter from the surface. Figures 5.16a and 5.16b are actual AAFE return waveforms obtained from the Dye 2 area during the 1993 ground truth experiment. These waveforms exhibit a second peak similar to that in the model waveform in figure 5.15b.

Both the model and actual waveforms agree with results from the ground-based Ku-band FMCW radar operated at Dye 2 during the 1993 ground truth experiment. Nadir results for this radar show a significant return from the surface and from the ice layer at one meter and much smaller returns from the ice lenses and pipes [Zabel, 1993], [Zabel et al., 1994]. Therefore, when a continuous ice layer is present in the percolation zone, it is the dominant scatterer and has the greatest effect on the AAFE return waveform.

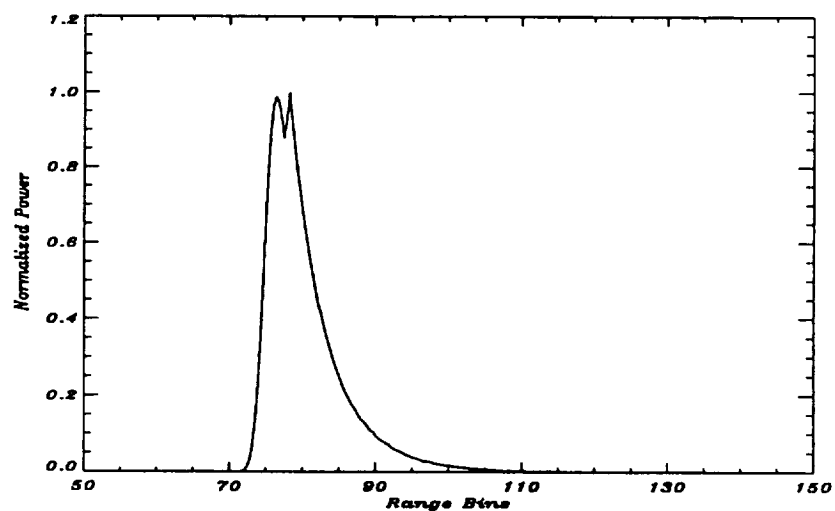
Although this model agrees with some of the altimeter returns from the percolation zone, it does not explain other more complex waveforms such as those in figure 5.9. Since both $n(h)$ and $\sigma_B(h)$ play an important role in the return waveform and both may vary significantly through the percolation zone, it is difficult to invert the relationship in equation 5.21 and determine $n(h)$ and $\sigma_B(h)$ from an actual waveform. Equation 5.21 does, however, show the relationship between the return and $n(h)$ and $\sigma_B(h)$, and allow sample distributions to be inserted and manipulated to illustrate the effect on the return waveform.

5.1.3 Dry-snow Zone Model

In the dry snow zone, where there is never summer melting, the density of the snow is low and the liquid water content is 0%. Measured values of snow density, which lie between .28 and .38 g/cm³ [Benson, 1962], result in attenuation coefficients

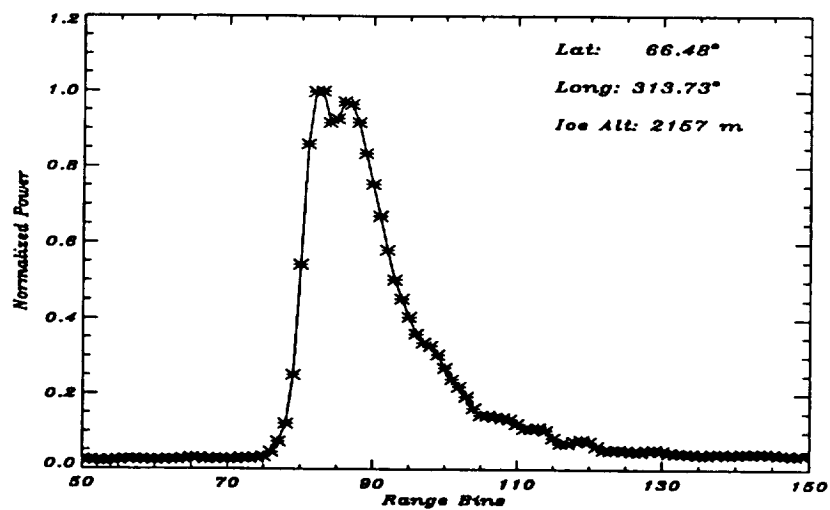


(a)

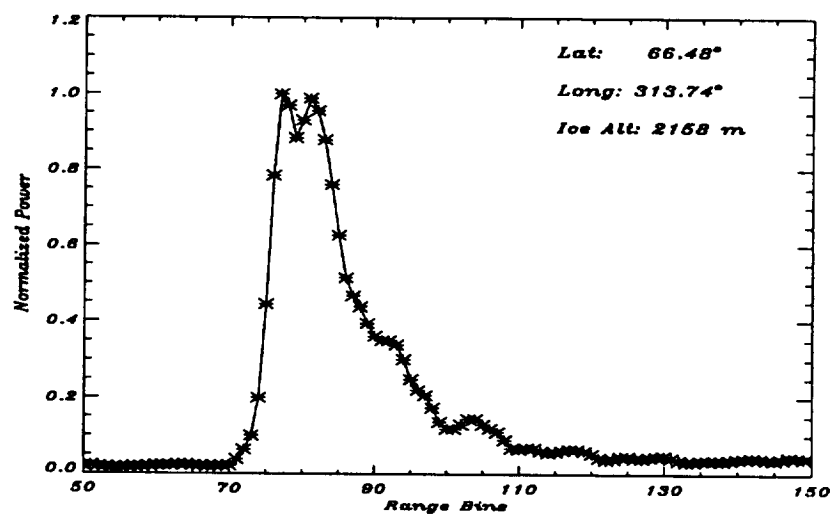


(b)

Figure 5.15. Altimeter model returns from the percolation zone. (a) The volume scattering component of the return and (b) the sum of the surface and volume scattering returns.



(a)



(b)

Figure 5.16. Actual AAFE Altimeter return waveforms from the percolation zone obtained while the aircraft flew over the Dye 2 camp site.

that are less than .1 Np/m or 1 dB/m and depths of penetration greater than 5 meters. Such a low attenuation coefficient suggests that a significant component of the return waveform is due to volume scattering from the sub-surface snow.

The scattering due to the sub-surface volume, $P_{rv}(t)$, is again calculated using the volume scattering radar range equation [Swift et al., 1985]

$$P_{rv}(t) = \frac{P_t \lambda^2 T^2}{(4\pi)^3} \int_{illum vol} \frac{\delta(t - 2(\frac{R_o}{c} + \frac{R-R_o}{c_s})G^2(\theta))}{R^4} e^{-4\alpha(R-R_o)} \eta_v dV . \quad (5.27)$$

The individual snow grains, which are less than .5 mm in this region, are small relative to the 2.16 cm wavelength of the altimeter. Therefore, the volume scattering is primarily due to Rayleigh scattering [Ulaby et al., 1981]. As a result, the volume backscatter coefficient, η_v , is

$$\eta_v = n \sigma_B \quad (5.28)$$

where σ_B is the Rayleigh backscatter cross section per particle and n is the density per unit volume. In the dry-snow zone, the density of the snow pack and the size of the snow grains is fairly constant in the upper several meters [Ling, 1985] resulting in an σ_B and n that are constant with position. Figure 5.17 illustrates this volume scattering model and defines the parameters used in the model. The resulting return power due to the Rayleigh volume scattering is

$$\begin{aligned} P_{rv}(\tau) &= C_2 \frac{1}{\beta c - 2\alpha c_s} (e^{-2\alpha c_s \tau} - e^{-\beta c \tau}) & \tau > 0 \\ P_{rv}(\tau) &= 0 & \tau < 0 \end{aligned} \quad (5.29)$$

where

$$C_2 = \frac{P_t \sqrt{2} \lambda^2 T^2 G_o^2 \eta_v}{32 \pi^2 H^3} , \quad (5.30)$$

$$\beta = \frac{8 \ln 2}{H \theta_B^2} , \quad (5.31)$$

$$\tau = t - \frac{2H}{c} \quad (5.32)$$

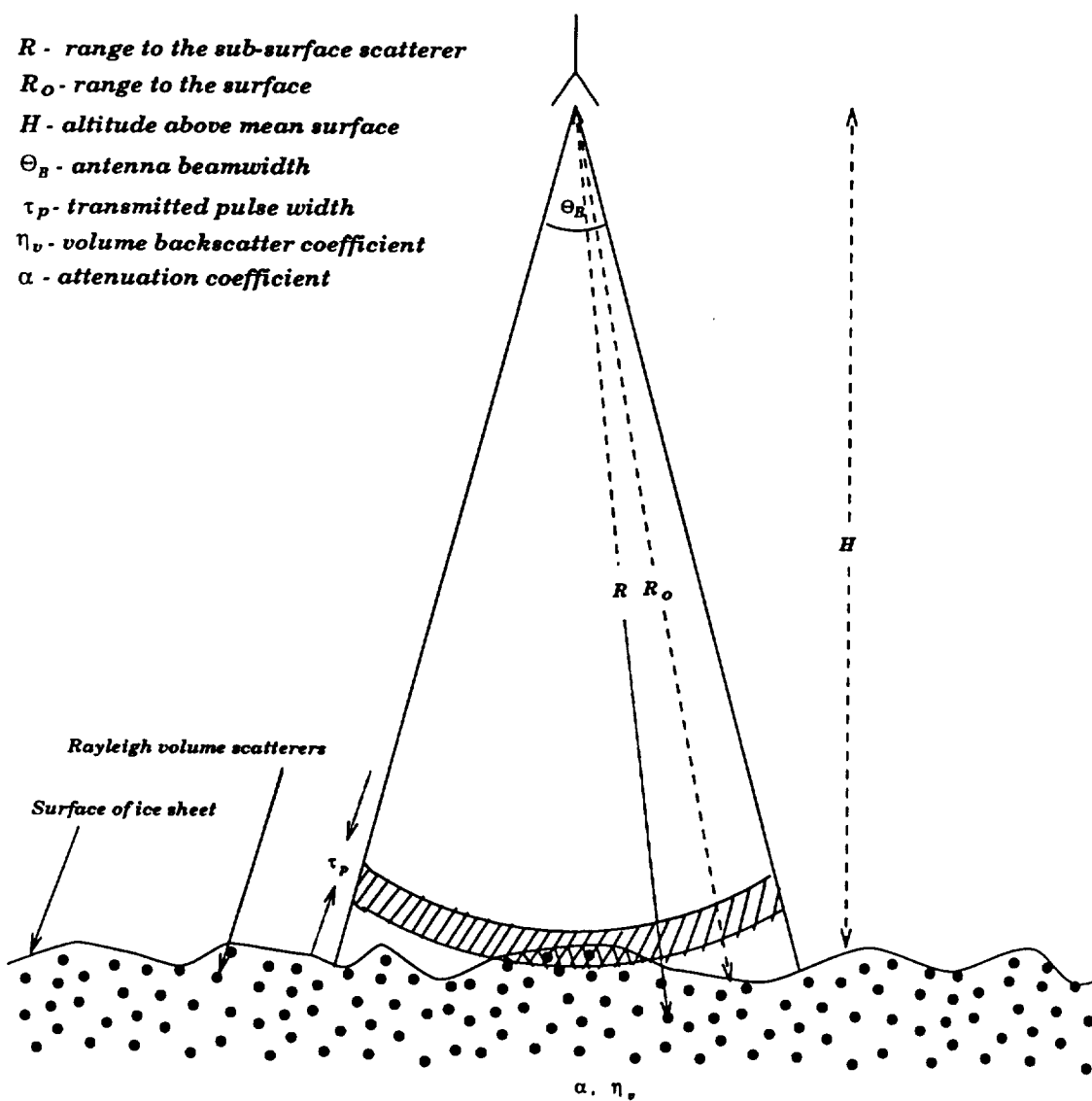


Figure 5.17. Model of Rayleigh volume scattering in the dry-snow zone of the Greenland ice sheet.

and

$$c_s = \frac{c}{\sqrt{\epsilon_s}}. \quad (5.33)$$

Equation 5.29 was obtained by performing the integral in equation 5.27 in cylindrical coordinates. Davis [Davis, 1993] obtained the same results by performing the analysis in spherical coordinates. Figure 5.18 shows how varying the attenuation coefficient, α , of the sub-surface snow affects the shape of the volume scattering return. As α approaches infinity, the depth of penetration goes to zero and, as expected, the volume scattering return goes to zero. On the other hand, as α goes to zero, the depth of penetration approaches infinity and $P_{rv}(\tau)$ becomes a function of the antenna beamwidth.

As in the percolation zone, the total return power, $P_r(\tau)$, is the incoherent sum of the surface and volume backscatter components. The series of waveforms in figure 5.19 illustrates the effect of varying the attenuation coefficient on the total return power. This is done by changing the snow density and liquid water content using equations 5.1 and 5.2. The first two waveforms show that a liquid water content of 3% and even 1% results in return waveforms that are predominantly surface scattering. The effects of sub-surface scattering do not appear until the third waveform, where the liquid water content is approaching 0%. The following waveforms illustrate the effect of keeping the liquid water content at zero and reducing the snow density from .40 g/cm³ to .27 g/cm³.

Values of the attenuation coefficient in the dry-snow zone are determined using a LMSE fit to a nonlinear seven parameter model, which is the sum of equation 5.24 and a noise floor parameter or

$$P_{r(fit)}(\tau) = a + A P_{rs}(\tau) + B P_{rv}(\tau). \quad (5.34)$$

The seven parameters used when fitting to equation 5.34 are listed in table 5.2. This combined surface and Rayleigh volume scattering model explains a return

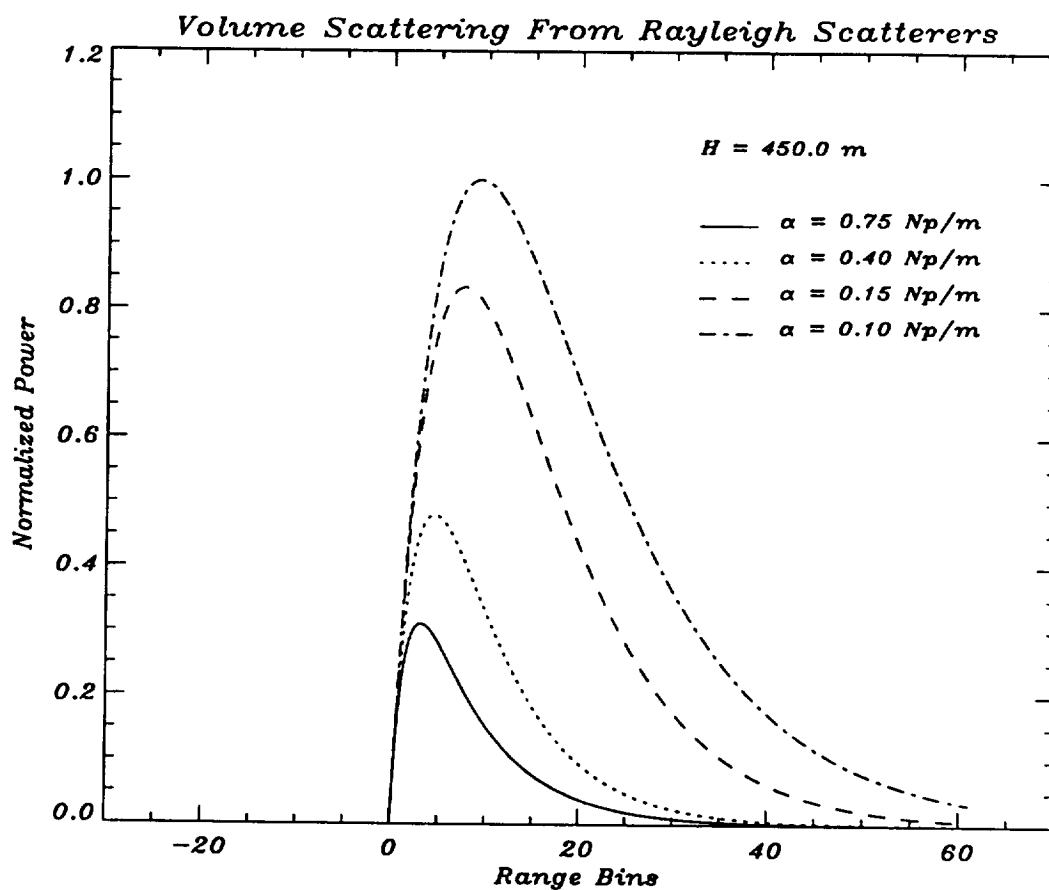


Figure 5.18. Effects of varying attenuation, α , on the Rayleigh volume scattering model of the dry-snow zone of Greenland.

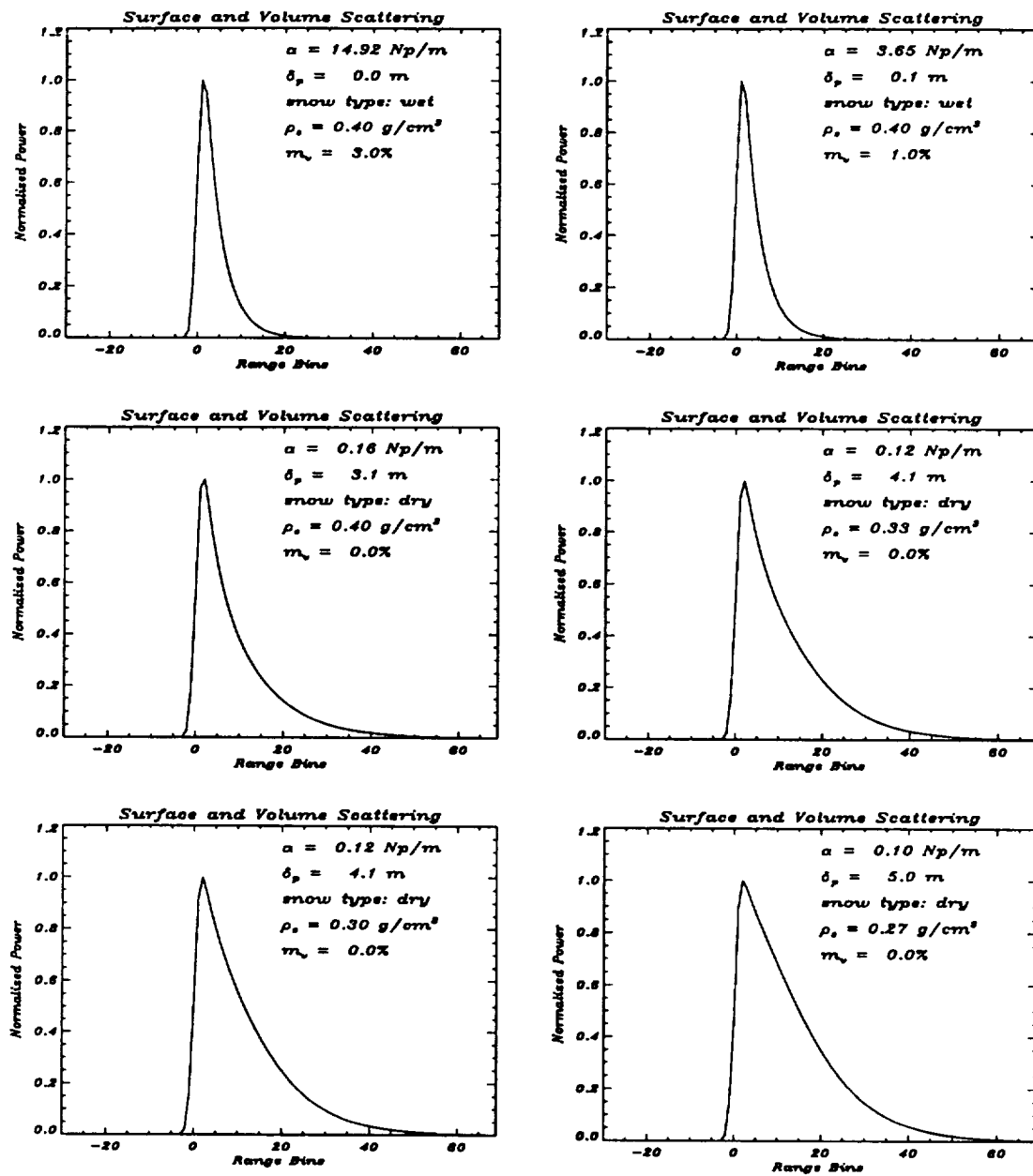


Figure 5.19. Combined surface and Rayleigh volume scattering model for varying values of snow density, ρ_s , and liquid water content, m_v .

Table 5.2. Table of the seven parameters used in the LMSE fit to the combined surface and Rayleigh volume scattering model.

PARAMETER	VARIABLE
Attenuation coefficient	α
Range or height to mean surface	H
RMS surface height	σ_h
RMS surface slope	s
Amplitude of the surface scattering component	A
Amplitude of the Rayleigh volume scattering component	B
Noise floor	a

waveform such as waveform 6 in figure 5.1, which has a sharp leading edge and a long gently sloping trailing edge. As figure 5.20 shows, the combined model fit to waveform 6 yields $\sigma_h = .42$ m, $s = 2.6^\circ$, $\alpha = .1$ Np/m and $\delta_p = 5.0$ m, which are reasonable surface and sub-surface parameters for the dry-snow zone. Using the attenuation coefficient, α , and assuming the snow is dry and has $m_v = 0\%$ results in an approximate snow density of $\rho_s = .29$ g/cm³. Figure 5.21a shows attenuation coefficients from a section of the dry-snow zone obtained by fitting the combined model in equation 5.34 to AAFE return waveforms. The average α is .11 Np/m or 1 dB/m, which is equivalent to an approximate snow density of $\rho_s = .28$ g/cm³. Davis and Zwally [Davis and Zwally, 1993] fit a similar combined surface and volume scattering model to SEASAT radar altimeter waveforms and obtained values between .1 and .15 Np/m in the dry-snow zone at 72° N, which was the upper extent of the SEASAT satellite coverage. Since both α and s in the combined model affect the waveform trailing edge, unreasonable parameter values are occasionally obtained during the LMSE fit, such as the points above .3 Np/m and at 0 Np/m in figure 5.21a.

Figures 5.21b and 5.21c show values of σ_h and s from the same fit to equation 5.34. The values of σ_h are similar to those shown in figure 5.6b over this same flight section, which were obtained when the waveforms were fit to the surface scattering model of equation 5.15. This shows that although Rayleigh volume scattering affects returns from the dry-snow zone, a surface scattering model can be used for rms surface height measurements, since the leading edge of the waveform is always due to a surface return. Values of s , on the other hand, cannot be obtained using the surface scattering model in the dry-snow zone. The combined model, however, allows part of the trailing edge to be attributed to s and part to α , resulting in reasonable values of rms surface slope, such as those shown in figure 5.21c.

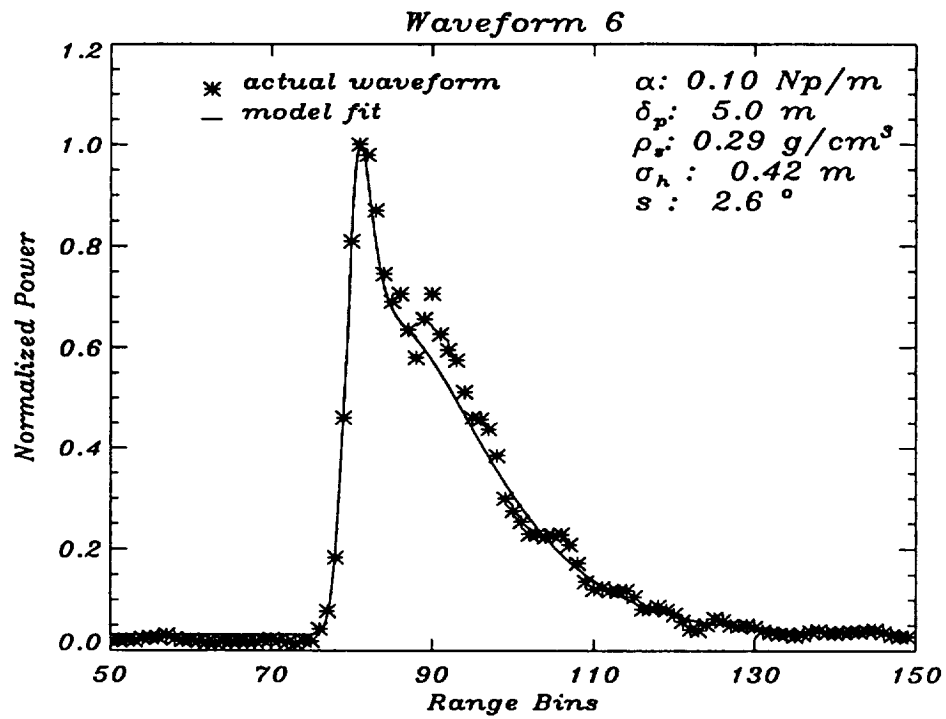


Figure 5.20. Combined surface and Rayleigh volume scattering model fit to waveform 6 of figure 5.1.

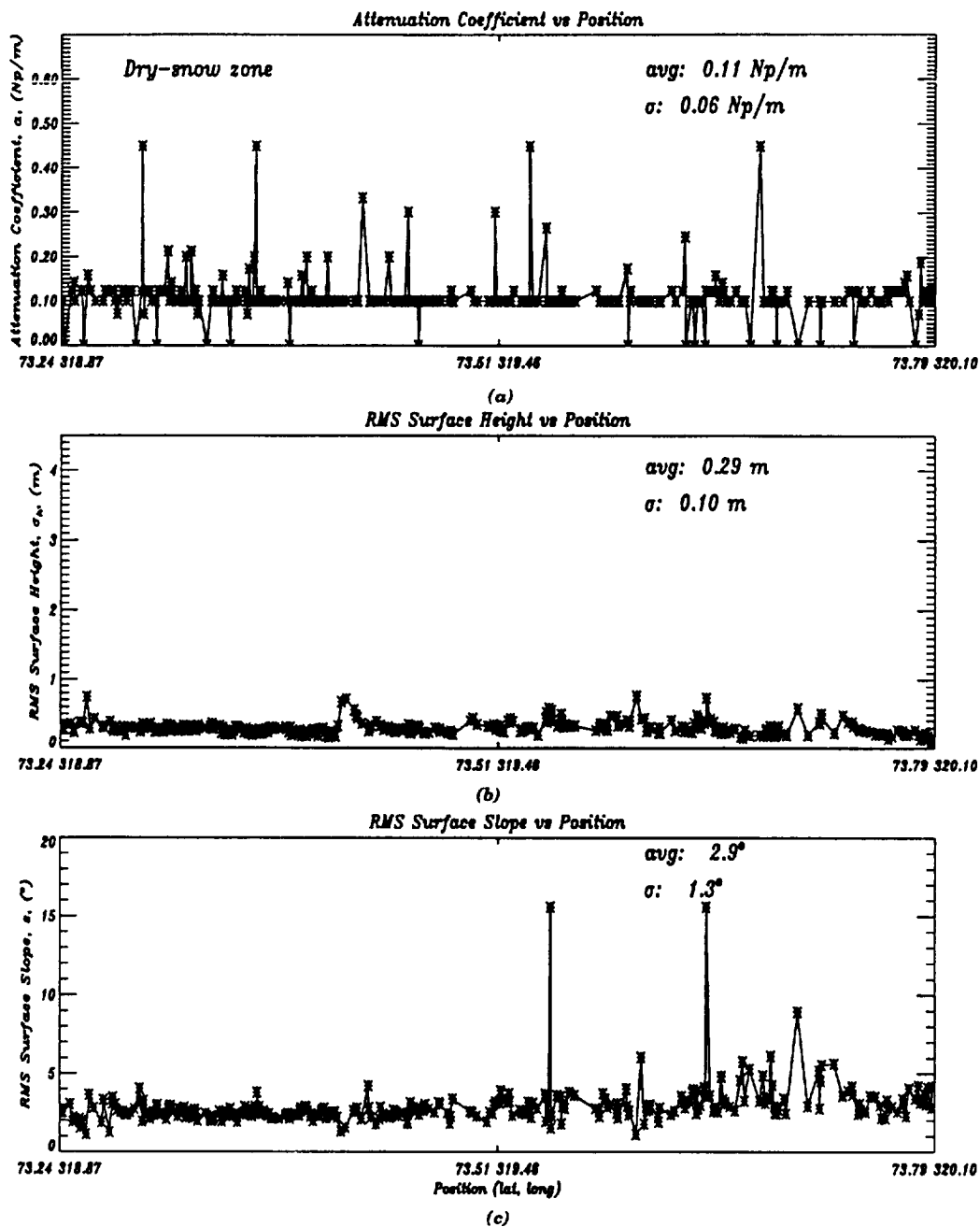


Figure 5.21. Results of the combined surface and Rayleigh volume scattering model fit to AAFE return waveforms from the dry-snow zone of the Greenland ice sheet. (a) Values of attenuation coefficient, α , (b) values of rms surface height, σ_h , and (c) values of rms surface slope, s .

5.2 Mapping Diagenetic Zones

As figure 5.5 shows, return waveforms from the percolation zone do not fit well to the surface scattering model of equation 5.15 and therefore the resulting rms error from the fit is large. Waveforms from the dry-snow zone do fit well to the surface scattering model and have a small rms error, but the resulting rms surface slope, s , is unreasonably high. Only the returns from the wet-snow zone give a small rms error and a reasonable s . These effects are apparent in figure 4.12, where the AAFE altitude results in the percolation zone differ considerably from the AOL.

Using these results, a simple algorithm has been developed that detects when ice features in the percolation zone are significant enough to affect the AAFE return waveform and give a poor fit to the surface scattering model. It also detects when s is too high to be caused by surface scattering as in the dry-snow zone. A block diagram of the diagenetic zone algorithm is shown in figure 5.22.

Since there are over one million waveforms from the 1991 experiment alone, the average result of 20 sample waveforms is taken every 20 km to reduce the amount of processing time. The AAFE altimeter not only participated in the 1991 and 1993 Greenland experiment, but also flew in 1992 in a Navy experiment over the northern part of the Greenland ice sheet from 74° N to 80° N. The altitude results were given to the Naval Research Laboratory, but the Microwave Remote Sensing Laboratory was able to keep the waveforms. Figure 5.23 shows the raw data from passing the 1991 and 1992 waveforms through the diagenetic zone algorithm. It is clear from these data that the AAFE altimeter senses the transition from the wet-snow to the percolation zone and from the percolation zone to the dry-snow zone. The data were smoothed to allow the transition to be clearly identified and then the results are compared in figure 5.24 to the transitions mapped by Benson in 1962. The two maps agree well in the north-east corner, but in the south-west the AAFE results show the transitions much further inland than the Benson map. There are insufficient

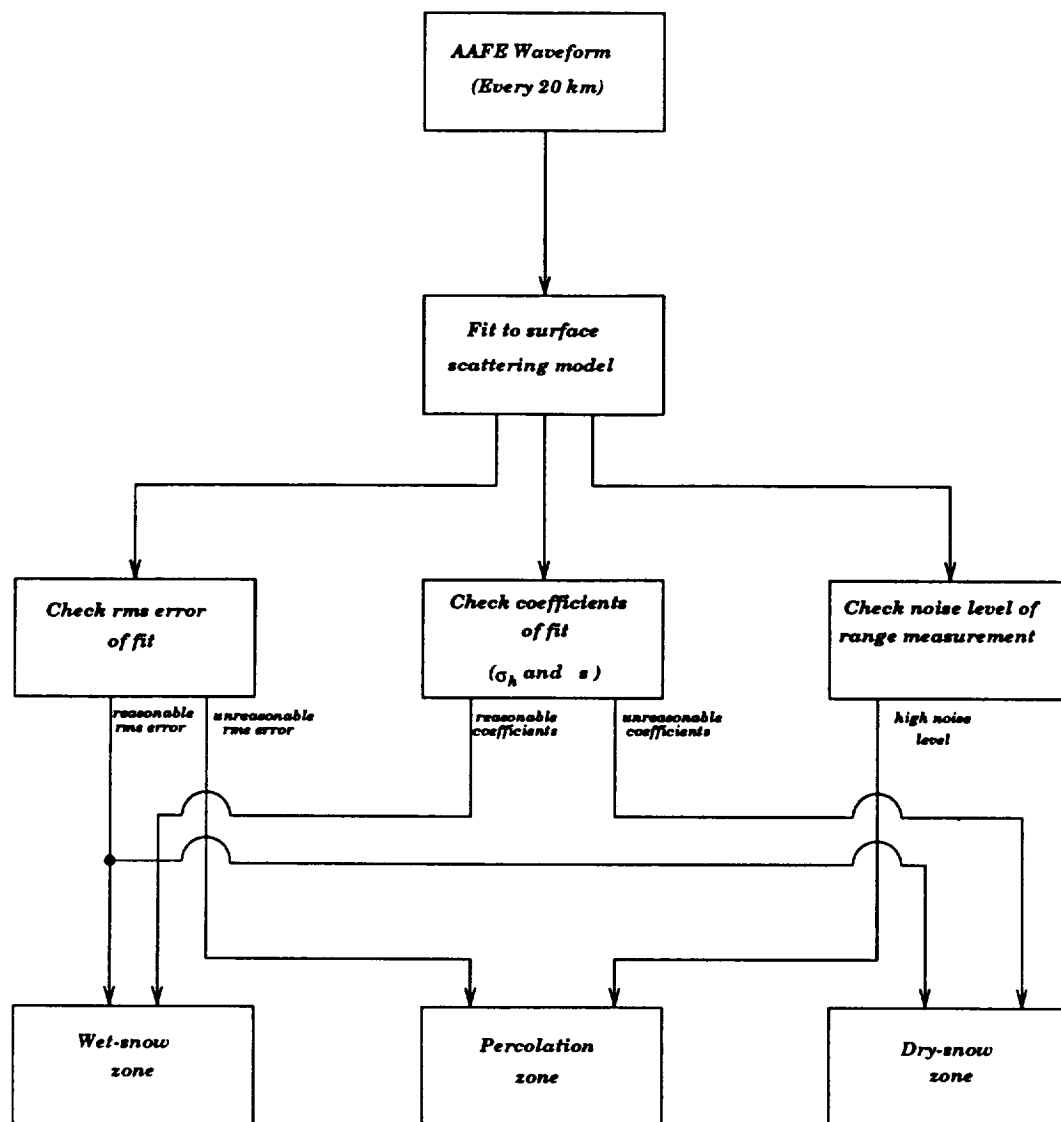


Figure 5.22. A block diagram of the algorithm used to determine the transitions between diagenetic zones of the Greenland ice sheet.

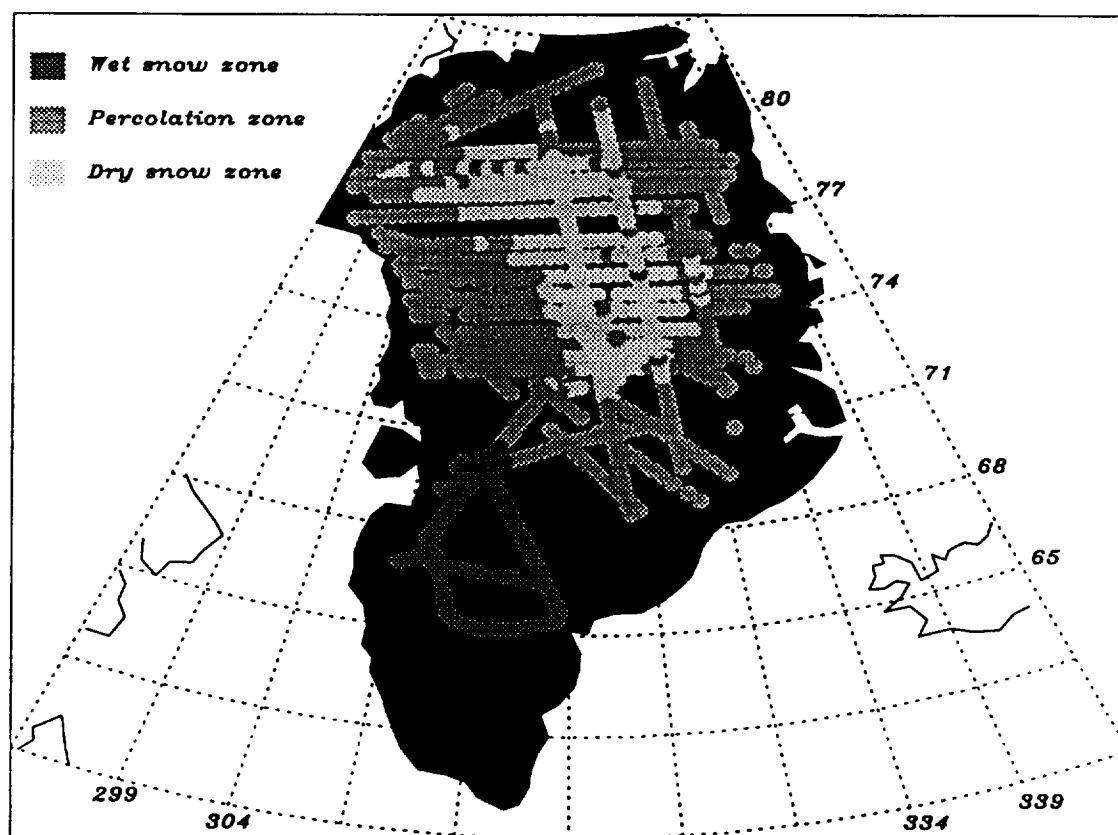


Figure 5.23. Raw data from passing the AAFE return waveforms from 1991 and 1992 through the diagenetic zone algorithm.

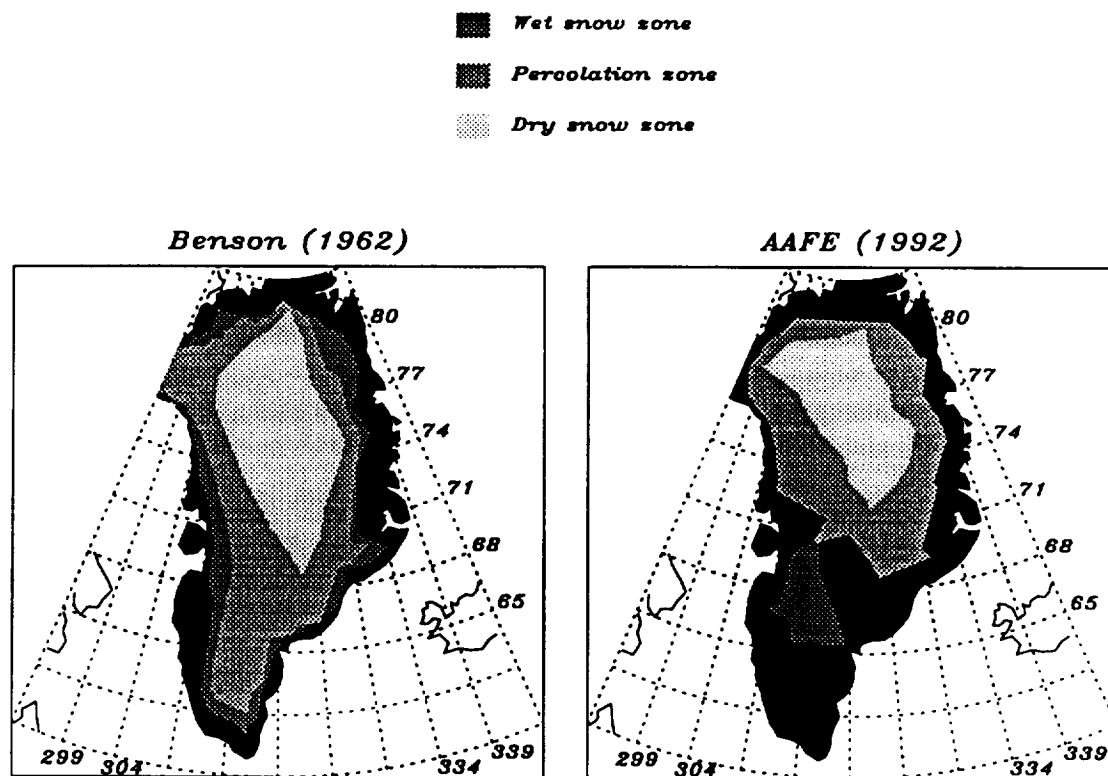


Figure 5.24. Smoothed results from the AAFE transition algorithm from 1991 and 1992 and the results from Benson in 1962.

data at this point to determine that this is the result of warming on the ice sheet. Some of the discrepancy may be due to the criteria used to map the transitions. For example, Benson was actually on the ice sheet digging pits and looking for the results of percolation, while the AAFE needs a sufficient amount of sub-surface features to affect the waveform before the algorithm determines the return is from the percolation zone. These results, however, represent the beginning of a data base to which future missions can be compared.

5.3 Comparison of Retracking Algorithms

The tracking algorithms discussed in Chapter 3 are used to keep the entire AAFE return waveform in the range window during flight so that it is completely stored for post-processing. One reason for post-processing is to retrack the stored return or find the exact point on the waveform that corresponds to the mean surface. There are several different ways to retrack a return waveform, such as fitting to a scattering model or using a mathematical analysis to find the half power point. Although retracking ocean return waveforms is well understood, returns from more complex surfaces such as ice sheets are not as predictable due to the different diagenetic zones and therefore they are much more difficult to retrack. Since the AOL laser altimeter receives a return from the ice sheet surface and has centimeter altitude precision, comparisons of AAFE altimeter retracked altitudes with the AOL altitude measurements allow different retracking methods to be analyzed.

Since there is always a surface scattering component in the AAFE returns from the Greenland ice sheet, one method of retracking the waveforms is to fit them to the surface scattering model in equation 5.15. As shown in table 5.1, one of the resulting parameters from the fit is the range to the mean surface. Figure 4.12, which is repeated here as figure 5.25, shows the resulting AAFE retracked altitudes using the surface scattering model over a south-west to north-east flight line that passed

through all of the diagenetic zones. Figure 5.25b shows the difference between the AAFE and AOL altitudes over the section and also displays the average difference and standard deviation, which are -28 cm and 30 cm respectively. The spikes on the left side of the difference plot are due to mispointing angle, but as expected from the analysis in section 5.1, the two data sets agree well in the wet-snow and dry-snow zones, but deviate significantly in the percolation zone. Therefore, this retracking method is not recommended for altimeter returns from the percolation zone.

Another method of retracking is to fit the waveforms to a five parameter continental ice sheet retracking algorithm developed by Martin et al. [Martin et al., 1983]. This model is a modification to the surface scattering model, defined in equation 5.15, that was developed by Brown [Brown, 1977]. Instead of an exponential trailing edge this model has a linear trailing edge and is defined as

$$P_r(\tau) = \beta_1 + \beta_2(1 + \beta_5 Q(x)) P\left(\frac{\tau - \beta_3}{\beta_4}\right) \quad (5.35)$$

where $Q(x)$ and $P(z)$ are defined as

$$Q(x) = \begin{cases} 0 & \tau < \beta_3 + 0.5\beta_4 \\ \tau - \beta_3 + 0.5\beta_4 & \tau \geq \beta_3 + 0.5\beta_4 \end{cases} \quad (5.36)$$

and

$$P(z) = \frac{1}{\sqrt{2\pi}} \int_{-\infty}^z e^{-q^2/2} dq = \frac{1}{2} + \frac{1}{2} \operatorname{erf}\left(\frac{z}{\sqrt{2}}\right) \quad (5.37)$$

[Zwally et al., 1990]. Table 5.3 defines the parameters used in this model and figure 5.26 shows a sample model waveform. Martin et al. [Martin et al., 1983] also defines a model for double ramped waveforms, which are often found in SEASAT altimeter returns, but this is not presented here because double ramps are not found in the AAFE airborne altimeter waveforms.

Figure 5.27a shows AAFE altitudes resulting from retracking with the Martin et al. [Martin et al., 1983] model along with the AOL altitude measurements and

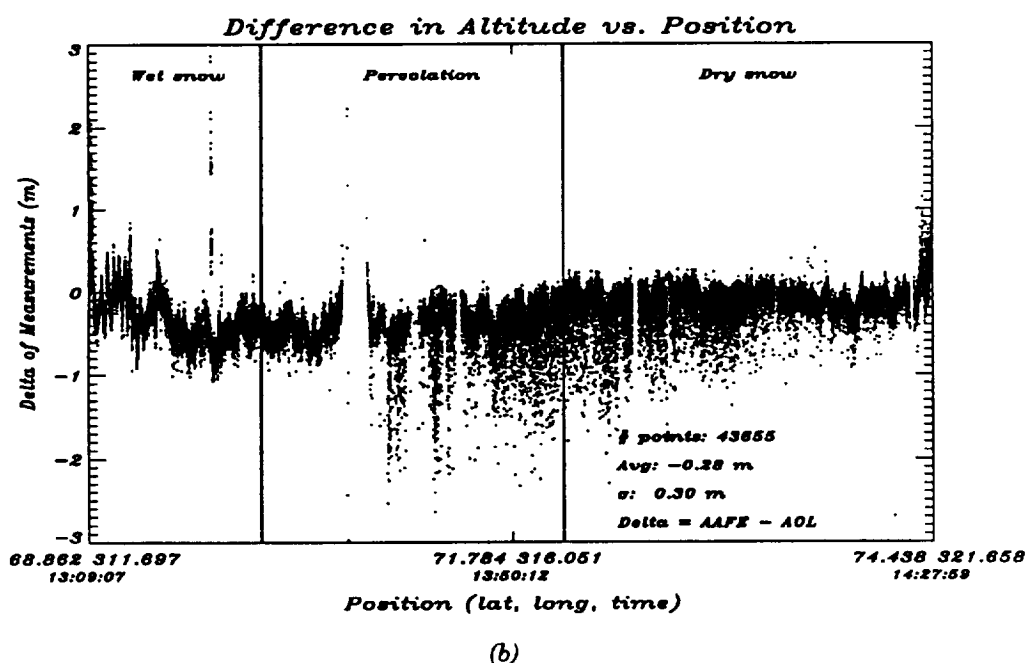
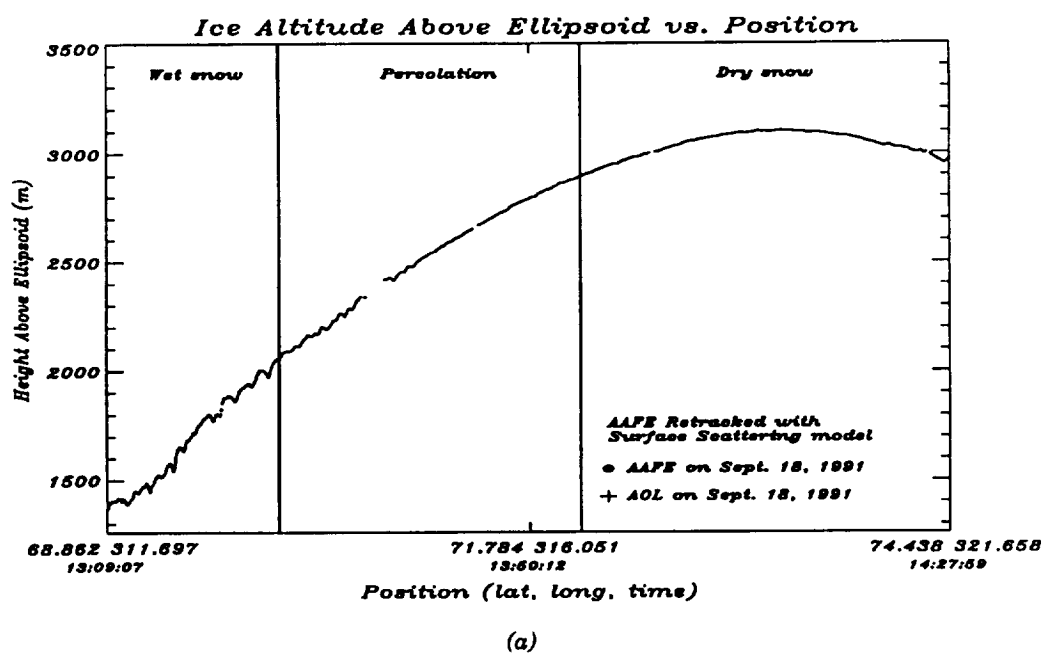


Figure 5.25. A comparison between AAFE altitudes obtained from retracking by fitting to the surface scattering model and AOL altitude measurements on September 18, 1991 over an entire south-west to north-east pass over the ice sheet. (a) The actual AAFE and AOL altitude measurements and (b) the difference between the two data sets calculated by subtracting the AOL altitude measurements from the AAFE altitude measurements.

Table 5.3. Table of the five parameters used in the least-mean-squared error fit to the Martin et al. model.

PARAMETER	VARIABLE
Noise floor	β_1
Amplitude	β_2
Range or height to mean surface	β_3
Waveform rise time	β_4
Slope of the trailing edge	β_5

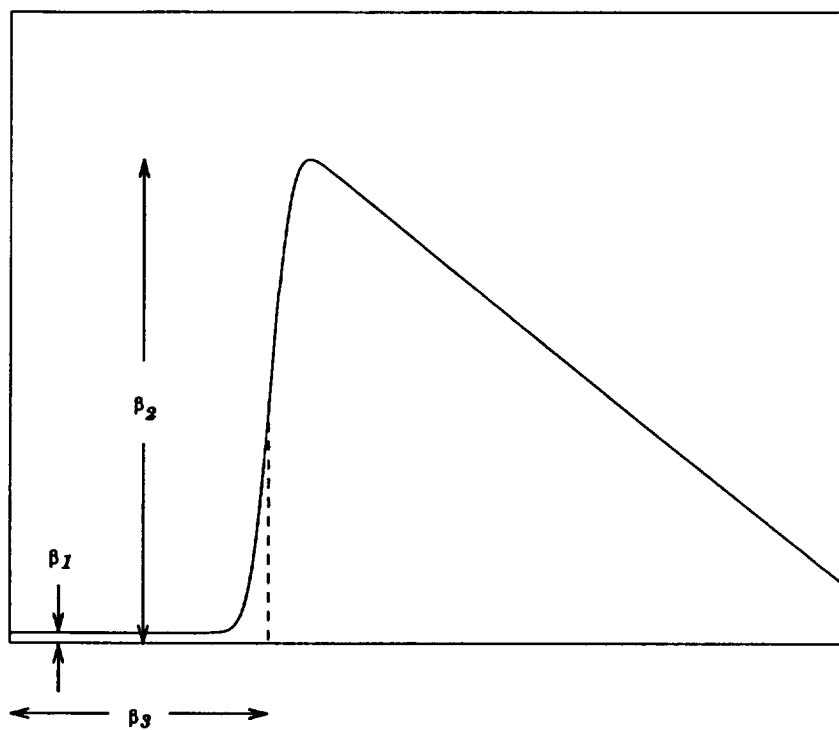
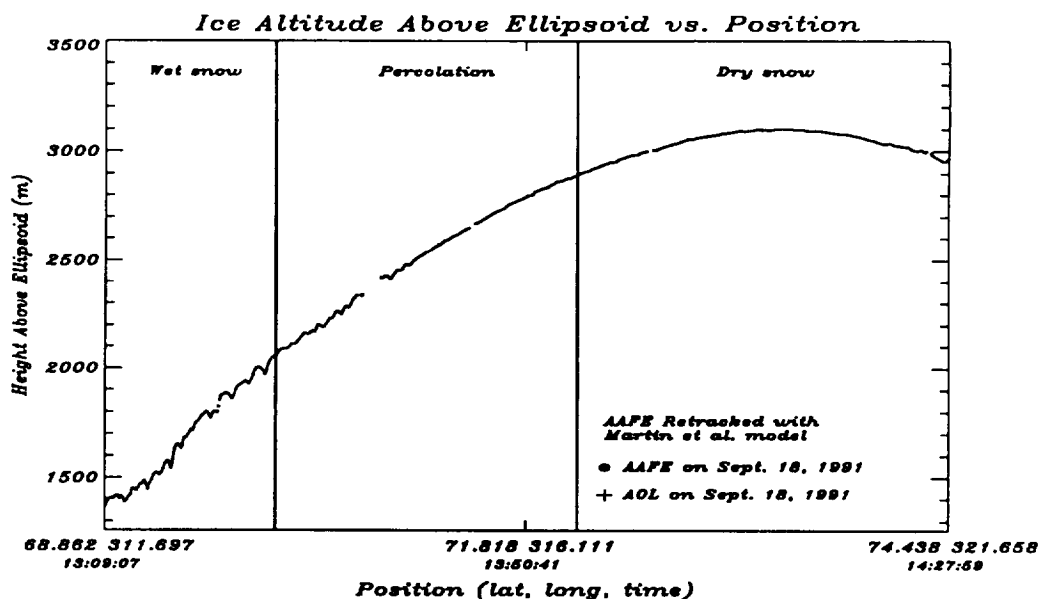
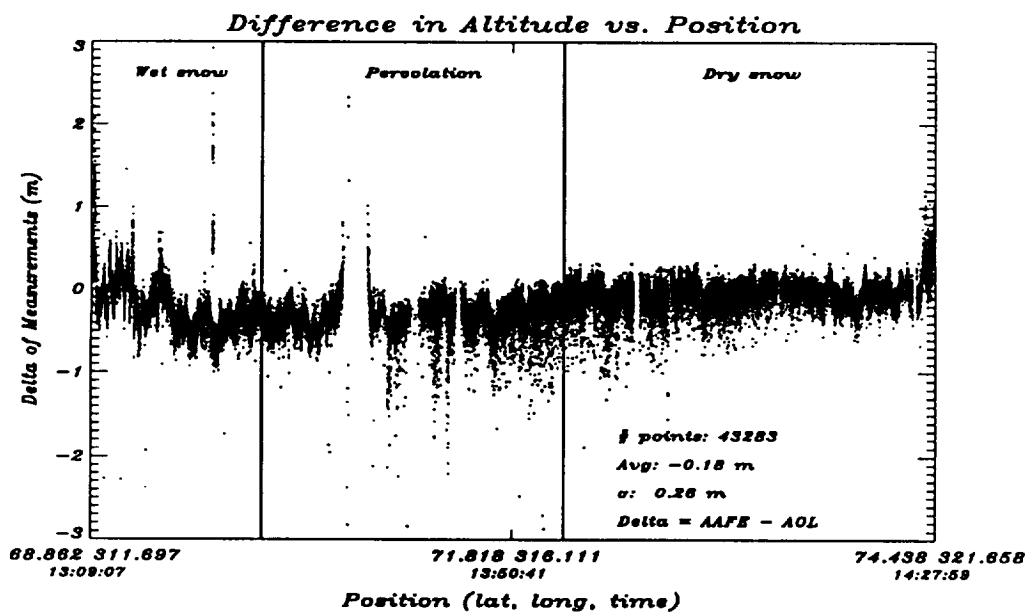


Figure 5.26. Sample radar altimeter waveform using the Martin et al [Martin et al, 1983] model.



(a)



(b)

Figure 5.27. A comparison between AAFE altitudes obtained from retracking by fitting to the Martin et al. [Martin et al., 1983] model and AOL altitude measurements on September 18, 1991 over an entire south-west to north-east pass over the ice sheet. (a) The actual AAFE and AOL altitude measurements and (b) the difference between the two data sets calculated by subtracting the AOL altitude measurements from the AAFE altitude measurements.

figure 5.27b shows the difference between the two data sets. This is the same flight line used in the comparison in figure 5.25 and it appears that the surface scattering and Martin et al. models are equivalent in the wet-snow and dry-snow regions. In the percolation zone, however, the Martin et al. model is somewhat better, but there is still an increase in the difference level showing that this retracking algorithm is sensitive to sub-surface and volume scattering.

The Offset Center of Gravity (OCOG) algorithm was discussed in detail in section 3.1.5 as a method of tracking altimeter waveforms. Since this mathematical algorithm finds the half power point on the leading edge of the altimeter return, it is also used for retracking waveforms. AAFE altitude measurements resulting from retracking with the OCOG algorithm are shown in figure 5.28a along with the AOL altitude measurements and the difference between the two data sets is shown in figure 5.28b. Although these retracked AAFE results have a -50 cm average bias, which is higher than the surface scattering or Martin et al. models, the noise level across the different diagenetic zones only increases slightly in the percolation zone. This means that the OCOG retracking algorithm is not very sensitive to the change in altimeter waveform shape due to the different zones and therefore is a good method of retracking for range measurements over all sections of the Greenland ice sheet.

Another method of retracking is to use a cubic spline [Press et al., 1988] to find the half power point on the waveform. This mathematical routine finds a smooth fit through all of the points in the return and allows the resulting function to be re-sampled at a much higher rate. For example, the asterisks in figure 5.29 represent 100 of the actual sampled points of the AAFE return and are spaced 41.67 cm apart, while the solid line is the cubic spline consisting of 5000 points spaced $41.67/50$ cm or .83 cm apart. Figure 5.30a shows the AAFE altitude measurements over the south-west to north-east flight line determined using the cubic spline and it also

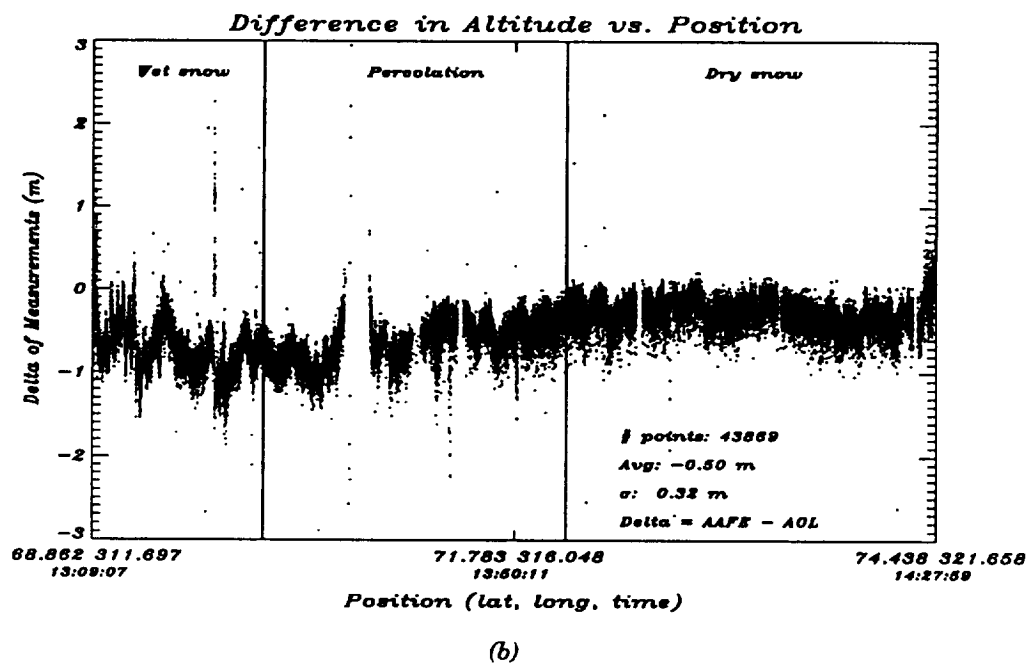
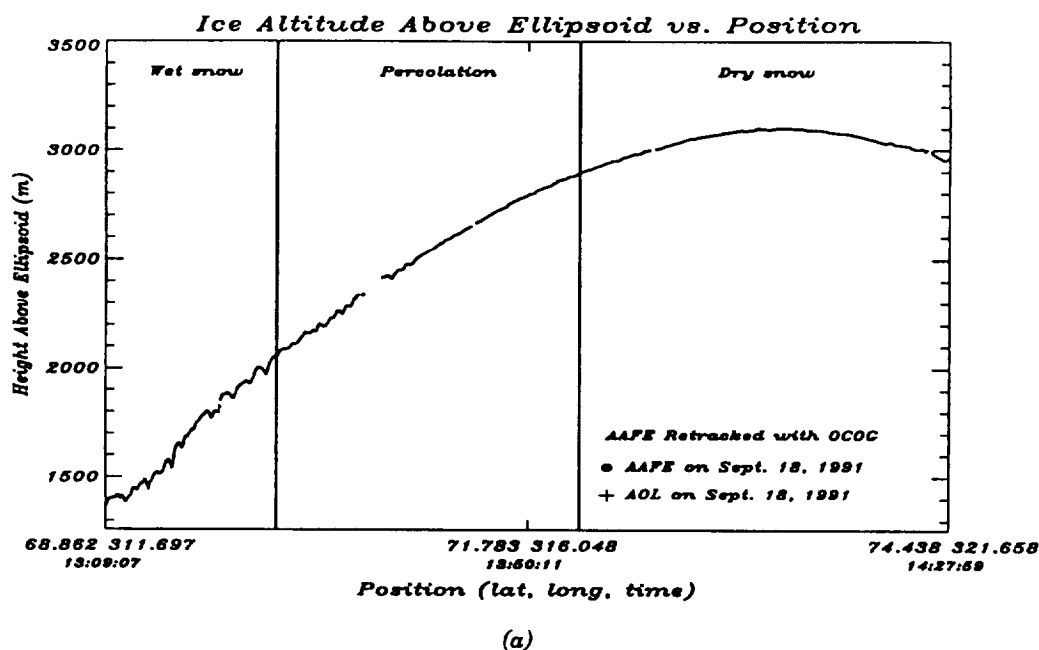


Figure 5.28. A comparison between AAFE altitudes obtained from retracking using the Offset Center of Gravity (OCOG) algorithm and AOL altitude measurements on September 18, 1991 over an entire south-west to north-east pass over the ice sheet. (a) The actual AAFE and AOL altitude measurements and (b) the difference between the two data sets calculated by subtracting the AOL altitude measurements from the AAFE altitude measurements.

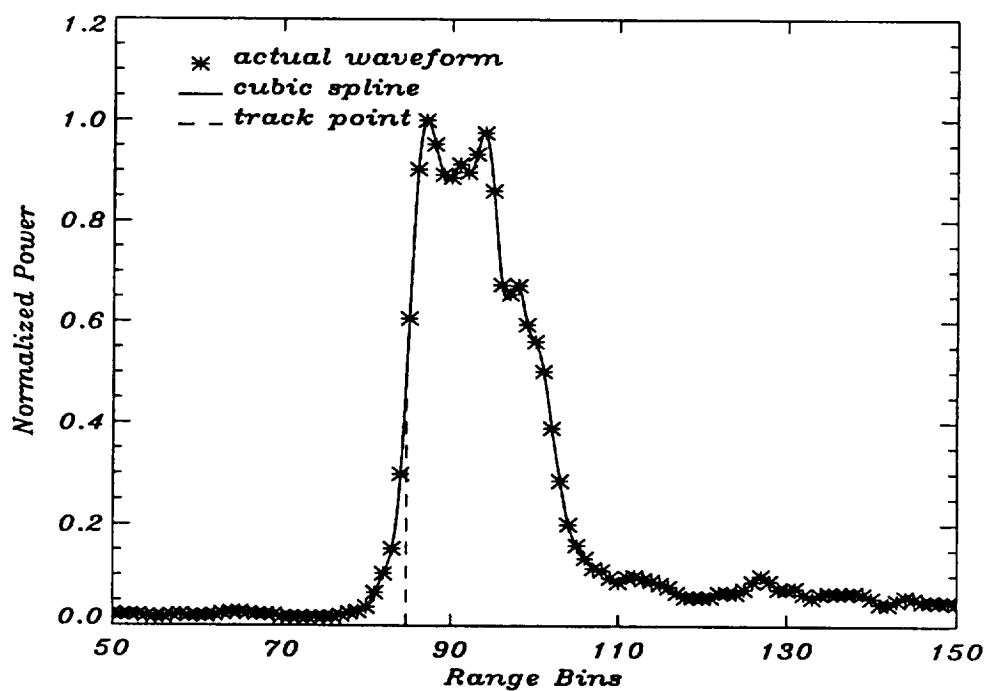
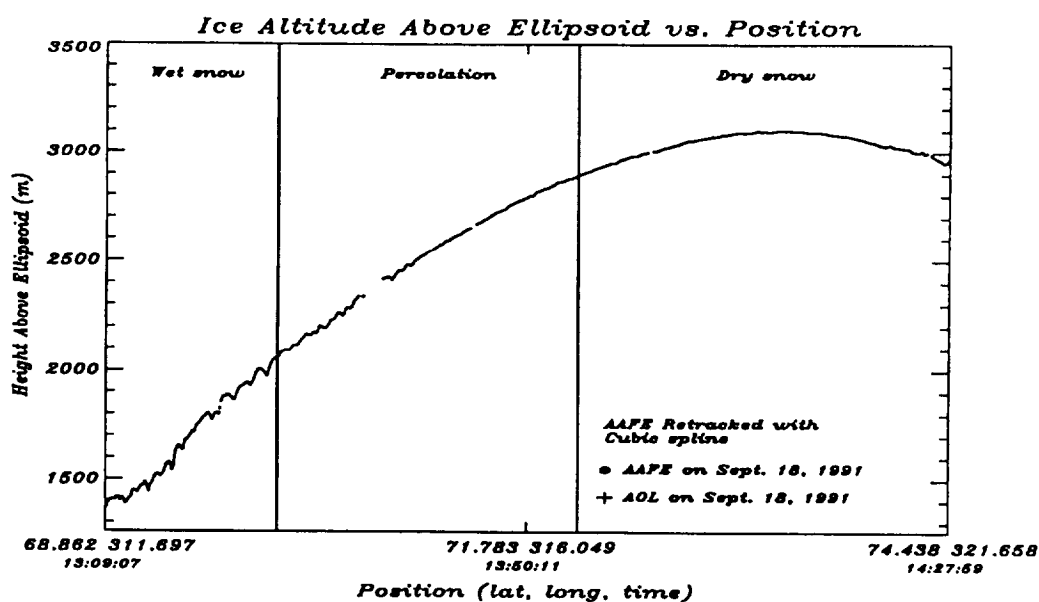


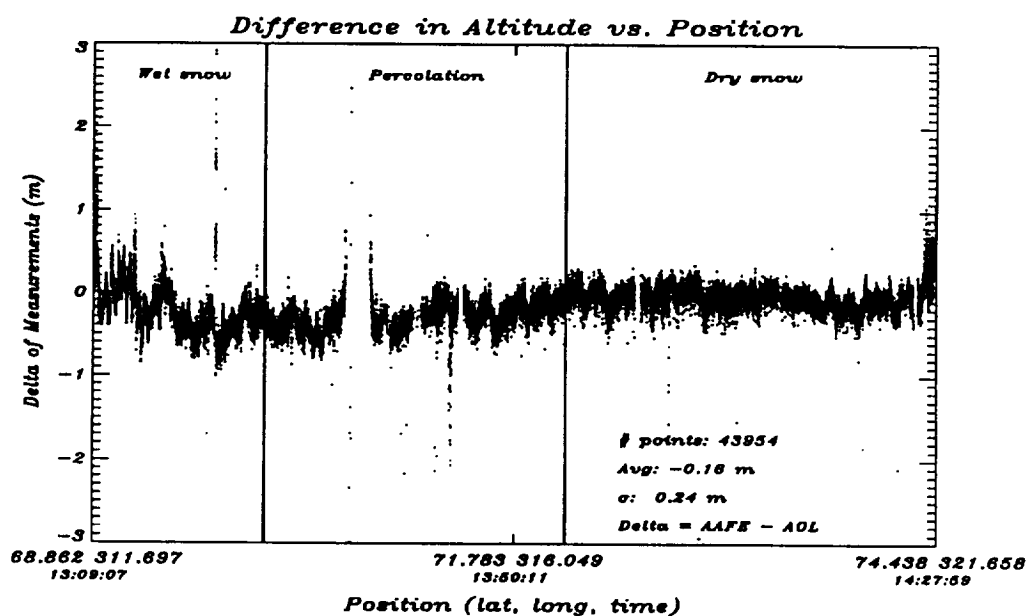
Figure 5.29. An actual AAFE return waveform (asterisks) consisting of 100 points spaced 41.67 cm apart and the cubic spline (solid line) consisting of 5000 points spaced .83 cm apart.

shows the corresponding AOL altitudes. The difference plot in figure 5.30b reveals that the cubic spline retracking method has the lowest noise level over the entire flight line and is not affected by the change in the waveform shape in the percolation zone.

Of the four retracking algorithms presented, the cubic spline is the best method for obtaining accurate range measurements over all of the diagenetic regions of the ice sheet. The OCOG retracking algorithm, however, only takes 0.5 hours to retrack one flight hour of AAFE data, while the cubic spline takes 12 hours and both the surface scattering and the Martin et al. models take approximately 40 hours. Therefore, to obtain quick first order retracked AAFE altitude measurements, the OCOG retracking algorithm is the most efficient.



(a)



(b)

Figure 5.30. A comparison between AAFE altitudes obtained from retracking using the cubic spline algorithm and AOL altitude measurements on September 18, 1991 over an entire south-west to north-east pass over the ice sheet. (a) The actual AAFE and AOL altitude measurements and (b) the difference between the two data sets calculated by subtracting the AOL altitude measurements from the AAFE altitude measurements.

CHAPTER 6

CONCLUSIONS AND RECOMMENDATIONS FOR FUTURE RESEARCH

The 1991 airborne Greenland experiment proved that the AAFE altimeter is able to track well over ice sheets and obtain accurate altitude measurements. Having both the AAFE radar and the AOL laser systems on board the aircraft made it possible to investigate issues such as penetration and sub-surface scattering in much greater detail and accuracy than can be achieved from space. Although few flight lines were repeated in the 1993 experiment, this mission covered a much larger portion of the ice sheet and allowed 1991 to 1993 comparisons to be made over the ERS-1 and EGIG lines. These comparisons revealed one of the difficulties in attempting to measure small scale surface changes, which is the ability to re-examine the same area so that actual changes in altitude are measured rather than shifts due to horizontal displacement.

The models of the diagenetic zones of Greenland provide a better understanding of how the radar altimeter Ku-band pulse interacts with the ice sheet. In addition, these models provide important information about geophysical parameters, such as rms surface roughness and slope in the wet-snow zone and attenuation and depth of penetration in the dry-snow zone. Although the percolation zone is complex and difficult to model, the ground truth data taken at Dye 2 has helped in modelling a region that has never been previously modelled.

Fitting return waveforms to these models not only allowed geophysical parameters of the ice sheet to be measured, but also provided an estimate of the range to the mean surface below the instrument. Comparisons of these range measurements

with the AOL laser altimeter altitude measurements enabled the assessment of these models along with several other retracking algorithms over the different diagenetic regions of Greenland.

As the interest in studying the earth and its geophysical properties increases, it is important to increase the system performance and versatility of the AAFE radar altimeter. By putting a low noise amplifier in the receiver front end and replacing all the remaining original active components, the dynamic range of the instrument can be increased significantly, resulting in higher range resolution and improved tracking abilities. If an advanced terrain tracker is implemented in the system, it could be used for terrain mapping of forests, remote lakes, rivers and desserts. In addition, the efficiency of the AAFE data acquisition and tracking subsystem could be improved by installing the tracking software on the VSP board.

Since the AAFE radar altimeter uses the same frequency and principle of operation as the ERS-1 satellite radar altimeter, comparisons of AAFE return waveforms to ice sheet satellite return waveforms will provide a better understanding of the information obtained by the satellite and help in investigating issues such as slope-induced error [Brenner et al., 1983]. Also, future ERS-1 underflights will aid in understanding satellite returns from other complex surfaces.

Currently, the future experiments planned for the AAFE radar altimeter include the 1994 NASA Greenland Airborne Experiment, which will map the northern half of the ice sheet. This experiment will be based out of Thule and will cover many of the same areas that were measured by the Navy in 1992. Using the diagenetic zone algorithm, the position of zone transitions in 1992 and 1994 can be compared. During the following few years (1995 - 1997) the NASA airborne group will concentrate on measuring the glaciers in northern Canada and then return to Greenland in 1998 or 1999 to repeat many of the original flight lines.

REFERENCES

- [Analytek, 1991] Analytek (1991). *Analytek Limited Series 2000 Waveform Sampler Systems Operations Manual*. Analytek Ltd. Marketing Department, Sunnyvale, CA.
- [Barrick, 1972] Barrick, D. E. (1972). *Remote Sensing of the Troposphere*, chapter 12. U.S. Government Printing Office, Washington, DC.
- [Benson, 1962] Benson, C. S. (1962). Stratigraphic studies in the snow and firn of the greenland ice sheet. Research Report 70, U.S. Army Snow Ice and Permafrost Research Establishment.
- [Bindshadler et al., 1989] Bindshadler, R. A., Zwally, H. J., Major, J. A., and Brenner, A. C. (1989). Surface topography of the greenland ice sheet from satellite radar altimetry. Technical Report SP-503, NASA.
- [Brenner et al., 1983] Brenner, A. C., Bindshadler, R. A., Thomas, R. H., and Zwally, H. J. (1983). Slope-induced errors in radar altimetry over continental ice sheets. *Journal of Geophysical Research*, 88(C3):1617-1623.
- [Brown, 1977] Brown, G. S. (1977). The average impulse response of a rough surface and its applications. *IEEE Journal of Oceanic Engineering*, OE-2(1):67-74.
- [Carnahan et al., 1969] Carnahan, B., Luther, H. A., and Wilkes, J. O. (1969). *Applied Numerical Methods*. John Wiley and Sons, Inc.
- [Davis, 1992] Davis, C. H. (1992). Satellite radar altimetry. *IEEE Transactions on Microwave Theory and Techniques*, 40(6):1070-1076.
- [Davis, 1993] Davis, C. H. (1993). A combined surface and volume scattering model for ice sheet radar altimetry. To be published.
- [Davis and Zwally, 1993] Davis, C. H. and Zwally, H. J. (1993). Geographic and seasonal variations in the surface properties of the ice sheets by satellite radar altimetry. To be published.
- [Gundestrup et al., 1986] Gundestrup, N. S., Bindshadler, R. A., and Zwally, H. J. (1986). SEASAT range measurements verified on a 3-d ice sheet. *Annals of Glaciology*, 8:69-72.
- [Hallikainen et al., 1986] Hallikainen, M. T., Ulaby, F. T., and Abdelrazik, M. (1986). Dielectric properties of snow in the 3 to 37 ghz range. *IEEE Transactions on Antennas and Propagation*, AP-34(11):1329-1340.

- [Harris, 1978] Harris, F. J. (1978). On the use of windows for harmonic analysis with the discrete fourier transform. *Proceedings of the IEEE*, 66(1):51-83.
- [Haykin, 1983] Haykin, S. (1983). *Communication Systems*. John Wiley and Sons.
- [Haykin, 1989] Haykin, S. (1989). *An Introduction to Analog and Digital Communications*. John Wiley and Sons.
- [Impact, 1987] Impact (1987). *Viper 8704/30 User's Manual*. Impact Technologies, Inc., Santa Clara, CA.
- [Impact, 1988] Impact (1988). *161ASM User's Manual*. Impact Technologies, Inc., Santa Clara, CA.
- [Jackson et al., 1992] Jackson, F. C., Walton, W. T., Hines, D. E., Walter, B. A., and Peng, C. Y. (1992). Sea surface mean surface slope from ku-band backscatter data. *Journal of Glaciology*, 97(C7):11411-11427.
- [Krabill, 1994] Krabill, W. (1994). NASA Wallops Flight Facility. Personal Communication.
- [Ling, 1985] Ling, C. H. (1985). A note on the density distribution of dry snow. *Journal of Glaciology*, 31(108):194-195.
- [Martin et al., 1983] Martin, T. V., Zwally, H. J., Brenner, A. C., and Bindshadler, R. A. (1983). Analysis and retracking of continental ice sheet radar altimeter waveforms. *Journal of Geophysical Research*, 88(C3):1608-1616.
- [McGoogan et al., 1974] McGoogan, J. T., Miller, L. S., and Brown, G. S. (1974). The S-193 radar altimeter experiment. *Proceedings of the IEEE*, 62(6):793-803.
- [Meier, 1990] Meier, M. F. (1990). Reduced rise in sea level. *Nature*, 343:115-116.
- [NASA, 1976] NASA (1976). *Final Report of the Advanced Application Flight Experiment Breadboard Pulse Compression Radar Altimeter Program*. NASA Contractor Report CR-141411.
- [Oppenheim and Schafer, 1989] Oppenheim, A. V. and Schafer, R. W. (1989). *Discrete-Time Signal Processing*. Prentice Hall.
- [Papoulis, 1973] Papoulis, A. (1973). Minimum-bias windows for high-resolution spectral estimates. *IEEE Transactions on Information Theory*, 19(1):9-12.
- [Partington et al., 1989] Partington, K. C., Ridley, J. K., Rapley, C. G., and Zwally, H. J. (1989). Observations of the surface properties of the ice sheets by satellite radar altimetry. *Journal of Glaciology*, 35(120):267-275.
- [Press et al., 1988] Press, W. H., Flannery, B. P., Teukolsky, S. A., and Vetterling, W. T. (1988). *Numerical Recipes in C*. Cambridge University Press.

- [Rapley et al., 1983] Rapley, Friffiths, Squire, Lefebvre, Birks, Brenner, Brossier, Clifford, Cooper, Cowan, Drewry, Gorman, Huckle, Lamb, Martin, McIntyre, Milne, Novotny, Peckham, Schgounn, Scott, Thomas, and Vesecky (1983). A study of satellite radar altimeter operation over ice-covered surfaces. European Space Agency Contract Report 5182/8/F/CG(SC), European Space Agency.
- [Rapley, 1990] Rapley, C. G. (1990). Satellite radar altimeters. *Microwave Remote Sensing for Oceanographic and Marine Weather Forecast Models*, pages 45–63.
- [Ridley and Partington, 1988] Ridley, J. K. and Partington, K. C. (1988). A model of satellite radar altimeter returns from ice sheets. *International Journal of Remote Sensing*, 9(4):601–624.
- [Robin, 1966] Robin, G. Q. (1966). Mapping the antarctic ice sheet by satellite altimetry. *Canadian Journal of Earth Sciences*, 3(6):893–901.
- [Schneider, 1992] Schneider, S. H. (1992). Will sea levels rise or fall. *Nature*, 356:11–12.
- [Skolnik, 1980] Skolnik, M. I. (1980). *Introduction to Radar Systems*. McGraw Hill Inc.
- [Stanford, 1987] Stanford (1987). *Model DG535 Digital Dealy/Pulse Generator*. Stanford Research Systems, Inc., Sunnyvale, CA.
- [Stiles and Ulaby, 1980] Stiles, W. H. and Ulaby, F. T. (1980). The active and passive microwave response to snow parameters 1. wetness. *Journal of Geophysical Research*, 85(C2):1037–1044.
- [Stiles and Ulaby, 1981] Stiles, W. H. and Ulaby, F. T. (1981). Dielectric properties of snow. NASA Contractor Report NASA CR-166764, NASA.
- [Swift et al., 1985] Swift, C. T., Hayes, P. S., Herd, J. S., Jones, W. L., and Delnore, V. E. (1985). Airborne microwave measurements of the southern greenland ice sheet. *Journal of Geophysical Research*, 90(B2):1983–1994.
- [Ulaby et al., 1981] Ulaby, F., Moore, R., and Fung, A. (1981). *Microwave Remote Sensing; Active and Passive Vol 1*. Artech House.
- [Ulaby et al., 1982] Ulaby, F., Moore, R., and Fung, A. (1982). *Microwave Remote Sensing; Active and Passive Vol 2*. Addison-Wesley.
- [Ulaby et al., 1986] Ulaby, F., Moore, R., and Fung, A. (1986). *Microwave Remote Sensing; Active and Passive Vol 3*. Artech House.
- [Ulaby and Stiles, 1980] Ulaby, F. T. and Stiles, W. H. (1980). The active and passive microwave response to snow parameters 2. water equivalent of dry snow. *Journal of Geophysical Research*, 85(C2):1045–1049.

- [Wingham et al., 1986] Wingham, D. J., Rapley, C. G., and Griffiths, H. (1986). New techniques in satellite altimeter tracking systems. *Proceedings of IGARSS 1986 Symposium*, pages 1139-1344.
- [Zabel, 1993] Zabel, I. (1993). Byrd Polar Research Center. Personal Communication.
- [Zabel et al., 1994] Zabel, I. H., Baggeroer, P. A., and Jezek, K. C. (1994). Radar and snow studies in the percolation zone of the greenland ice sheet: A data report on the 1993 field season at dye 2. Technical note 94-01, Byrd Polar Research Center.
- [Zwally, 1989] Zwally, H. J. (1989). Growth of greenland ice sheet: Interpretation. *Science*, 246:1589-1591.
- [Zwally et al., 1983] Zwally, H. J., Bindshadler, R. A., Brenner, A. C., Martin, T. V., and Thomas, R. H. (1983). Surface elevation contours of greenland and antarctic ice sheets. *Journal of Geophysical Research*, 88(C3):1589-1596.
- [Zwally et al., 1989] Zwally, H. J., Brenner, A. C., Major, J. A., Bindshadler, R. A., and Marsh, J. G. (1989). Growth of greenland ice sheet: Measurement. *Science*, 246:1587-1589.
- [Zwally et al., 1990] Zwally, H. J., Brenner, A. C., Major, J. A., Martin, T. V., and Bindshadler, R. A. (1990). Satellite radar altimetry over ice, volume 1 - processing and corrections of seasat data over greenland. Reference Publication 1233, NASA.
- [Zwally et al., 1987] Zwally, H. J., Major, J. A., Brenner, A. C., and Bindshadler, R. A. (1987). Ice measurements by GEOSAT radar altimeter. *Johns Hopkins APL Technical Digest*, 8(2):251-254.